

# **Rolling Contact Fatigue of Silicon Nitride**

Wei Wang

A thesis submitted in partial fulfilment of the  
requirement of Bournemouth University for the  
degree of Doctor of Philosophy

December 2010

Bournemouth University

This copy of the thesis has been supplied on condition that anyone who consults it is understood to recognise that its copyright rests with its author and due acknowledgement must always be made of any material contained in, or derived from, this thesis.

## Abstract

Silicon Nitride has traditionally been used as rolling contact bearing material owing to its superior performance compared to bearing steels. Its successful application as a bearing element has led to the development of Silicon Nitride in other rolling contact applications in the automotive industry and the power industry. However, a major limitation of its wider application is its high material and machining cost, especially the cost associated with the finishing process. In the present study, a low cost sintered and reaction-bonded Silicon Nitride is used to study the surface machining effects on its rolling contact fatigue performance. Studies have been carried out to link the surface strengths of Silicon Nitride derived from half-rod and C-Sphere flexure strength specimens to the rolling contact lives of Silicon Nitride rod and ball specimens. The rolling contact fatigue tests were carried out on ball-on-rod and modified four-ball machines. Three types of surface with coarse, fine and RCF-conventional finishing conditions were examined. Flexure strength tests on half-rod and C-Sphere showed an increasing surface strength from specimens with coarse, fine to RCF-conventionally machined conditions. During rolling contact fatigue tests of as-machined specimens, no failures were observed on either ball-on-rod or four-ball tests after 100 million stress cycles. However, a trend of decreasing wear volumes was measured on the contact path of rods and balls with coarse, fine and RCF-conventional conditions. In four-ball tests, spall failures were observed on pre-cracked specimens. There was a trend of increasing rolling contact fatigue lifetime from pre-cracked specimens with coarse, fine to RCF-conventional machining conditions. The study of Silicon Nitride machining was also carried out using an eccentric lapping machine to investigate the effect of eccentricity on the finishing rate of hot isostatically-pressed and sintered and reaction-bonded Silicon Nitride. The eccentricity had no significant impact on finishing rate as concluded in this study. The effect of lubricant viscosity and chemistry on the rolling contact fatigue performance of Silicon Nitride was also studied. The result is inconclusive.

## Publications

1. **Wang, W.**, Wereszczak, A. and Hadfield, M., Flexure Strength of Silicon Nitride as Indication of Rolling Contact Performance Measured on Ball-on-Rod and Modified Four-Ball Testers, Tribology International Journal. Vol. 43, pp. 423-432 (2010).
2. **Wang, W.**, Wereszczak, A., Hadfield, M., Surface Strength of Silicon Nitride in Relation to Rolling Contact Performance. Ceramics International Journal. Vol. 35, pp. 3339-3346 (2009).
3. **W. Wang**, A. A. Wereszczak and M. Hadfield, WIT Transactions of Engineering Sciences, Vol. 55 111-122 (2007)
4. A. Wereszczak, **W. Wang**, O. M. Jadaan, and M. J. Lance, Ceramic Engineering and Science Proceedings, Vol. 27(2), 281-293 (2006)
5. **W. Wang**, M. Hadfield, Y. Wang and A. A. Wereszczak, Tribology 2006: IMechE Tribology Group 50<sup>th</sup> Anniversary Conference Proceedings, No. C645-034 (2006)

# Abbreviations

ORNL- Oak Ridge National Laboratory  
SRBSN – Sintered and Reaction Bonded Silicon Nitride  
RBSN – Reaction Bonded Silicon Nitride  
HIP – Hot Isostatically Pressed  
SEM – Scanning Electron Microscope  
XRD – X-ray Diffraction  
HP – Hot Press  
GPS – Gas Pressure Sinter  
RCF – Rolling Contact Fatigue  
RUS – Resonance Ultrasound Spectroscopy  
NIST – National Institute of Standards and Technology  
UV – Ultra-violet  
EDX – Energy Dispersive X-ray Spectroscopy  
ASTM – American Society for Testing and Materials  
JIS – Japanese Industrial Standards  
CARES – Ceramics Analysis and Reliability Evaluation of Structures  
FEA – Finite Element Analysis  
PAO - Poly-alpha-olefin

# Contents

<b>ABSTRACT</b> .....	<b>III</b>
<b>PUBLICATIONS</b> .....	<b>IV</b>
<b>ABBREVIATIONS</b> .....	<b>V</b>
<b>CONTENTS</b> .....	<b>VI</b>
<b>LIST OF FIGURES</b> .....	<b>VIII</b>
<b>LIST OF TABLES</b> .....	<b>XIII</b>
<b>ACKNOWLEDGEMENT</b> .....	<b>XIV</b>
<b>1. CHAPTER 1: INTRODUCTION</b> .....	<b>1</b>
1.1 BACKGROUND .....	1
1.2 LITERATURE REVIEW .....	6
1.2.1 Silicon Nitride Material.....	6
1.2.2 Rolling Contact Fatigue Test.....	8
1.2.3 Residual Stress in Silicon Nitride .....	12
1.2.4 Materials Characterisation.....	13
1.2.5 Machining Damage and Strength of Silicon Nitride.....	14
1.3 STATE-OF-THE-ART FROM LITERATURE REVIEW .....	15
1.4 SCOPE OF RESEARCH .....	16
1.5 STRUCTURE OF THESIS .....	16
<b>2. CHAPTER 2: SILICON NITRIDE MICROSTRUCTURE AND MACHINING</b> .....	<b>18</b>
2.1 SILICON NITRIDE MATERIAL .....	18
2.2 SILICON NITRIDE MACHINING .....	23
2.2.1. Grinding of Silicon Nitride ball.....	23
2.2.2. Lapping of Silicon Nitride ball.....	26
2.2.3. Machining of RCF Rod Specimens .....	36
2.2.4. Machining of C-Sphere Specimens .....	37
<b>3. CHAPTER 3: SURFACE STRENGTH OF SILICON NITRIDE</b> .....	<b>39</b>
3.1 RCF HALF CYLINDER FLEXURE STRENGTH .....	39
3.2 C-SPHERE TEST .....	42
3.2.1. C-Sphere Geometry .....	42
3.2.2. C-Sphere FEA Characteristics .....	44
3.2.3. C-Sphere Flexure Test .....	48
3.2.4. C-Sphere Test Results and Discussion .....	49
<b>4. CHAPTER 4: ELASTIC PROPERTY AND RESIDUAL STRESS OF SILICON NITRIDE</b> ...	<b>55</b>
4.1 RUS MEASUREMENT OF ELASTIC PROPERTIES OF SILICON NITRIDE.....	55
4.1.1 Mechanical Measurement of Elastic Properties of Materials .....	55
4.1.2 RUS Measurement Equipment .....	56
4.1.3 RUS Measurement Methodology .....	57
4.1.4 RUS Measurement Results.....	59
4.2 RESIDUAL STRESS MEASUREMENT.....	63
4.2.1 Type and Measurement of Residual Stress .....	63
4.2.2 Residual Stress Result and Discussion .....	65
<b>5. CHAPTER 5: ROLLING CONTACT FATIGUE</b> .....	<b>69</b>

5.1 ROLLING CONTACT FATIGUE METHODOLOGY .....	69
5.1.1 <i>Modified Four Ball Test</i> .....	69
5.1.2 <i>Ball-on-Rod Test</i> .....	71
5.1.3 <i>Four-Ball and Ball-on-Rod Tribometers: Comparison</i> .....	72
5.1.4 <i>Surface Defects and Artificial Defects Introduction</i> .....	75
5.2 ROLLING CONTACT WEAR .....	78
5.3 ROLLING CONTACT FATIGUE .....	83
5.3.1 <i>RCF Life of Lapped SRBSN Silicon Nitride</i> .....	83
5.3.2 <i>RCF Life of Core Drilled SBRSN Silicon Nitride</i> .....	86
5.4 EFFECT OF LUBRICANT VISCOSITY .....	90
<b>6. CHAPTER 6: DISCUSSION AND CONCLUSIONS .....</b>	<b>95</b>
6.1 SURFACE STRENGTH, RESIDUAL STRESS AND MACHINING PROCESS OF SILICON NITRIDE.....	95
6.2 SURFACE STRENGTH AND ROLLING CONTACT FATIGUE .....	96
6.3 CONCLUSIONS .....	98
6.4 FUTURE WORKS .....	99
<b>7. APPENDIX.....</b>	<b>101</b>
7.1 PLASMA ETCHING .....	101
7.2 HALF ROD OPTICAL FRACTOGRAPHY.....	103
7.3 C-SPHERE SEM FRACTOGRAPHY .....	112
7.4 MODIFIED FOUR-BALL MACHINE – HERTZIAN STRESS .....	116
7.5 BALL-ON-ROD TESTER CONFIGURATION .....	117
7.6 BALL ON ROD – CONTACT ANALYSIS.....	120
7.7 ABSOLUTE VISCOSITY .....	123
<b>8. REFERENCES.....</b>	<b>125</b>

# List of Figures

Figure 1-1: Silicon Nitride ball bearing element. (SKF).....	4
Figure 1-2: Hybrid ceramic bearing with Silicon Nitride rolling element and steel race. (SKF).....	4
Figure 1-3: Silicon Nitride diesel engine component. (Ceradyne Co.).....	5
Figure 1-4: Ceramic components made from SRBSN material. (Ceradyne Co.).....	5
Figure 1-5: SEM image of SRBSN fracture surface showing porosity (Tuyen, Park et al. 2009) .....	8
Figure 1-6: Scope of research .....	16
Figure 2-1: Plasma etched microstructure of Ceralloy 147-31N Silicon Nitride. a. 5000x; b. 10000x;.....	19
Figure 2-3: Thermal-chemical etched microstructure of Toshiba TSN03NH Silicon Nitride at different magnification.....	20
Figure 2-4: Thermal-chemical etched microstructure of NBD200 Silicon Nitride at different magnification.....	21
Figure 2-5: Thermal-chemical etched microstructure of SN101C Silicon Nitride at different magnification.....	21
Figure 2-6: Schematic of core drill machining of Silicon Nitride. ....	23
Figure 2-7: Surface profile of coarse finished Si <sub>3</sub> N <sub>4</sub> ball using core drills. ....	24
Figure 2-8: Surface profile of fine finished Silicon Nitride ball using core drills. ....	24
Figure 2-9: Surface profile of RCF-conventional finished Silicon Nitride ball using core drills. ....	25
Figure 2-10: Zygo Newview optical interferometer.....	25
Figure 2-11: Schematic of the lapping machine (Kang and Hadfield 2001) .....	27
Figure 2-12: The lapping machine setup.....	27
Figure 2-13: Three units of lapping machine.....	28
Figure 2-14: Lower plate.....	28
Figure 2-15: Upper plate .....	28
Figure 2-16: Variation of $\omega_b$ , $\beta$ , $\omega_c$ during a 360° of the lower plate under a typical lapping condition with the V-groove having 8mm eccentricity (Kang and Hadfield 2001). .....	29
Figure 2-17: Influence of eccentricity on ball kinematics under the same lapping condition(Kang and Hadfield 2001).....	30
Figure 2-18: Typical surface profile of Spheric-Toshiba after 45 micron diamond paste lapping.....	31
Figure 2-19: Finishing rates of Spheric-Toshiba ball blanks.....	32
Figure 2-20: 45 micron diamond paste finished SRBSN ball blank surface profile.....	33
Figure 2-21: SRBSN ball blank finishing rate .....	34
Figure 2-22: Spheric-Toshiba ball blanks after 1/4 micron diamond paste lapping at 12.70 mm diameter .....	35
Figure 2-23: SRBSN ball blanks after 1/4 micron diamond paste lapping at 12.70 mm diameter.....	35
Figure 2-24: Material removal rate comparison.....	35
Figure 2-25: Longitudinally-ground surface.....	36

Figure 2-26: Transversely-ground surface .....	36
Figure 2-27: C-Sphere specimen geometry .....	37
Figure 2-28: C-Sphere specimens .....	38
Figure 2-29: C-Sphere specimens .....	38
Figure 3-1: RCF half cylinder flexural strength specimen dimensions and tolerances ....	39
Figure 3-2: Half RCF cylinder flexure strength of coarse, fine and RCF-Conventionally machined SRBSN specimens .....	40
Figure 3-3: Optical fractography of the weakest coarse, fine and RCF-Conventionally finished specimens, from top to bottom respectively .....	41
Figure 3-4: C-Sphere geometry .....	43
Figure 3-5: C-Sphere flexure strength loading schematic .....	43
Figure 3-6: Mesh distribution for ¼ symmetry model of the C-Sphere specimen. ....	44
Figure 3-7: Intermediate mesh .....	45
Figure 3-8: Fine mesh .....	45
Figure 3-9: a) nodal first principal stress distribution, and b) element first principal stress distribution for the C-Sphere specimen, using the fine mesh model with the elements within the high stress concentration zone (under the load) carved out. ....	47
Figure 3-10: Effective volume in relation to Weibull modulus. ....	48
Figure 3-11: Effective area in relation to Weibull modulus. ....	48
Figure 3-12: C-Sphere specimens as received from contract manufacturer .....	49
Figure 3-13: C-Sphere surface strength testing .....	49
Figure 3-14: Special jig to position C-Sphere on the test cell .....	49
Figure 3-15: Fractured specimen .....	49
Figure 3-16: C-Sphere Weibull strength distribution of NBD200 and SN101C Silicon Nitride .....	50
Figure 3-17: Fractography of NBD200 specimen number 5 at 50x and 1000x respectively .....	51
Figure 3-18: Fractography of NBD200 specimen number 7 at 50x and 1000x respectively .....	51
Figure 3-19: Crack initiation location .....	52
Figure 3-20: Crack initiation origin .....	52
Figure 3-21: C-Sphere Weibull Strength Distribution of Ceralloy Specimens .....	52
Figure 3-22: Definition of angles of failure location .....	53
Figure 3-23: Actual failure stress in relation to failure location angle .....	54
Figure 4-1: Quasar International Resonance Ultrasound Spectroscopy. ....	56
Figure 4-2: Schematic of RUS measurement .....	57
Figure 4-3: RUS Spectrum .....	58
Figure 4-4: A unique combination of elastic properties satisfies both resonance frequencies .....	60
Figure 4-5: Elastic properties of Ceralloy 147-31N SRBSN measured from RUS Spectroscopy .....	60
Figure 4-6: Elastic properties of three HIPed Silicon Nitrides. ....	61
Figure 4-7: The normal distribution of elastic properties measured on three commercial grade HIPed Silicon Nitrides .....	61
Figure 4-8: The effect of Young's modulus on Hertzian contact stress .....	62
Figure 4-9: Three types of residual stresses classified by the length scale .....	63

Figure 4-10: The penetration and measured volume on Silicon Nitride using XRD technique .....	64
Figure 4-11: XRD machine .....	64
Figure 4-12: XRD machine specimen chamber .....	65
Figure 4-13: Residual stress of SRBSN specimens with three surface finishing conditions .....	67
Figure 4-14: Comparison of average residual stress of specimens with three surface finishing conditions .....	68
Figure 4-15: Coarse specimen with different sampling time .....	68
Figure 5-1: The schematic of four-ball contact .....	69
Figure 5-2: Four ball contact geometry .....	70
Figure 5-3: Ball-on-Rod contact geometry .....	71
Figure 5-4: Negative slip of ball-ball contact of modified four ball machine (Hadfield 1993). .....	74
Figure 5-5: Plint TE 15 impact tester .....	75
Figure 5-6: Fixed contact ball .....	75
Figure 5-7: Schematic of artificial crack creation .....	76
Figure 5-8: Artificial crack under UV light .....	76
Figure 5-9: Crack gap under SEM .....	77
Figure 5-10: Crack as visualised on Zygo interferometer .....	77
Figure 5-11: Positioning of cracks in the contact path of four-ball contact (Wang and Hadfield 2002). .....	77
Figure 5-12: Contact geometry changed due to wear of Silicon Nitride .....	79
Figure 5-13: Contact stress reduction due to contact geometry change .....	79
Figure 5-14: Contact path profile of RCF rod with coarse surface condition .....	80
Figure 5-15: Contact path profile of RCF rod with fine surface condition .....	80
Figure 5-16: Contact path profile of RCF rod with RCF-conventional surface condition .....	81
Figure 5-17: Contact path profile of RCF ball with coarse surface condition .....	81
Figure 5-18: Contact path profile of RCF ball with fine surface condition .....	82
Figure 5-19: Contact path profile of RCF ball with RCF-conventional surface condition. ....	82
Figure 5-20: Wear volume loss comparison of three surface finishing conditions .....	82
Figure 5-21: Profile of 30 degree crack seen on a Zygo interferometer .....	83
Figure 5-22: 30 degree artificial crack – 0 minutes. ....	84
Figure 5-23: 30 degree artificial crack – 0 minute .....	84
Figure 5-24: 30 degree crack after 31 minutes .....	84
Figure 5-25: 30 degree crack after 130 minutes .....	84
Figure 5-26: 60 degree crack – after 0 minutes .....	85
Figure 5-27: 60 degree crack – after 0 minutes .....	85
Figure 5-28: 60 degree crack – after 15 minutes .....	85
Figure 5-29: 60 degree crack - after 45 minutes .....	85
Figure 5-30: Weibull analysis of RCF test results of coarse, fine and RCF-conventional conditions. ....	87
Figure 5-31: Coarse-01 .....	87
Figure 5-32: Coarse-02 .....	87
Figure 5-33: Coarse-03 .....	87

Figure 5-34: Coarse-05 .....	87
Figure 5-35: Fine 01 .....	88
Figure 5-36: Fine 03 .....	88
Figure 5-37: Fine-04 .....	88
Figure 5-38: Fine-05 .....	88
Figure 5-39: RCF-Conventional-01 .....	88
Figure 5-40: RCF-Conventional-03 .....	88
Figure 5-41: RCF-Conventional-04 .....	89
Figure 5-42: RCF-Conventional-02 .....	89
Figure 5-43: Fine-02 .....	89
Figure 5-44: Fine-02 .....	89
Figure 5-45: Relationship between absolute viscosity and temperature for three lubricants .....	91
Figure 5-46: Temperature profile of four-ball machine at room temperature and elevated temperature .....	91
Figure 5-47: Pressure-viscosity relationship at 40 degrees .....	92
Figure 5-48: Pressure-viscosity relationship at 100 degrees .....	93
Figure 6-1: Secondary crack creation mechanism .....	97
Figure 6-2: Spall formation mechanism .....	97
Figure 6-3: SEM images of secondary crack creation .....	98
Figure 7-1: Plasma etching machine .....	101
Figure 7-2: Plasma etching machine control panel .....	102
Figure 7-3: Plasma etching chamber .....	102
Figure 7-4: Half RCF rod coarse 01 .....	103
Figure 7-5: Half RCF rod coarse 02 .....	103
Figure 7-6: Half RCF rod coarse 03 .....	103
Figure 7-7: Half RCF rod coarse 04 .....	104
Figure 7-8: Half RCF rod coarse 05 .....	104
Figure 7-9: Half RCF rod coarse 06 .....	104
Figure 7-10: Half RCF rod coarse 07 .....	105
Figure 7-11: Half RCF rod coarse 08 .....	105
Figure 7-12: Half RCF rod fine 01 .....	106
Figure 7-13: Half RCF rod fine 02 .....	106
Figure 7-14: Half RCF rod fine 03 .....	106
Figure 7-15: Half RCF rod fine 04 .....	107
Figure 7-16: Half RCF rod fine 05 .....	107
Figure 7-17: Half RCF rod fine 06 .....	107
Figure 7-18: Half RCF rod fine 07 .....	108
Figure 7-19: Half RCF rod fine 08 .....	108
Figure 7-20: Half RCF rod RCF-conventional 01 .....	108
Figure 7-21: Half RCF rod RCF-conventional 02 .....	109
Figure 7-22: Half RCF rod RCF-conventional 03 .....	109
Figure 7-23: Half RCF rod RCF-conventional 04 .....	109
Figure 7-24: Half RCF rod RCF-conventional 05 .....	110
Figure 7-25: Half RCF rod RCF-conventional 06 .....	110
Figure 7-26: Half RCF rod RCF-conventional 07 .....	110

Figure 7-27: Half RCF rod RCF-conventional 08 .....	111
Figure 7-28: C-Sphere SRBSN coarse 06.....	112
Figure 7-29: C-Sphere SRBSN coarse 07.....	113
Figure 7-30: HIPed NBD200 specimen 07 .....	114
Figure 7-31: Figure 7-32: HIPed NBD200 specimen 05 .....	115
Figure 7-33: A. plastic guard; B. middle plate, lower plate and spring assembly; C. small plastic guard; D. bearing cups; E. bolts and nuts assembly; F. nut; G. testing specimen; H. plastic guide; I. pick-up accelerator; J. copper container and steel balls; K. upper plate with bearing cup.....	117
Figure 7-34: Ball on rod tester test head.....	118
Figure 7-35: Calibration: measurement of the gap between middle plate and lower plate. ....	118
Figure 7-36: Calibration: apply a known load to the spring. ....	119
Figure 7-37: Contact geometry of ball-on-rod tester .....	120
Figure 7-38: Correction factors plotted against $(R'/R'')^{1/2}$ (Johnson 1987).....	121

## List of Tables

Table 1-1: Selected material properties of typical structural ceramic compared to traditional bearing steel.....	3
Table 2-1: Mechanical properties of Silicon Nitride compared. * Data acquired from manufacturer’s data sheet; † Data acquired from resonance ultrasound spectroscopy measurement. ....	19
Table 2-2: Surface profile of core drill finished Silicon Nitride balls. ....	25
Table 2-3: Material finishing parameters in the lapping and polishing steps. ....	29
Table 2-4: Finishing rates of Spheric-Toshiba Silicon Nitride ball blanks.....	31
Table 2-5: Finishing rate (materials removal rate) of SRBSN ball blanks .....	33
Table 2-6: Material removal rates at the polishing step.....	34
Table 4-1: Comparison of three techniques broadly used to measure elastic properties of materials.....	56
Table 4-2: Residual stress of coarse SRBSN specimen.....	66
Table 4-3: Residual stress of coarse specimen with 120 seconds sampling time .....	66
Table 4-4: Residual stress of fine SRBSN specimen.....	66
Table 4-5: Residual stress of RCF-conventional specimen .....	66
Table 5-1: Comparison between modified four-ball machine and ball-on-rod machine..	73
Table 5-2: RCF results of Ceralloy 147-31N SRBSN .....	86
Table 5-3: Properties of three selected lubricants.....	90
Table 5-4: Pressure viscosity coefficient of the lubricants .....	92
Table 5-5: RCF performance of lapped SRBSN balls studied on modified four-ball machine with three different lubricants.....	93
Table 7-1: Relationship between machine loading and contact stress on four-ball machine .....	116
Table 7-2: Relationship between spring loading and contact stress on ball-on-rod machine .....	122

# Acknowledgement

I am extremely grateful to Professor Mark Hadfield without whom, I would not have completed the project and thesis successfully. His kind supervision and guidance always gave me immediate enlightenment whenever I encountered difficulties in the project. He was always encouraging and offered advice whenever I felt low in energy.

I want to thank Dr Andrew Wereszczak for his supervision while I was away visiting Oak Ridge National Laboratory. His indepth knowledge in engineering ceramics made my visiting research in ORNL extremely rewarding. His help in life also made my relocation to Tennessee trouble free.

I am indebted to ORNL and the School of Design, Engineering and Computing who kindly provided funding for my Ph.D project. Without their financial support, the completion of the project would not have been possible.

I also want to thank my family, especially my wife, who have been very supportive during these past few years while I was pursuing my Ph.D study.

# CHAPTER 1: INTRODUCTION

## 1.1 Background

Technical ceramics, also known as structural ceramics or engineering ceramics, are a group of ceramic materials used or which potentially could be used in engineering applications, such as fuel cell, hydrogen storage, artificial hip replacement, advanced rolling element bearings, etc. Rolling contact applications is one of those areas where technical ceramics have made important contributions due to their excellent mechanical properties. Technical ceramics which have been considered for rolling contact applications include Alumina ( $\text{Al}_2\text{O}_3$ ), Zirconia ( $\text{Zr}_2\text{O}_3$ ), Silicon Carbide (SiC), Silicon Nitride ( $\text{Si}_3\text{N}_4$ ), etc. However, Silicon Nitride has been widely recognised to be the best candidate for rolling contact applications as a replacement for conventional high hardness steel. Table 1-1 compared the properties of Silicon Nitride with those of M-50 steel, which is the most widely used bearing steel. As described in Table 1-1, apart from the relatively lower fracture toughness, technical ceramics offer a combination of higher hardness, lower density, better suitability in high temperature applications and better corrosion resistance compared with M-50 steel. All of these properties are desirable for advanced rolling contact design and application. Demonstration tests show that all these four technical ceramics have good rolling contact fatigue properties, however, SiC and  $\text{Al}_2\text{O}_3$  fail due to fracture which is a catastrophic mode of failure undesirable for rolling contact applications, especially for bearing applications. Zirconia offers similar properties to Silicon Nitride, but defect-free zirconia is hard to fabricate and economically very expensive. Considering all these factors, Silicon Nitride is the most suitable material to replace conventional steel material in rolling contact applications.

Broadly speaking, conventional bearing failures can be classified into three categories, abrasion, fatigue and pressure-induced welding. Abrasion can be a result of bearing contamination or bearing wear where hard particles are in contact with the bearing material. Fatigue, i.e. rolling contact fatigue, occurs when the bearing is cyclically loaded to the point that it exceeds its fatigue life. Pressure-induced welding can be caused by lubricant starvation or local high contact stress which leads to metal on metal contact. On

the modified four-ball machine and ball-on-rod machine, all these three failure modes can be replicated. However, as Silicon Nitride is particularly sensitive to rolling contact fatigue failure originating from surface cracks, bench testing is normally carried out in a controlled environment where rolling contact fatigue leads to failures.

For conventional bearings in aerospace industry applications, a very low proportion of bearing failure is actually attributed to rolling contact fatigue. Normally bearing failures are caused by high stresses originating from special causes (for instance, bearing load crossover). However, as Silicon Nitride rolling element bearings improve performance in hostile environments, such as lubricant starvation, high temperature and high contact stresses, it is therefore particularly vulnerable to rolling contact fatigue originated from surface cracks (natural or from machining). The rolling contact fatigue properties of Silicon Nitride are therefore of particular interest in the present study.

Improvement in Silicon Nitride processing technology enables economic fabrication of densified Silicon Nitride with minimum porosity. As a typical technical ceramics, it has offered high hardness, low density, corrosion resistance, low thermal expansion and good high temperature strength. In addition it also offers wear resistance and good performance under hostile lubricating environment.

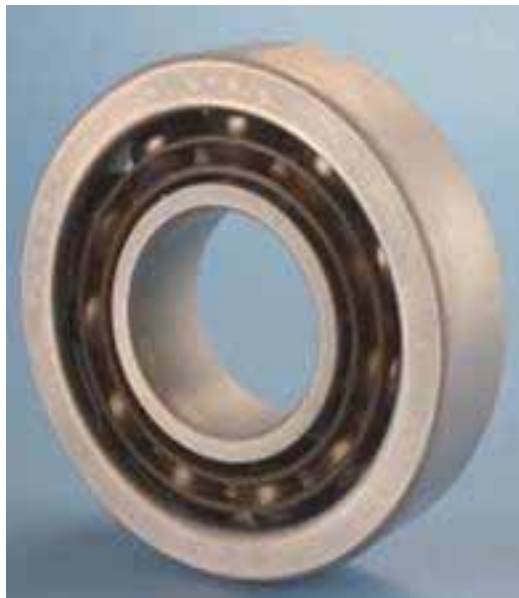
Material	Processing	Hardness ( $\text{kg mm}^{-2}$ )	Fracture Toughness ( $\text{MPa m}^{-1/2}$ )	Elastic Modulus (GPa)	Density ( $\text{g cm}^{-3}$ )	Application Temperature (C)	Corrosion Resistance
M-50 Steel	Wrought	800	18-20	210	8	<325	Moderate
Zirconia	Sintered and Transformation Toughened	1300	14	205	5.6	<900	Good
$\text{Al}_2\text{O}_3$	Fully Dense Sintered	2000	5	385	4	<1000	Good
SiC	Sintered	2800	4	410	3.1	<1400	Good
$\text{Si}_3\text{N}_4$	Hot Pressed	1800-2000	5-7	310	3.2	<1100	Good

Table 1-1: Selected material properties of typical structural ceramic compared to traditional bearing steel.

This unique combination of properties makes Silicon Nitride an excellent material for bearing applications. Hybrid bearings, which use a combination of steel race and Silicon Nitride rolling elements, can be found in applications in the aerospace, automotive and power generation industries. Figure 1-1 and Figure 1-2 below show the ball bearing element and hybrid bearing respectively.



**Figure 1-1: Silicon Nitride ball bearing element. (SKF)**



**Figure 1-2: Hybrid ceramic bearing with Silicon Nitride rolling element and steel race. (SKF)**

Silicon Nitride can contribute to improved energy efficiency, prolonged component life and is more environmentally friendly. These characteristics of Silicon Nitride are

especially attractive to diesel engine manufactures and power industry and bearing applications. During the past two decades, Silicon Nitride processing and machining techniques have been significantly improved through research and development funded by government initiatives and industry participants. This has enabled limited application of high performance Silicon Nitride components, such as diesel engine exhaust valves, fuel pump rollers, cam roller followers, etc. Some typical diesel engine components are shown in Figure 1-3 and Figure 1-4.

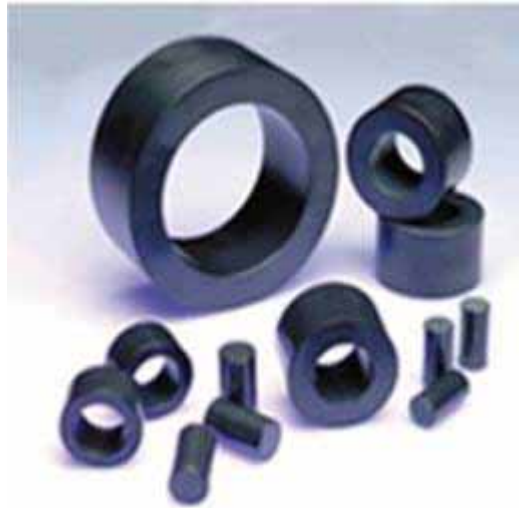


**Figure 1-3: Silicon Nitride diesel engine component. (Ceradyne Co.)**



**Figure 1-4: Ceramic components made from SRBSN material. (Ceradyne Co.)**

The superiority of Silicon Nitride in rolling contact applications has convinced manufacturers in automotive, power and aerospace industries to develop more

applications to realise better performance and energy savings. However, the knowledge of contact reliability and cost-effectiveness of Silicon Nitride is limited which prohibits its mass market application. The current project focuses on the examination of the relationship between surface/subsurface qualities of Silicon Nitride material and its contact reliability. The contact reliability of ceramics is normally examined on rolling contact fatigue (RCF) bench testers. Different test configurations are used across the world, such as ball-on-flat tests in Japan, four-ball tests in Europe and ball-on-rod test in United States. However, the individual test methods are confined by geographical boundary, there is no inter-laboratory study to compare the results acquired from different testing methods. As a result of this, there is no international standard to study rolling contact fatigue, which is a significant factor affecting mass market applications of Silicon Nitride. Apart from lacking unified RCF test standards, most of the previous studies were performed on hot isostatically-pressed Silicon Nitride, such as Norton and Toshiba commercial Silicon Nitride. These are more expensive than sintered and reaction bonded Silicon Nitride, which is a recently developed processing technique. SRBSN, such as Ceralloy 147-31N, has comparable strength and densities to HIPed Silicon Nitride, but is significantly cheaper to produce. However, knowledge of contact reliability of SRBSN is more limited, and the cost-effectiveness of SRBSN cannot be materialised without this knowledge.

## 1.2 Literature Review

### 1.2.1 Silicon Nitride Material

Silicon Nitride was traditionally manufactured through hot pressing process, which further developed into hot isostatical pressing (HIP) (Bocanegra-Bernal 2004) in order to improve the mechanical property of fabricated Silicon Nitride. This method was developed to produce Silicon Nitride with higher density and lower porosity.  $\alpha$ - $\text{Si}_3\text{N}_4$  raw powder was used as the starting material in addition to some sintering additives to produce bulk Silicon Nitride in a confined space of graphite die under a hot, nitrogen environment (Terwilliger 1974; Terwilliger and Lange 1975). X-ray Diffraction pattern could indicate the transformation of  $\alpha$ -phase to  $\beta$ -phase occurred during the sintering process (Bhandhubanyong and Akhadejdamrong 1997). HIPed Silicon Nitride could

achieve density nearly to theoretical density, which resulted in good fracture toughness and surface hardness. Although HIPed Silicon Nitride has very good mechanical properties, the high material cost (i.e. raw Silicon Nitride powder cost) prevents its use in widespread applications.

Sintered and reaction-bonded Silicon Nitride (SRBSN) is a processing method developed to produce Silicon Nitride at relatively low cost without significant sacrifice of strength. SRBSN is formed by a two step process – reaction bonding and post-bonding sintering. Reaction-bonded Silicon Nitride (RSBN) processing is a method to produce Silicon Nitride material through incorporation and nitridation of silicon powders, which was mainly developed in the 1950s (Riley 2000). It uses silicon powder as the raw material and fabricate silicon nitride through direct nitridation process. Metallurgical grade silicon powder is more cost-effective compared with metallurgical grade Silicon Nitride powder where is used as raw material for HIPed silicon nitride. The reaction bonding process produces porous Silicon Nitride with weak mechanical properties, and therefore a sintering process is required to induce densification process in order to produce silicon nitride with 93 to 99% theoretical density. The resulting mechanical property of SRBSN is comparable to hot pressed Silicon Nitride (Lee, Mun et al. 2004; Muller, Bauer et al. 2009; Muller, Rogner et al. 2009). The microstructure of SRBSN can be affected by a range of parameters such as nitridation temperature, silicon powder size, sample size, sintering aid (Xu, Luo et al. 2008) and dwell time.

The sintering and densification of Silicon Nitride requires sintering aids and high density low porosity Silicon Nitride is difficult to achieve due to the strong covalent bonding between silicon and nitrogen. Figure 1-5 shows the rod like porous SRBSN fracture surface microstructure. Alternative sintering process was investigated by using Silicon Nitride powder as seed powder, and silicon powder as raw material to fabricate SRBSN through nitridation process. This process formed a microstructure with elongated grains distributed in the smaller grain structure, which helps to improve the mechanical strength of SRBSN (Lee, Mun et al. 2003).

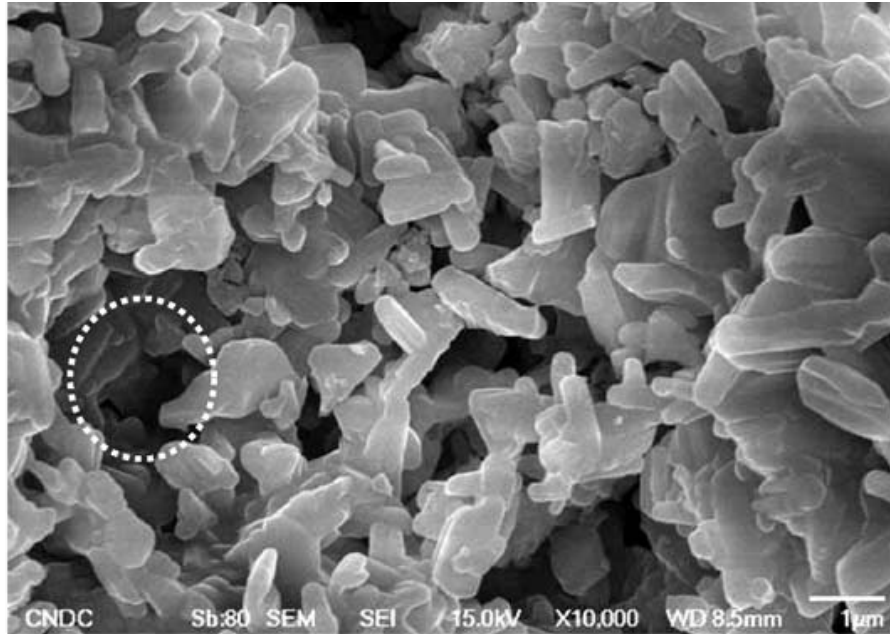


Figure 1-5: SEM image of SRBSN fracture surface showing porosity (Tuyen, Park et al. 2009)

### 1.2.2 Rolling Contact Fatigue Test

Research over the past three decades has developed Silicon Nitride into practical applications of rolling contact bearing (Katz 1985; Chao and Shetty 1995; Wang, Snidle et al. 2000) and selected rolling contact applications in diesel engine components. Rolling contact fatigue performance of material can be evaluated through either full-scale bearing testing or laboratory bench testing. Full-scale testing is complex to set up, so in practice various types of tribotesters are used to study RCF. Many types of test-rigs are used to study rolling contact fatigue performance of ceramics. Typically, in such tests, a detector coupled with a shutdown device is used to monitor the vibration of the assembly. When a preset vibration level is reached, indicating the formation of a spall of excessive uneven wear, the test is automatically stopped and the lifetime of the test is recorded. Alternatively, the tests are suspended at different durations to study the wear rate.

Modified four-ball testers and ball-on-rod testers are widely used in the United Kingdom and United States respectively, and their characteristics and applications are reviewed in detail in the following sections. Apart from these two types of testers, the RCF performance of ceramics and other materials was also studied on a Ball-on-Plate (Ball-on-Flat) tester (Kikuchi, Yoshioka et al. 1984; Fujiwara, Yoshioka et al. 1989), Disc-on-

Rod Machine (Baumgartner 1974; Cowley and Lueck 1979) and Contacting Ring (Cylinder-on-Cylinder) Machine (Otsuka, Sugawara et al. 1994) (Akazawa and Kato 1988; Akazawa, Kato et al. 1989; Braza, Cheng et al. 1989). Alternatively, the contact durability tests were carried out to study the tribological properties of a few hot pressed Silicon Nitrides (Kelina, Tkacheva et al. 2005).

Recently, the RCF of Silicon Nitride balls was also studied on a newly developed pure rolling fatigue test rig with three contact points, which showed that the sub-surface cracks played a dominant role in the development of spall failure (Bocanegra-Bernal 2004; Zhou, Wu et al. 2007; Zhou, Wu et al. 2007; Zhou and Wu 2009). This is consistent with the research findings from the experiments carried out on the four-ball machine, which is discussed in detail in Section 1.2.2.1.

Apart from the experimental studies of the RCF of Silicon Nitride, the fatigue life models and fracture mechanics models to predict the crack initiation, crack propagation and fatigue life of Silicon Nitride were also developed (Levesque and Arakere; Abe, Niizeki et al. 1988; Wang and Hadfield 2000; Wang and Hadfield 2000; Wang and Hadfield 2003; Levesque and Arakere 2008; Zhou, Wu et al. 2009). However, the main focus of this thesis is to study the RCF of Silicon Nitride through an experimental approach, therefore the analytical and numerical modellings of RCF and crack propagation are not further reviewed. Instead, the studies carried out on the experimental rigs are reviewed in detail in the following sub-sections.

#### 1.2.2.1 Four-Ball Test

In a modified four-ball/five-ball tester, a model contact consisting of three lower balls driven by a fourth contacting upper ball simulates conditions within a standard deep-groove ball bearing. The upper ball models the bearing race, while the cup simulates the bearing outer race and the three planetary balls represent the balls within a ball bearing. The machine has a proven history as being useful to investigate the rolling contact fatigue resistance of materials under various tribological conditions. Previously, this machine has been mainly used as an accelerated method to measure the rolling contact fatigue of

bearing steels by various researchers. The influence of lubrication type on steel ball rolling contact fatigue was also evaluated using the machine (Scott; Barwell and Scott 1956; Krivoshein 1960). The institute of Petroleum gathered a range of papers (Tourret and Wright 1976), which describes various test results, ball dynamics and kinematics using the modified four-ball machine. Recently, the modified four ball machine (Hadfield, Stolarski et al. 1993; Hadfield, Stolarski et al. 1993; Hadfield 1998; Thoma, Rohr et al. 2004; Kida, Kitamura et al. 2005; Karaszewski 2008) have been used to simulate the rolling contact in hybrid ball bearings and study the fatigue crack propagation.

The five-ball test assembly is similar to a four-ball one. It consists of a driven test ball on top of four lower balls positioned by a separator, in the form of a pyramid. The four lower balls rotate in a race driven by the upper ball, thus simulating the rolling and sliding produced in angular contact ball bearing. This five-ball machine has been used to investigate the fatigue life of high-speed ball bearings with hot pressed Silicon Nitride balls (Parker and Zaretsky 1975; Roosen and Carter 1998).

#### 1.2.2.2 Ball-on-Rod Test

The ball-on-rod bench tester was first developed by the Ball and Roller Bearing Group of Federal-Mogul, and the design detail was described by D. Glover (Glover 1982). Three steel balls, 12.7 mm in diameter, orbit a rotating 9.53 mm diameter cylinder test specimen. A precision collet was used to hold the testing rod in a strict vertical position. Cowley defined a standardised method to finish the testing rods which was used on this tester. The procedure, including cut per pass and total thickness removed at rough, intermediate and finish grinding stage was detailed by Chao (Chao, Lakshminarayanan et al. 1995). The thrust load on the bearing cups is applied mechanically by forcing the upper cup towards the lower cup with three precalibrated coil springs in the assembly. The rod specimen is rotated by a direct-drive electric motor mounted in line with the specimen below the table. The three balls are, in turn, driven by the rod and rotate around the rod. Lubricant is supplied by drip feed onto the top of the rod. This machine had been employed to study rolling-contact wear performance of the steel ball and Silicon Nitride rod contact and all ceramic contact (Lakshminarayanan, Chao et al. 1997; Chao,

Lakshminarayanan et al. 1998). Wear performance of several Silicon Nitride materials was investigated using this machine (Lueck 1990). The effects of microstructure, composition and physical properties on rolling-contact wear and fatigue performance were also studied respectively on this machine by researchers (Allen 1994; Burrier 1996). A Japanese type of ball-on-rod tester was used to investigate RCF performance of ceramics by Nishihara (Nishihara 1988). In this method, two balls each in 12.7 mm diameter, are supported by three rollers which are pressed against a bearing steel rod. The specimen receives 1,200,000 stress cycles per hour when driven at 10,000 rpm. Earlier work using this machine was performed by researchers (Baumgartner 1974; Cowley and Lueck 1979). The ball-on-rod tester was also used by Trivedi (Trivedi, Massey et al. 2001; Trivedi and Saba 2001) to study the lubricant performance. It is also modified by attaching a heating chamber to investigate the lubricants at elevated temperatures.

### 1.2.2.3 Rolling Contact Wear

Rolling contact wear of Silicon Nitride was studied (Akazawa 1986; Asada, Hashimoto et al. 1992) on a contact ring tester under dry contact. Ring specimens of Silicon Nitride were cold pressed in air and then heat treated. A two-state wear mechanism, including initial severe state and steady state was observed, with wear coefficients in the order of  $10^{-6}$  and  $10^{-8}$  respectively. Braza studied three types of Silicon Nitride using a similar contact ring tester, but it used Silicon Nitride and cast iron contact instead of only Silicon Nitride contacts. The highest wear rate was observed on reaction bonded Silicon Nitride.

Rolling contact wear was also observed on a Ball-on-Rod tester using a hybrid contact of steel rod and Silicon Nitride balls (Lakshminarayanan, Chao et al. 1997; Chao, Lakshminarayanan et al. 1998). Five types of Silicon Nitride were tested with turbine oil as lubricant. Results showed that two Hot Isostatically Pressed (HIPed) specimens had the lowest wear rates. Pressureless sintered sialon has a wear rate 1000 times of HIPed Silicon Nitride. The same type of tester was also used (Chao, Lakshminarayanan et al. 1998) to study rolling contact wear of lubricated Silicon Nitride and Silicon Nitride contact. The wear of Silicon Nitride elements was concluded to be transient, dependent on initial surface roughness of the elements. In addition, the terminal loss increased with

the contact stress. Seven HIPed Silicon Nitride balls with different surface roughness were tested against steel balls under lubricated contact with a maximum stress of 6.58 GPa. Terminal wear volumes in the range of  $0.3-3 \times 10^{-10}$  were observed among these specimens.

### 1.2.3 Residual Stress in Silicon Nitride

Residual stress is a type of stress remaining in the body of the material or component while it maintains its equilibrium. It can cause premature failure and shortened lifetime when it coexists with applied stresses. In certain applications, residual stresses are artificially induced to optimise the design of the components, such as the compressive residual stress for pressure vessels. In the case of Silicon Nitride components used in rolling element bearing applications, residual stress can be induced and varied through fabrication and machining, and residual stress in Silicon Nitride can affect the fatigue behaviour under rolling contact.

A physical model (Li, Lei et al. 1999) is set up to demonstrate the generation of residual stress during the fabrication of reaction bonded Silicon Nitride. The residual stress arises during the cooling of a partially reacted powder with different thermal expansions between core and surface layer. The residual stress induced by the fabrication process can be measured through X-ray diffraction (Guo, Li et al. 2007) and the macroscopic residual stress was the result of the volume changes through the phase transformation. In the microscopic scale, the residual stress resulted in flaws through strain contract and transgranular cracks in the grain.

The residual stress in Silicon Nitride can also be introduced through machining process. The residual stress can be formed at the surface layer of the specimen following machining, which is a result of the elastic recovery of core material being constrained by the surface layer which experiences plastic deformation (Ren, Wang et al. 2002). Kang studied the effect of machining parameters on the residual stress (Kang, Hadfield et al. 2002), which concluded that the compressive residual stress was proportional to the lapping load. The residual stresses were also measured on pre-tested and failed Silicon

Nitride balls to study the impact of residual stresses on the RCF (Hadfield and Tobe 1998; Khan, Hadfield et al. 2005; Khan, Hadfield et al. 2006), and it has been concluded that the compressive residual stresses were relieved with the RCF cycle counts increasing. The compressive residual stress value was low where the spall failure was formed, which indicated that it was relieved as a result of the subsurface damage leading into spall failure.

#### 1.2.4 Materials Characterisation

Many techniques have been utilised to characterise the pre- and post- RCF test specimens in order to give an intrinsic explanation of rolling contact fatigue properties of Silicon Nitride ceramic materials. Non-destructive testing methods are widely used, including fluorescent dye penetration, resonance ultrasound spectroscopy, scanning acoustic microscopy and many more. Destructive techniques, such as flexure strength, crush strength, and C-Ring strength are also used to evaluate the candidate material to demonstrate the intrinsic material properties.

##### 1.2.4.1 Destructive Evaluation

Previous testing has revealed a high correlation between the fatigue life of a bearing and the crushing strength of the rolling elements. A Japanese JIS B1501 standard test was performed by Nishihara (Nishihara 1988), a distinct trend was evident although there was a high scatter on data. It implies that a crushing test can serve as a substitute for proof testing of rolling bearing elements.

At an early stage in the development of ceramic rolling contact bearings, flaking fatigue tests of ceramic balls were carried out using a fatigue test setup for radial contact ball bearings (Abe, Niizeki et al. 1988). Six different types of Silicon Nitride were tested and only two of these samples exhibited longer lives than those of steel balls (Abe, Niizeki et al. 1988). Flaking was recognised as the result of crack propagation, either from internal flaws or inclusions. SEM and EDX analysis identified the origin of flaking as the segregation of sintering additives or metallic inclusions during the manufacturing process.

The C-Ring test was traditionally used to examine the strength and subsurface damage of tubular components (Wereszczak, Caspe et al. 2003). Four types of engineering ceramics including Silicon Nitride were C-Ring tested according to ASTM C1323 to help facilitate design and reliability modelling with each type of ceramic. The investigated Silicon Nitride and zirconia were found to exhibit higher uncensored characteristic strengths than the alumina and silicon carbide.

#### 1.2.4.2 Non-Destructive Evaluation

Acoustic methods have been widely used in defect characterisation of ceramic materials. Scanning acoustic microscopy was employed by Hadfield (Hadfield and Stolarski 1995) to quantify incipient delaminated subsurface crack depth. This technique is especially useful for subsurface crack observations of ceramics which are traditionally difficult to analyse experimentally (Hadfield, Tobe et al. 1994). The acoustic waves penetrate to a certain depth of the subsurface and the reflected acoustic waves are collected by the receiver. The depth and size of the defect can be quantitatively determined from the micrograph generated from the acoustic waves.

Hsieh et al. (Hsieh and Khuriyakub 1992; Hsieh and Khuriyakub 1993) developed the resonant sphere technique to characterise ceramic ball-bearing elements, which utilised the surface wave to examine the surface defect population. The resonance quality factor (Q) decreases in surface wave mode due to the existence of surface defect.

A method of locating the position of acoustic emission sources has been applied to identify the position of crack initiation in RCF by Yoshioka et al. (Yoshioka and Takeda 1994). The positions of crack initiation were widely spread and did not always coincide with the theoretical prediction, which assumed that a crack initiates at the depth of the maximum orthogonal shear stress. Further improving the Yoshioka technique may offer the possibility of identifying the onset of crack propagation in a non-destructive manner, leading to higher reliability of rolling bearings in service.

#### 1.2.5 Machining Damage and Strength of Silicon Nitride

Research by Wang (Ahmed and Hadfield 1996; Wang and Hadfield 1999; Wang and Hadfield 1999; Wang and Hadfield 2000; Wang and Hadfield 2000; Wang and Hadfield

2000; Wang and Hadfield 2001; Wang and Hadfield 2002; Wang and Hadfield 2003; Wang and Hadfield 2003; Zhao, Hadfield et al. 2003) discovered that surface defects significantly affect the rolling contact fatigue lives of Silicon Nitride. Ring cracks are the most commonly found natural cracks on commercial Silicon Nitride balls. It is believed they are produced during the machining process.

Research by Kang (Kang and Hadfield 1999; Kang, Hadfield et al. 2000; Kang and Hadfield 2001; Kang and Hadfield 2001; Kang and Hadfield 2002) studied the Silicon Nitride machining process using an in-house manufactured novel eccentric lapping machine. The finishing rate and the surface quality are affected by the combination of factors such as lapping speed, applied load, abrasives etc.

Research by Jahanmir (Jahanmir 1993) discovered that the machining conditions affect the flexure strength of rod specimens, with coarsely-machined rods having the lowest strength. An extensive study on SRBSN material was coordinated by NIST (Quinn, Ives et al. 2003), which investigated the cracks induced by machining within the sub-surface of the specimens. It also concluded that aggressive machining can cause deep sub-surface damage to the specimen with larger crack length.

### **1.3 State-of-The-Art from Literature Review**

The rolling contact performance of Silicon Nitride material has been extensively studied using various types of tribotesters, of which the four ball tribotester and ball-on-rod tester are most widely used. Research results reveal that the intrinsic property of different types of Silicon Nitride material and the surface quality affects the rolling contact fatigue life of Silicon Nitride. The effect of the machining process on the surface/subsurface quality of Silicon Nitride has also been widely studied, and in particular, there is extensive research in SRBSN carried out by NIST. However, little effort has been made to quantify the effect of surface/sub-surface quality of Silicon Nitride on its rolling contact performance. The aim of this thesis is to fill this gap by examining the RCF performance of Ceralloy 147-31N SRBSN material with different controlled machining conditions.

## 1.4 Scope of Research

The main objective of the research work carried out during the period of this PhD project was to investigate the relationship between subsurface damage and the rolling contact fatigue performance of Silicon Nitride ceramics. The investigation was carried out through the characterisation of Silicon Nitride properties using various techniques, such as C-Sphere strength, Resonance Ultrasound Spectroscopy and Residual Stress. The objective of the research was subsequently divided into several areas and the interlinking of these areas is summarised and set out in Figure 1-5. (1). To examine and compare the microstructure of different types of Silicon Nitride materials; (2). To study the machining process of Silicon Nitride ball bearing elements using a eccentric lapping machine; Quantify the machining effects on residual stress. (3). Quantify the subsurface damage of Silicon Nitride ball bearing elements using flexure strength tests. (4). Compare the RCF results of three batches of Silicon Nitride specimens with different machining parameters. (5). Examine the lubricant effects on RCF test results.

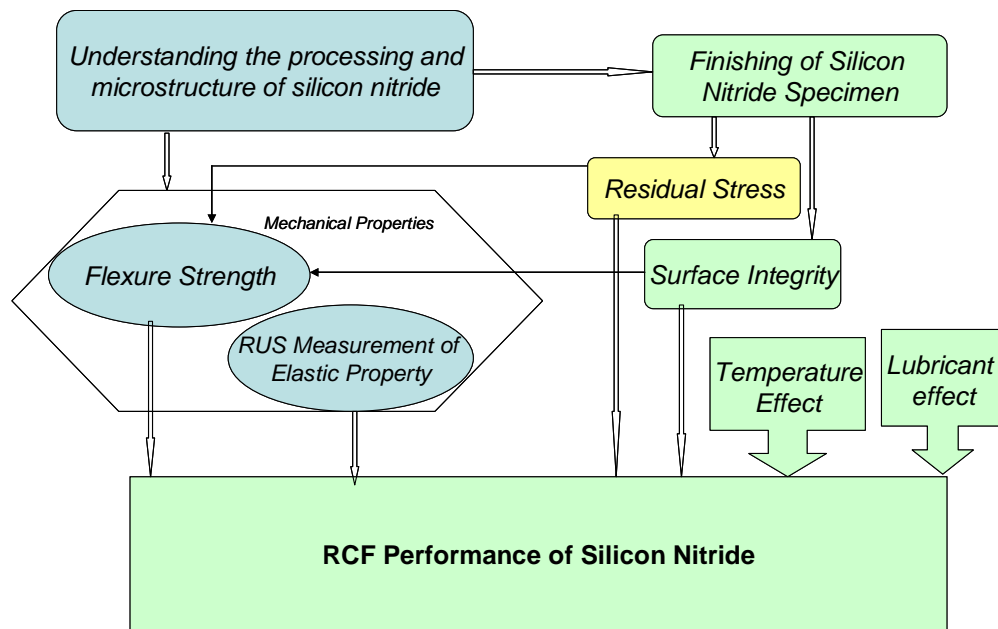


Figure 1-6: Scope of research

## 1.5 Structure of Thesis

The background information of this research work is briefly introduced in Chapter One, including the literature of previous experimental work and characterisation techniques

relating to rolling contact fatigue testing of ceramics. In Chapter Two, the microstructure of various candidate Silicon Nitride materials is examined and compared using plasma etching or thermal mechanical etching techniques. The process of preparing Silicon Nitride ball-bearing element specimens is studied using an in-house manufactured eccentric lapping machine. The surface strength of Silicon Nitride ball and rod specimens are studied in Chapter Three. Chapter Four studies the elastic property and residual stress of Silicon Nitride. Chapter Five discusses the RCF test methodology, including the setup of a four-ball and ball-on-rod tribometer, their contact geometry and the artificial crack generation. The RCF test results and analysis, including effect of lubricants are also discussed in this chapter. The overall discussion and major conclusions from this thesis are included in Chapter Six, which also includes recommendations for future directions of research work in this area.

# CHAPTER 2: SILICON NITRIDE MICROSTRUCTURE AND MACHINING

## 2.1 Silicon Nitride Material

As the microstructure of Silicon Nitride can affect the contact reliability under rolling contact condition, the microstructure of HIPed Silicon Nitride and SRBSN was studied in this thesis. HIPed Silicon Nitride is currently more widely used as a bearing element material in the market than SRBSN Silicon Nitride, primarily because of its perceived superior mechanical properties and mature processing technology. Three grades of HIPed Silicon Nitride material from three major suppliers of HIPed Silicon Nitride are therefore studied in this thesis and compared with SRBSN. These are SN101C from Cerbec, NBD200 from Norton and TSN03-NH from Toshiba. SRBSN is an alternative processing technology which has seen its application in mass production of a range of diesel engine components, including fuel injector cam roller follower and link pin, fuel pump roller and exhaust valve cam roller follower, where their superior rolling contact performance compared with steel components allows engine manufacturers to reduce warranty costs. Insufficient knowledge of rolling contact performance and contact reliability of SRBSN Silicon Nitride prevents its wider application as bearing elements or other typical rolling contact application. A typical SRBSN material, Ceralloy 147-31N materials produced by Ceradyne Co. is investigated in this study.

HIP and SRBSN process have been discussed in Section 1.2.1, and a comparison of mechanical properties of Ceralloy 147-31N and three type of HIPed Silicon Nitride are shown in Table 2-1. As illustrated in the table, all of these materials have similar density, strength, fracture toughness, and elastic properties. However, Ceralloy 147-31N SRBSN is cheaper to produce due to its processing technique, which is a significant advantage in engineering applications.

Properties	Ceralloy 147-31N	Toshiba TSN03H	Saint Gobain NBD200	Saint Gobain SN101C
Density (g/cc)*	3.21	3.22	3.16	3.21
Strength (MPa)*	800	900	900	1000
Fracture Toughness* (MPam <sup>1/2</sup> )	6.0	6.7	5.5	6.5
Elastic Modulus (GPa)†	308	307	321	308
Poisson's Ratio†	0.28	0.28	0.27	0.26

**Table 2-1: Mechanical properties of Silicon Nitride compared. \* Data acquired from manufacturer's data sheet; † Data acquired from resonance ultrasound spectroscopy measurement.**

The microstructures of four types of Silicon Nitride material were studied. The microstructure of Ceralloy 147-31N SRBSN was studied using plasma etching technique, and the results are shown in Figure 2-1. The plasma etching process and equipment used to study the microstructure of SRBSN are described in Appendix 7.1. Ceralloy 147-31N showed a rod like microstructure, which is typical of SRBSN.

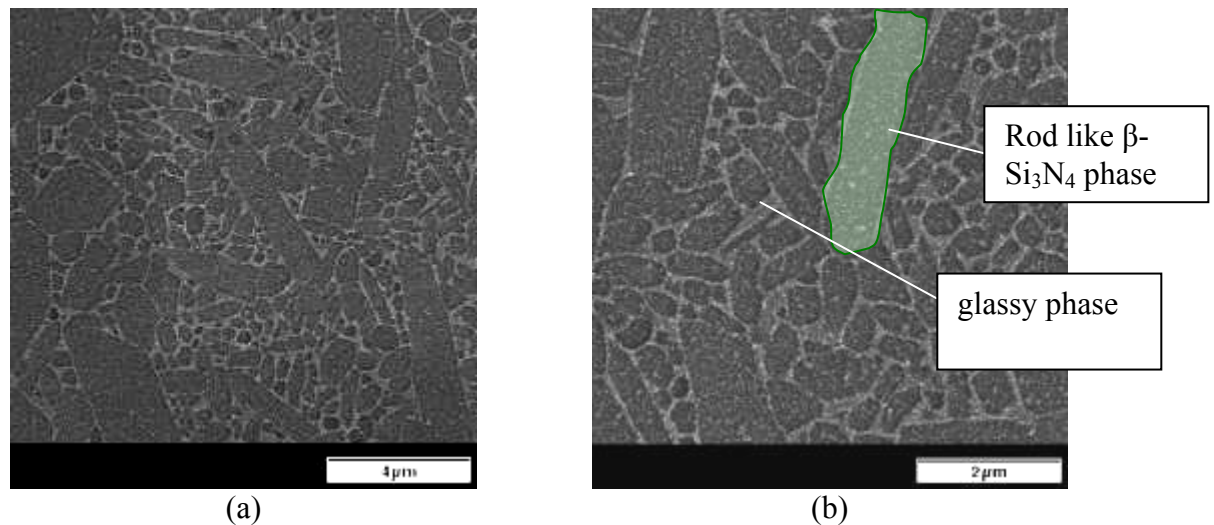


**Figure 2-1: Plasma etched microstructure of Ceralloy 147-31N Silicon Nitride. a. 5000x; b. 10000x;**

The schematic of the rod-like microstructure is shown in Figure 2-2. The rod-like primary phase was evenly distributed within the glassy second phase. The primary phase interlocked with the rest of the microstructure, and this was perceived as the main reason

for improved fracture toughness. The rod-like structure was also thought to be preventing the crack propagation under cyclic loading.

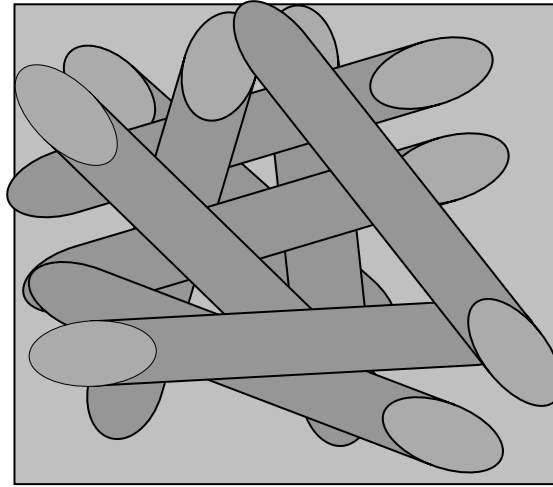


**Figure 2-2: Schematic of Rod-like microstructure**

Plasma etching technique was also practised on three HIPed Silicon Nitride samples but was not as effective as it is applied on SRBSN. Traditional thermal-chemical etching method is then applied to examine the microstructure of HIPed Silicon Nitride instead of the plasma etching technique, and the etched microstructure is shown in Figure 2-3 - Figure 2-5.

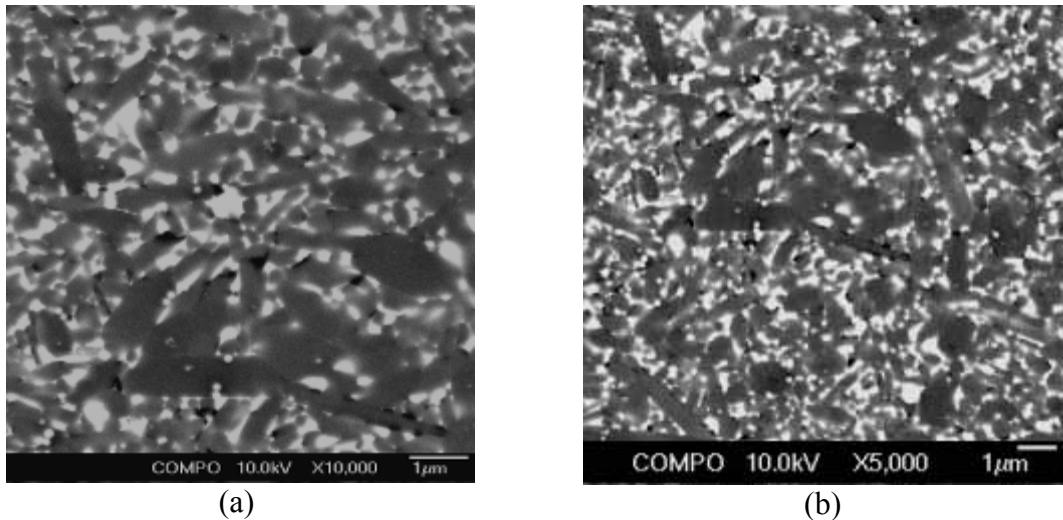


**Figure 2-3: Thermal-chemical etched microstructure of Toshiba TSN03NH Silicon Nitride at different magnification**

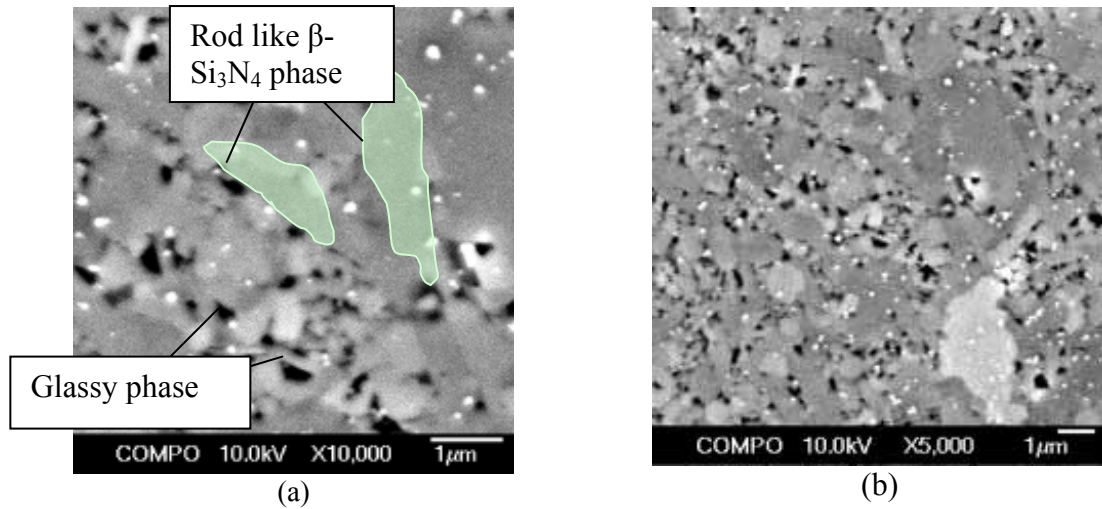


**Figure 2-4: Thermal-chemical etched microstructure of NBD200 Silicon Nitride at different magnification**

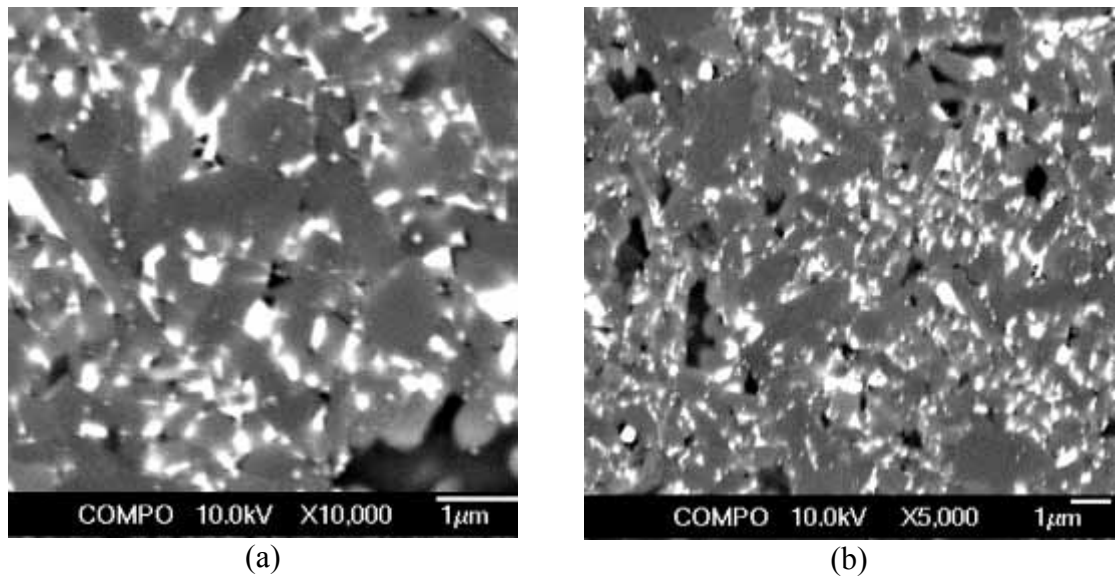


**Figure 2-5: Thermal-chemical etched microstructure of SN101C Silicon Nitride at different magnification**

Both of Ceralloy 147-31N and HIPed Silicon Nitride can achieve a density of 3.1-3.2 g/cc, which represents an improvement in SRBSN which traditionally achieved lower density than HIPed counterpart. This comparable density gave rise to a similar strength, fracture toughness and elastic modulus.

The microstructure of Ceralloy 147-31N is similar to that of TSN03NH and SN101C shown in Figures 2-3 and 2-5, which are both typical of HIPed Silicon Nitride rod-like

grain structure. NBN200 microstructure shown in Figure 2-4 is also believed to be rod like although it was not clearly shown due to the quality of the micrograph. HIPed Silicon Nitride has well-proven tribological and fatigue performance through their bearing applications. Ceralloy 147-31N is believed to have the same intrinsic properties as HIPed, therefore it is believed be a cost-effective alternative of the HIPed Silicon Nitride. If it can be demonstrated with good contact reliability, it is suitable for rolling contact applications at a fraction of HIPed Silicon Nitride's processing cost. The rolling contact fatigue performance of Ceralloy 147-31N is studied in Chapter 5.

## 2.2 Silicon Nitride Machining

### 2.2.1. Grinding of Silicon Nitride ball

In order to examine the machining effect on contact reliability of Silicon Nitride, controlling the surface/subsurface conditions by varying machining parameters is an essential step. The as-sintered Ceralloy 147-31N SRBSN ingot was machined into three batches of 12.7 mm diameter balls with different machining parameters. The difference on machining produced three batches of balls with varying surface and subsurface qualities. The machining parameters were determined by referring to conventional RCF rod finishing for a standard ball-on-rod test. In order to compare the results of the ball-on-rod test and the four-ball test, the Silicon Nitride ball specimens and rod specimens were finished to the same standard. The machining was performed on three diamond dressed core drills as shown in Figure 2-6. These core drills were positioned at 120 degrees to each other, and driven by motors to run simultaneously. Table 2-1 shows the machining procedures applied to coarse, fine and RCF-conventional machining conditions. The grinding of the Silicon Nitride ball was carried out by a machining subcontractor in the United States, as the quality of the machining is crucial to the subsequent tests. However the machining specification (including tolerances) and instruction was defined and provided to the contractor.

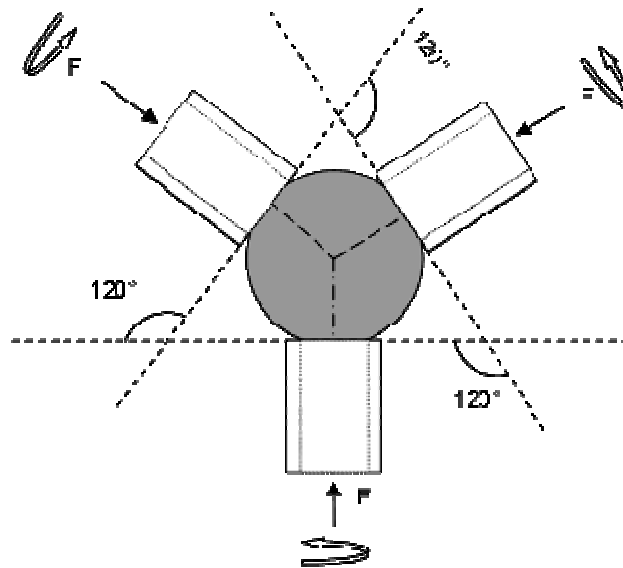
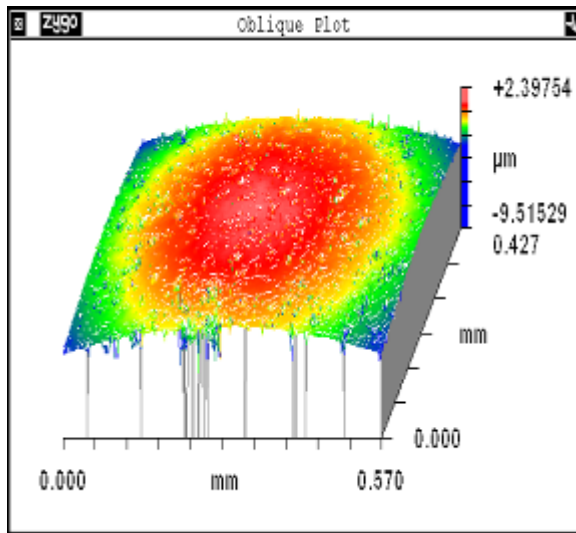


Figure 2-6: Schematic of core drill machining of Silicon Nitride.

Surface Condition	Step	Wheel	Removal
Coarse	1 (roughing)	accepted practice	
	2 (induce damage)	100 grit	0.1000 mm
	3 (finishing)	600 grit	0.0127 mm
Fine	1 (roughing)	accepted practice	
	2 (induce damage)	180 grit	0.1000 mm
	3 (finishing)	600 grit	0.0127 mm
RCF-Conventional	Use the “accepted” practice for RCF finishing (Ref PO# SB 1341-02-N-1669).		

**Table 2-1: Machining procedures used to prepare rolling contact fatigue specimens.**

Four sets of twenty Ceralloy 147-31N SRBSN balls were machined using the core drills. Three sets were finished with coarse, fine, RCF-conventional conditions as defined above. Another set of ball blanks was finished to 13.45 mm diameter with allowance for lapping machine finishing comparisons with HIPed Silicon Nitride. The surface conditions of coarse, fine and RCF-conventional Ceralloy 147-31N SRBSN balls are shown in Figure 2-7 to Figure 2-9. The surface profile was measured on a Zygo optical interferometer, which is shown in Figure 2-10.



**Figure 2-7: Surface profile of coarse finished  $\text{Si}_3\text{N}_4$  ball using core drills.**

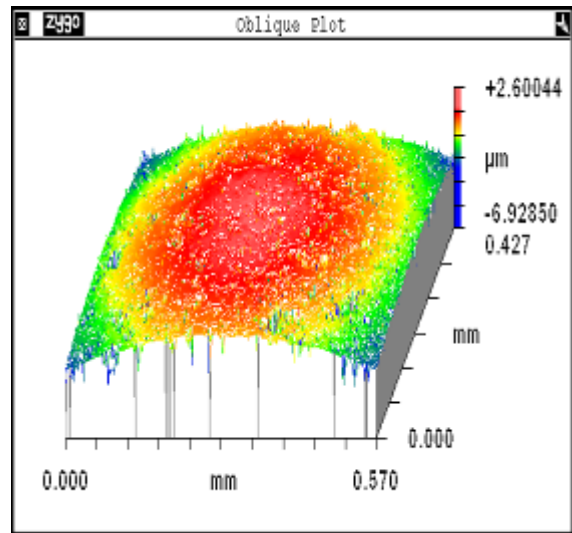


**Figure 2-8: Surface profile of fine finished Silicon Nitride ball using core drills.**

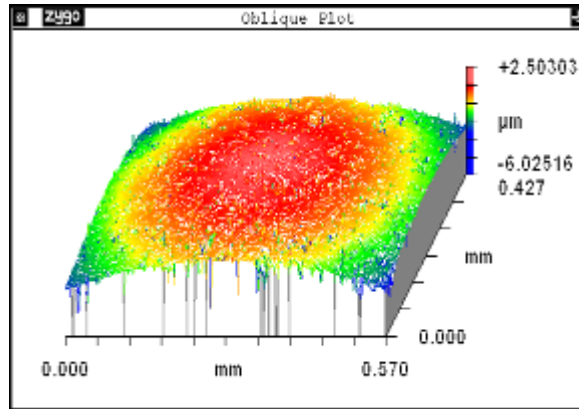


Figure 2-9: Surface profile of RCF-conventional finished Silicon Nitride ball using core drills.

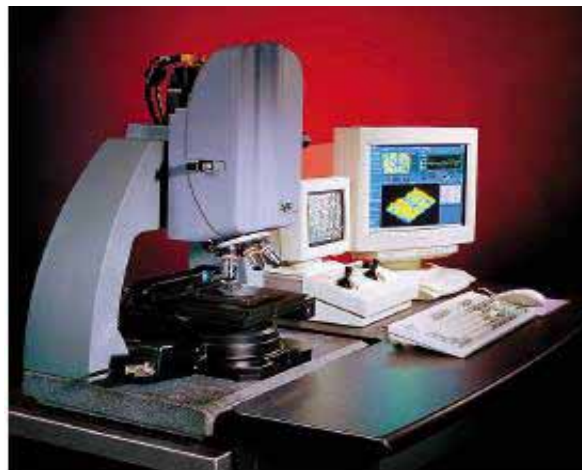


Figure 2-10: Zygo Newview optical interferometer

The comparison of the surface profile is shown in Table 2-2 below. As indicated in the data, the coarse and fine specimens had similar surface roughness as expected because the last step in the machining of these two surface conditions was identical, using a 600 grit diamond grinding wheel. The RCF-conventional specimens had better average surface roughness compared with the other two types of specimens as these specimens were ground by a 1200 grit diamond grinding wheel in the last machining step.

Finishing Condition	Average Ra (nm)	Average Rms (nm)
Coarse	231	327
Fine	219	330
RCF-conventional	160	314

Table 2-2: Surface profile of core drill finished Silicon Nitride balls.

Five Ceralloy 147-31N SRBSN balls from each of the coarse, fine and RCF-conventional surface finishing conditions were further machined to C-Sphere specimens for the evaluation of surface strength of Ceralloy 147-31N SRBSN balls. Fifteen remaining SRBSN ball specimens of each condition were used to study their RCF performance.

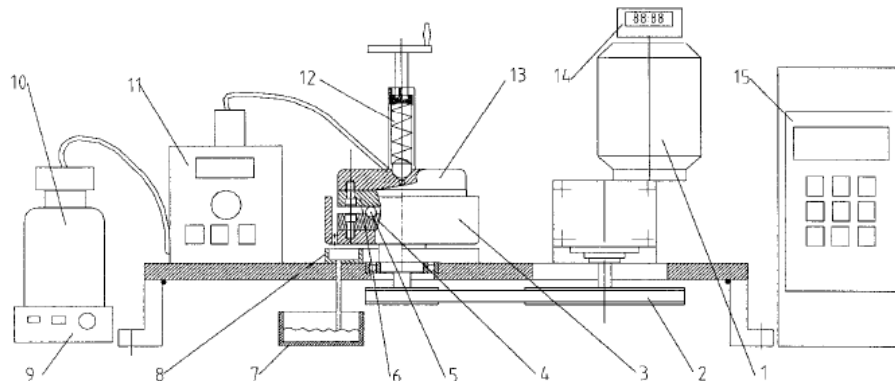
### 2.2.2. Lapping of Silicon Nitride ball

Unlike the above Ceralloy 147-31N Silicon Nitride specimens prepared for the RCF test, which were machined by diamond grinding core drills, most of the commercial grade Silicon Nitride ball bearing elements were finished on industrial lapping machines with two parallel metal lapping plates, with diamond suspension fluid as abrasive.

The conventional way of Silicon Nitride finishing is through grinding and lapping process at a low rotational speed but a high load, with diamond paste as abrasive. This process is time-consuming and expensive, and also prone to produce surface damages. An alternative finishing process is magnetic float polishing (MFP), which is based on the magneto-hydrodynamic behavior of a magnetic fluid. This process removes Silicon Nitride through a micro-mechanical mechanism by generating ductile fractures at nanometer level (Lu, Yuan et al. 2002). The load on Silicon Nitride ball is generally small (0.5N-2N) which is applied through the magnetic abrasives suspended by the magnetic fluid. MFP can achieve a high finishing rate and minimal surface damage as a result of the high rotational speed and low contact load (Komanduri, Hou et al. 1999).

As a result of tooling availability, the traditional lapping finishing of Silicon Nitride ball bearing element was studied on an eccentric lapping machine, which was designed and manufactured in-house to simulate the industrial lapping process (Kang and Hadfield 2001). The effects of load, abrasive, speed and lapping plate have been comprehensively examined on this machine in previous studies (Kang and Hadfield 1999; Kang and Hadfield 2001; Kang and Hadfield 2001). However, the importance of the eccentricity effect was not quantified. In the current research, the eccentricity effect of the lapping plates on the finishing rate was investigated. Two sets of fifteen ball blanks were used to study the eccentricity effect: the Ceralloy 147-31N SRBSN ball blanks and Spheric-

Toshiba HIPed Silicon Nitride ball blanks. Both sets of ball blanks were finished on this lapping machine with a target to achieve grade 5 average surface roughness (C1323 2001), which is the minimum standard for commercial ball bearing elements. Three pairs of lapping plates with 0 mm, 8 mm and 12 mm eccentricity on the lower plates were machined from steel ingot. The schematic and the physical setup of the lapping machine are shown in Figures 2-11 and 2-12 below.



Schematic of the novel eccentric lapping machine: 1, a.c. motor and gearbox combination; 2, pulleys and belt; 3, flange shaft; 4, lower plate; 5, ceramic ball; 6, top plate; 7, lubricant fluid collection tank; 8, lubricant fluid tray; 9, magnetic stirrer; 10, lubricant fluid; 11, pump; 12, spring loading unit; 13, backing plate; 14, time counter; 15, microinverter

**Figure 2-11: Schematic of the lapping machine (Kang and Hadfield 2001)**



**Figure 2-12: The lapping machine setup**

The lapping machine was made up of three units, the abrasive supplying unit, loading control and lapping unit and motion unit as shown in the schematic in Figure 2-13. The

abrasive supplying unit was controlled by a micropump which sucked abrasive fluids from a glass container placed on a magnetic stirrer which maintained a uniform mixing of the abrasive fluid. The abrasive fluid feeding speed was fixed at 15 strokes per minute throughout the lapping experiment for consistency.

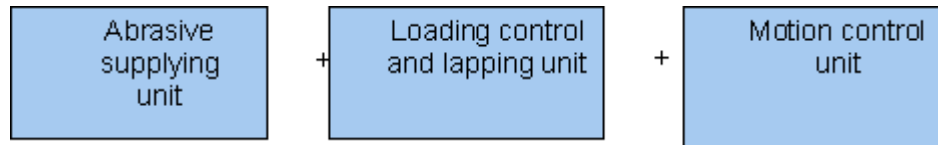


**Figure 2-13: Three units of lapping machine**

The mechanical loading was applied through a coil spring onto the backing plate. The lapping plates were parallel surfaces with a groove on the lower plate as shown in Figure 2-14. The upper plate, as shown in Figure 2-15 stayed static during the lapping process. The lower plate was driven by a friction belt connected to an electric motor. The speed of the motor can be varied, but for the purpose of this study, the motor speed was fixed at 169 rpm for the lapping step and 93.75 for the polishing step.

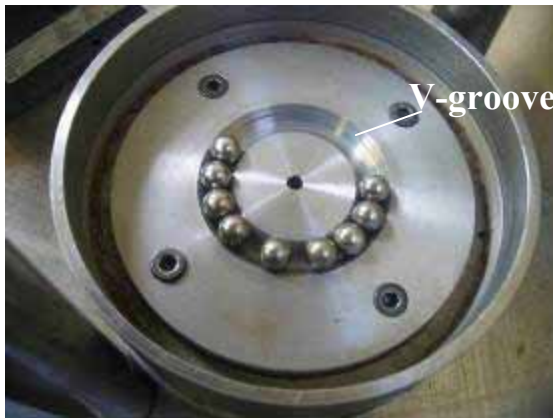


**Figure 2-14: Lower plate**



**Figure 2-15: Upper plate**

The Silicon Nitride ball finishing process using the lapping machine can be divided into two steps – lapping and polishing. In the lapping process, the applied load is higher to achieve faster material removal, and the diamond suspension abrasive fluid has a higher concentration of larger abrasive particles. In the polishing process, the load is reduced, and the diamond suspension abrasive fluid has a lower concentration of finer abrasive

particles to remove the final layer of Silicon Nitride to achieve a grade five surface quality. The setup and conditions of the lapping machine is summarised in Table 2-3 below.

Steps	Load	Speed	Particle Size	Lapping Fluid Concentration	Lapping Plates
Lapping	43 N per ball	169rpm	45 micron and 9 micron diamond paste	1:30	0 mm, 8 mm, and 12 mm eccentricity
Polishing	8.82 N per ball	93.75rpm	1 micron and 1/4 micron diamond paste	1:60	0 mm eccentricity only

**Table 2-3: Material finishing parameters in the lapping and polishing steps.**

The load and speed parameters were chosen with reference to previous studies (Kang and Hadfield 2001) in order to achieve a good finishing rate without introducing significant subsurface damage. The lapping plates with 0mm, 8mm and 12mm eccentricity were used at each particle size to study the eccentricity effect on the finishing rate. The ball kinematics was studied by Kang (Kang and Hadfield 2001) and Figure 2-16 shows the variations in ball spin angular speed  $\omega_b$ , ball spin angle  $\beta$  and ball circulation angular speed  $\omega_c$  at different contact points on the V-groove (designated as rotation angle of the lower plate  $\Omega_p t$ ) during a 360° rotation of the lower plate.

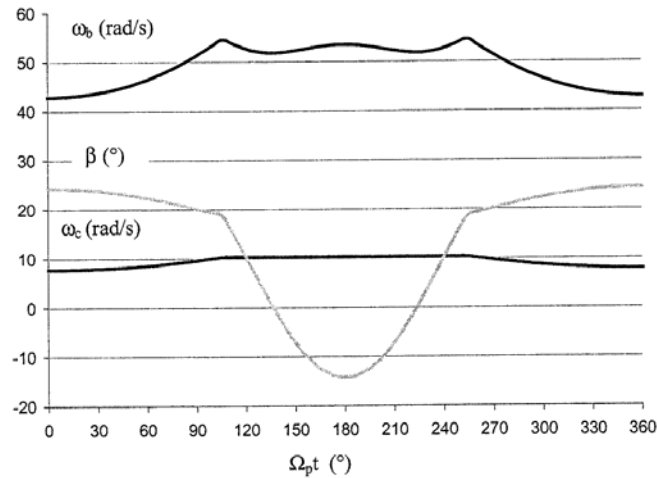


**Figure 2-16: Variation of  $\omega_b$ ,  $\beta$ ,  $\omega_c$  during a 360° of the lower plate under a typical lapping condition with the V-groove having 8mm eccentricity (Kang and Hadfield 2001).**  
The effect of V-groove eccentricity on the ball kinematics is shown in Figure 2-17.

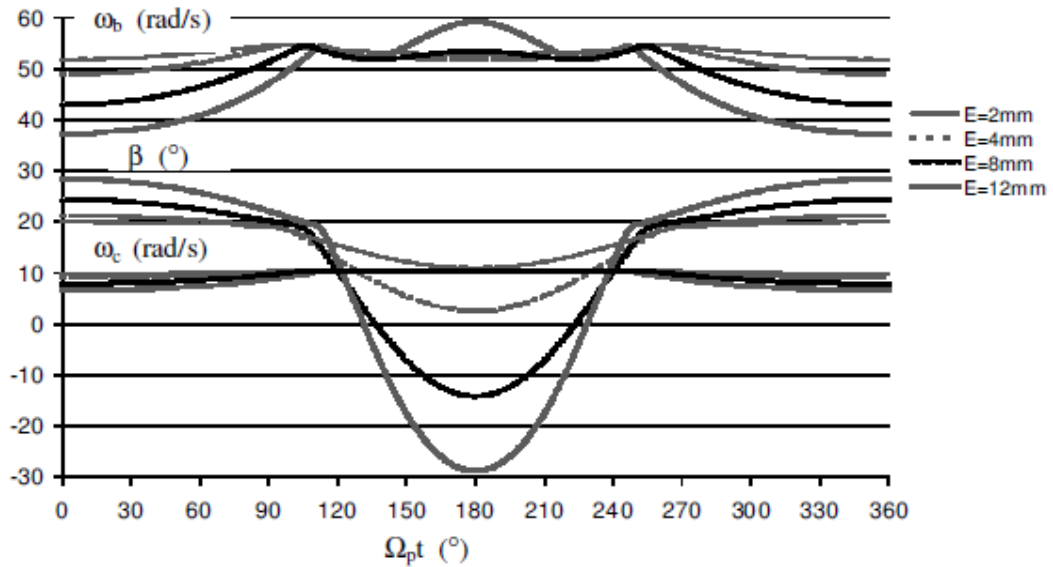


**Figure 2-17: Influence of eccentricity on ball kinematics under the same lapping condition(Kang and Hadfield 2001)**

Two batches of fifteen ball blanks were studied, the HIPed Silicon Nitride (Spheric-Toshiba) ball blanks and SRBSN ball blanks. The average Spheric-Toshiba ball blank diameter was 13.35 mm prior to the start the lapping process and the average SRBSN ball blank diameter is 13.45 mm prior to the start. The lapping step reduced the diameter of the ball blanks to 12.85 mm before the start of the polishing step. The ball blank diameters reduced to approximately 13.00 mm using diamond suspension abrasive fluid containing 45 micron diamond paste. Diamond suspension abrasive fluid containing 9 micron diamond paste was then applied to reduce the ball blank diameters to approximately 12.85 mm. The diameter of the ball blanks was measured using a digital calliper at scheduled intervals.

The material removal rate of Spheric-Toshiba ball blanks are summarised in Table 2-4. The surface profile of selected ball blanks was inspected on the Zygo Interferometer to monitor the surface roughness after completing the lapping step using 45 micron diamond suspension fluid.

<b>Plate eccentricity (mm)</b>	0	8	12	0	8	12
--------------------------------	---	---	----	---	---	----

Diamond paste size	45 micron			9 micron		
Avg Initial Ball Diameter (mm)	13.35	13.26	13.15	13.01	12.95	12.88
Avg Interim Ball Diameter (mm)	13.26	13.15	13.01	12.95	12.88	12.84
Number of Hours	1.70	2.04	2.89	1.25	1.42	0.76
Finishing Rate (micron/hour)	52.9	53.8	48.3	48.0	49.3	52.6

Table 2-4: Finishing rates of Spheric-Toshiba Silicon Nitride ball blanks

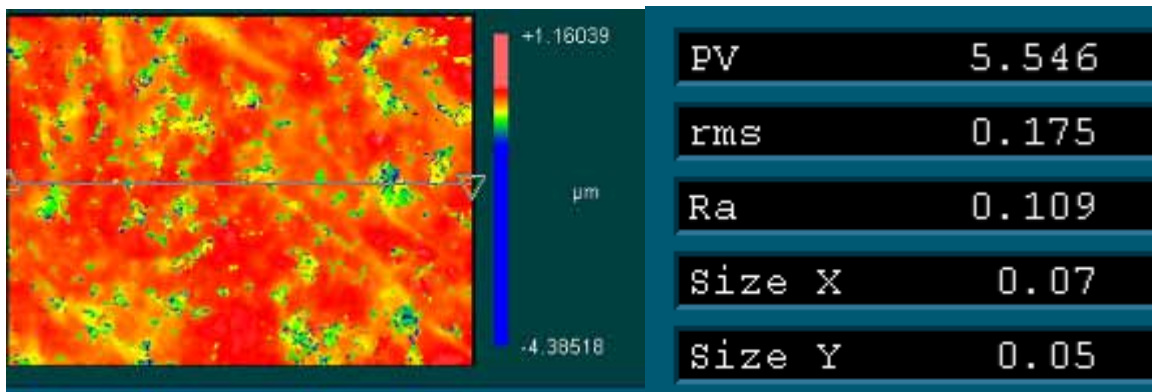
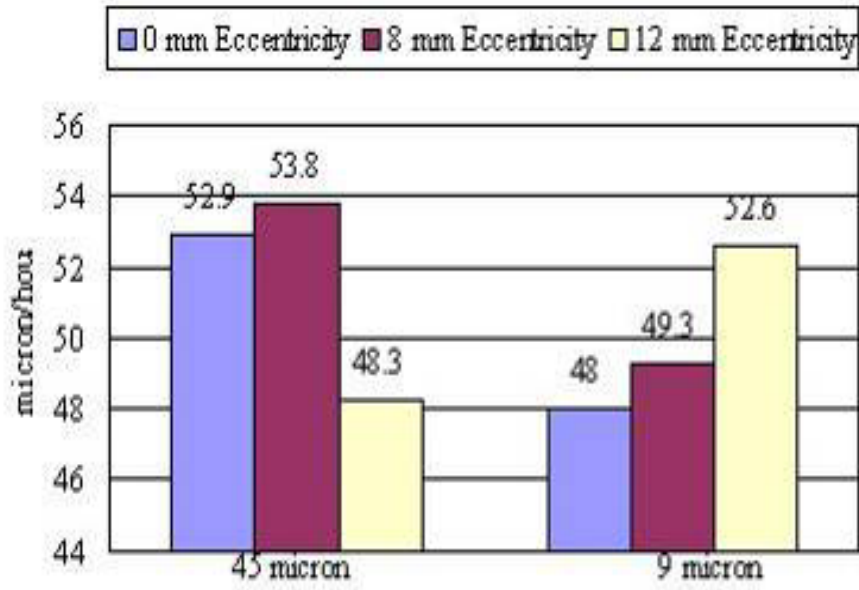


Figure 2-18: Typical surface profile of Spheric-Toshiba after 45 micron diamond paste lapping

As shown in Figure 2-18, the selected ball blank achieved an average roughness of 109 nm after 6.63 hours 45 micron diamond suspension abrasive fluid lapping. There was no significant trend of improved material removal rate with increased eccentricity, and it was observed that the material removal rate of 12 mm eccentricity lapping plate was reduced by 10% compared with the 8 mm eccentricity lapping plate. The overall material removal rate with 45 micron diamond suspension abrasive fluid was 51.3 microns per hour, and the overall material removal rate with 9 micron diamond suspension was 49.6 microns per hour. As seen from this data, the diamond size had slight but limited effect on the material removal rate at the lapping step, which is in line with the results from previous studies. However quantification of the effect of diamond particle size on the material removal rate is inconclusive from this study.



**Figure 2-19: Finishing rates of Spheric-Toshiba ball blanks**

There was a slight increase in material removal rate with increased eccentricity using 9 micron diamond suspension fluid as shown in Figure 2-19. However, the increase was minimal which could be a result of the variation of loading, diamond concentration and digital calliper measurements. Comparing trends seen on 45 micron diamond suspension abrasive fluid lapping, it is concluded that the eccentricity did not have any effect on the material removal rate of Spheric-Toshiba HIPed Silicon Nitride ball blanks.

The material removal rates of SRBSN ball blanks are summarised in Table 2-5, and the surface profile of selected ball blanks was inspected on the Zygo Interferometer to monitor the surface roughness after completing the lapping step using 45 micron diamond suspension fluid. As shown in Figure 2-20, the selected SRBSN ball blank achieved a roughness of 144 nm after 6.48 hours 45 micron diamond suspension fluid lapping. The average roughness of the SRBSN ball blank was higher than the Spheric-Toshiba ball blank, which could be a result of the difference in material property, such as density and hardness. However, the reason for the average roughness variation is not understood, and it is not the main aim for this study.

<b>Plate eccentricity (mm)</b>	0	8	12	0	8	12
<b>Diamond paste size</b>	45 micron			9 micron		
<b>Avg Initial Ball Diameter (mm)</b>	13.45	13.25	13.14	12.99	12.95	12.90
<b>Avg Interim Ball Diameter (mm)</b>	13.25	13.14	12.99	12.95	12.90	12.85
<b>Number of Hours</b>	2.82	1.58	2.08	0.59	0.71	0.73
<b>Finishing Rate (micron/hour)</b>	70.9	69.8	72.1	67.8	70.4	68.5

**Table 2-5: Finishing rate (materials removal rate) of SRBSN ball blanks**

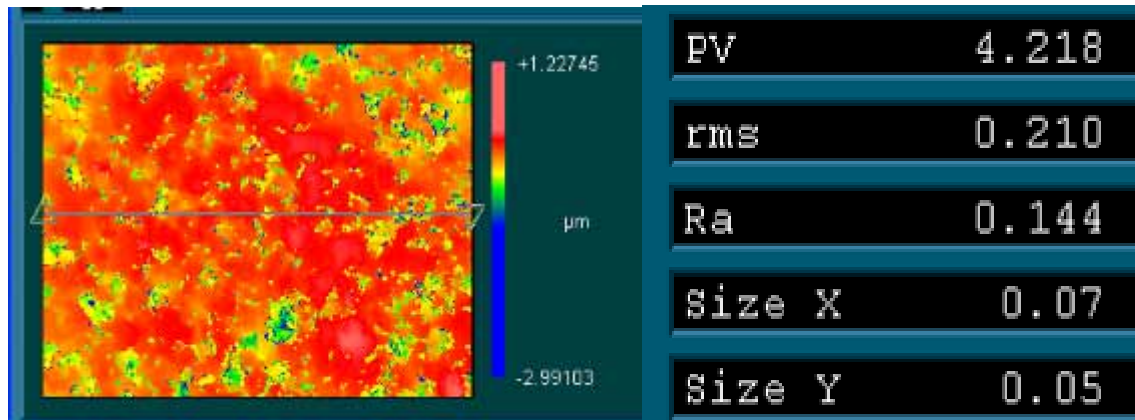


**Figure 2-20: 45 micron diamond paste finished SRBSN ball blank surface profile**

As shown in Figure 2-21, the eccentricity of the lapping plate did not increase the material removal rate of SRBSN ball blanks, as was observed in the finishing Spheric-Toshiba ball blanks. The overall material removal rate with 45 micron diamond suspension fluid was 71.0 microns per hour, and 68.9 microns per hour with 9 micron diamond suspension fluid. Compared with the material removal rate of Spheric-Toshiba ball blanks, SRBSN removal rate was 38% higher with 45 micron diamond suspension and 39% higher with 9 micron diamond suspension at the lapping step of the finishing process.

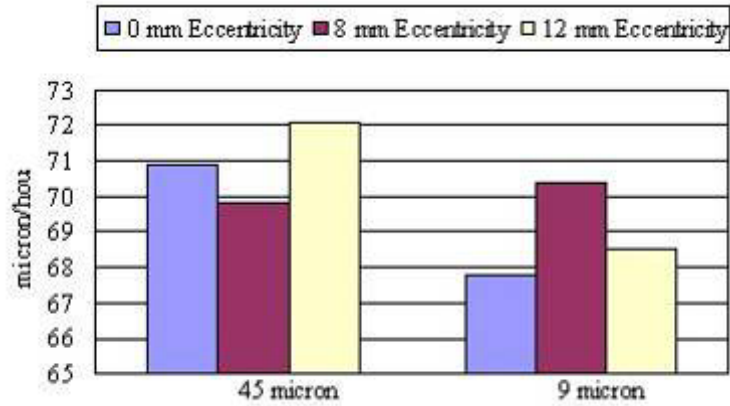


Figure 2-21: SRBSN ball blank finishing rate

After completing the lapping step, both batches of Spheric-Toshiba and SRBSN ball blanks were polished to achieve an above grade 5 finish for RCF testing. 1 micron and 1/4 micron diamond suspension fluid were used to achieve the required surface finishing condition. As concluded in the lapping step, as the eccentricity did not have an impact on the material removal rate, only the concentric lapping plates (0 mm eccentricity) were used in the polishing step to simplify the study. The material removal rates of the ball balls are summarised in Table 2-6.

Specimen	Diamond Paste Size	Avg Initial Ball Diameter (mm)	Avg Interim Ball Diameter (mm)	Duration (hours)	Finishing Rate (micron/hour)
Spheric-Toshiba	1 micron	12.84	12.75	36.5	2.47
Spheric-Toshiba	1/4 micron	12.75	12.70	22.2	2.25
SRBSN	1 micron	12.85	12.75	28.6	3.50
SRBSN	1/4 micron	12.75	12.70	17.9	2.80

Table 2-6: Material removal rates at the polishing step

Selected ball blanks from Spheric-Toshiba and SRBSN were examined under the Zygo interferometer to see the surface profile of the specimen after completion of the polishing process with a ball diameter of 12.70 mm. The surface profiles (with spikes removed) are shown in Figures 2-202 and 2-23. As shown in the figures, the Spheric-Toshiba ball achieved an average roughness of 2 nm, and the SRBSN ball achieved an average

roughness of 3 nm, both of which satisfies grade three average roughness requirement, and is significantly better than the grade five target average surface roughness.

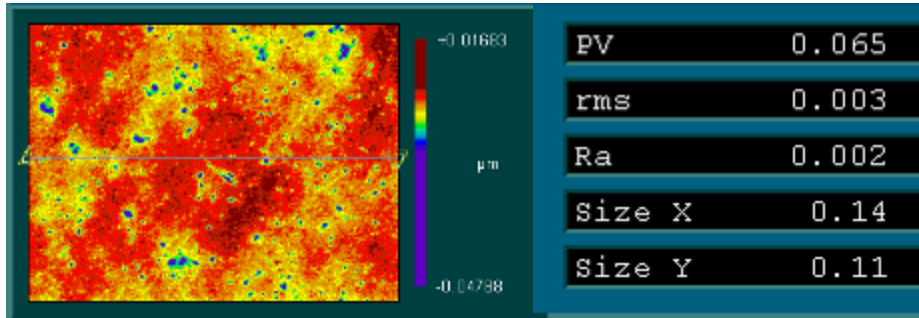


Figure 2-22: Spheric-Toshiba ball blanks after 1/4 micron diamond paste lapping at 12.70 mm diameter

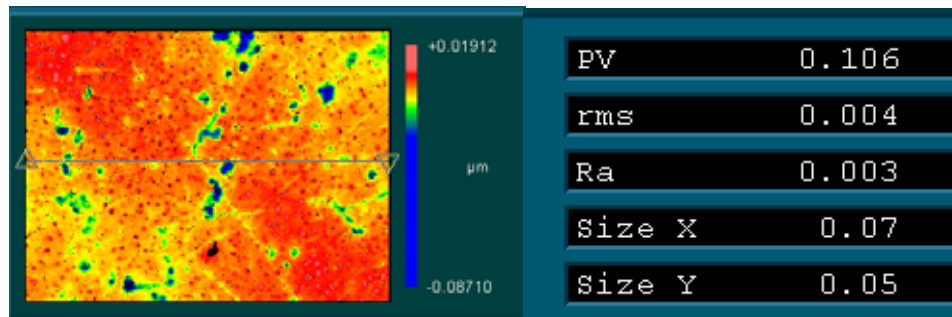


Figure 2-23: SRBSN ball blanks after 1/4 micron diamond paste lapping at 12.70 mm diameter

As shown in Figure 2-24 below, the SRBSN ball blanks had a better overall material removal rate in the polishing step which was in line with the observation in the lapping step. With 1 micron diamond paste, SRBSN material removal rate was 42% better than Spheric-Toshiba, and with 1/4 micron diamond paste, SRBSN material removal rate was 24% better.

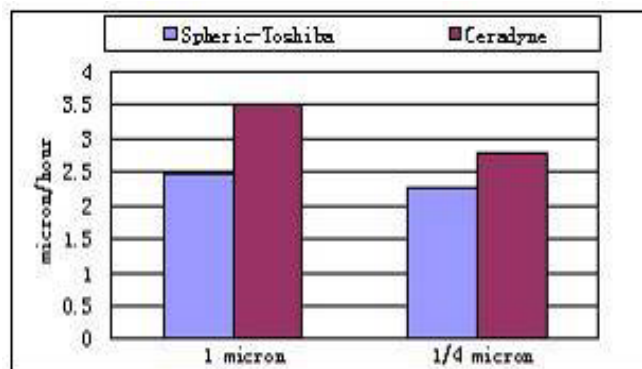


Figure 2-24: Material removal rate comparison

### 2.2.3. Machining of RCF Rod Specimens

In order to evaluate the rolling contact performance of Silicon Nitride using a ball-on-rod tester and also evaluate the flexure strength of half-rod specimen, the SRBSN RCF rod specimens were prepared using the centreless grinding technique. As stated in section 2.2.1, the rods were ground to three surface conditions detailed in Table 2-1, which was identical to the surface conditions of core-drill finished SRBSN balls in order to make surface strength and RCF performance comparisons. One factor of particular note is that there are two types of grinding direction, the longitudinal grinding and transverse grinding, which generate different surface textures, as shown in Figures 2-25 and 2-26. The grinding of the rod specimens was carried out by a machining subcontractor in the United States, as the quality of the machining is crucial to the subsequent tests. However the machining specification (including tolerances) and instruction was defined and provided to the contractor.



**Figure 2-25: Longitudinally-ground surface**

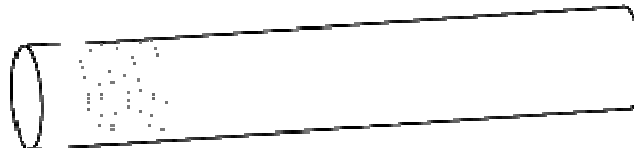


**Figure 2-26: Transversely-ground surface**

As the surface texture does have an effect on the surface strength of the rod specimen (Quinn, Ives et al. 2003), only transverse grinding was used to prepare the SRBSN RCF rod specimens. Similar to the SRBSN ball specimens, 20 rods in each of coarse, fine and RCF-conventional finishing conditions were machined for this study. Eight of the RCF rod specimens of each condition were further machined to half-rod specimens to evaluate the surface strength, and fifteen specimens in each finishing condition were reserved for RCF studies on the ball-on-rod tribotester.

#### 2.2.4. Machining of C-Sphere Specimens

In order to evaluate the surface strength of Silicon Nitride balls, the C-Sphere specimens were machined from the half inch diameter Silicon Nitride balls. The dimension of the specimen is shown in Figure 2-27. A quarter inch slot was required to be machined into the Silicon Nitride balls using a diamond grinding wheel with the defined dimension. The outer ball surface needed to be protected as the surface strength of the C-Sphere is very sensitive to surface defects introduced in the machining process, such as dents and scratches. The grinding of the C-Sphere specimens was carried out by a machining subcontractor in the United States, as the quality of the machining is crucial to the subsequent tests. However the machining specification (including tolerances) and instruction was defined and provided to the contractor.

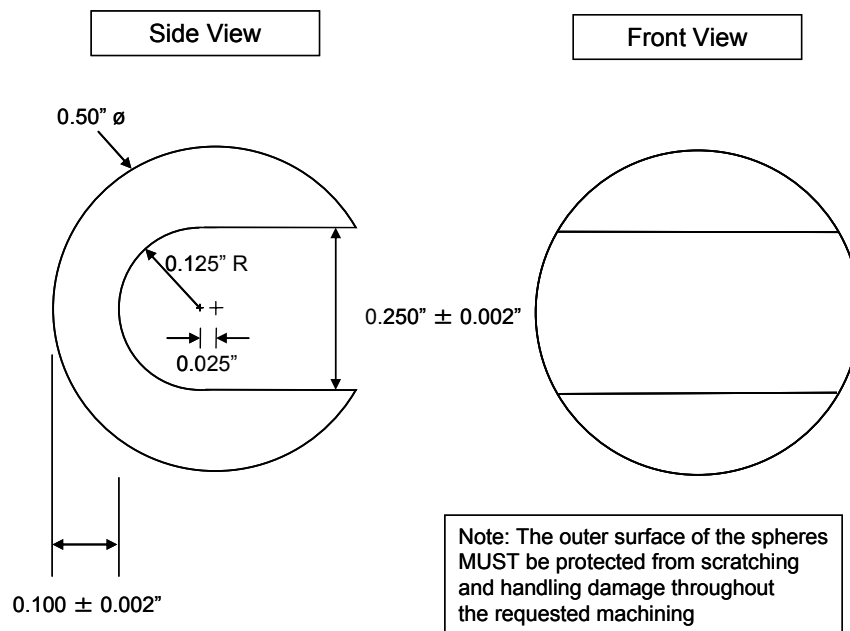


Figure 2-27: C-Sphere specimen geometry

Five specimens from each batch of coarse, fine and RCF-conventionally machined SRBSN balls were machined to C-Sphere specimen. Fourteen SN101C and Toshiba HIPed Silicon Nitride balls were also machined into C-Sphere to evaluate the surface strength of these ball bearing elements. The physical samples of the specimens are shown in Figures 2-28 and 2-29 below.



**Figure 2-28: C-Sphere specimens**



**Figure 2-29: C-Sphere specimens**

# CHAPTER 3: SURFACE STRENGTH OF SILICON NITRIDE

## 3.1 RCF Half Cylinder Flexure Strength

In order to quantify the influence of subsurface damage of the RCF test rod on the RCF performance of Silicon Nitride, the half RCF cylinder flexure strength was examined. The size of the flaws which initiated the failure of the test rod can be predicted and compared among three groups of specimens which have coarse, fine and RCF-Conventional surface finishing conditions respectively. The geometry of the half RCF cylinder specimen is shown in Figure 3-1. The surface finish standard was determined from the RCF test rod finishing standard.

Three batches of specimens with coarse, fine and RCF-Conventionally finished subsurfaces were tested. In each batch, there were eight specimens in total. Statistically eight specimens do not provide any conclusive results through Weibull Analysis, but the test did show a trend of increased effective strength from coarse, fine to RCF-Conventional finishing conditions.

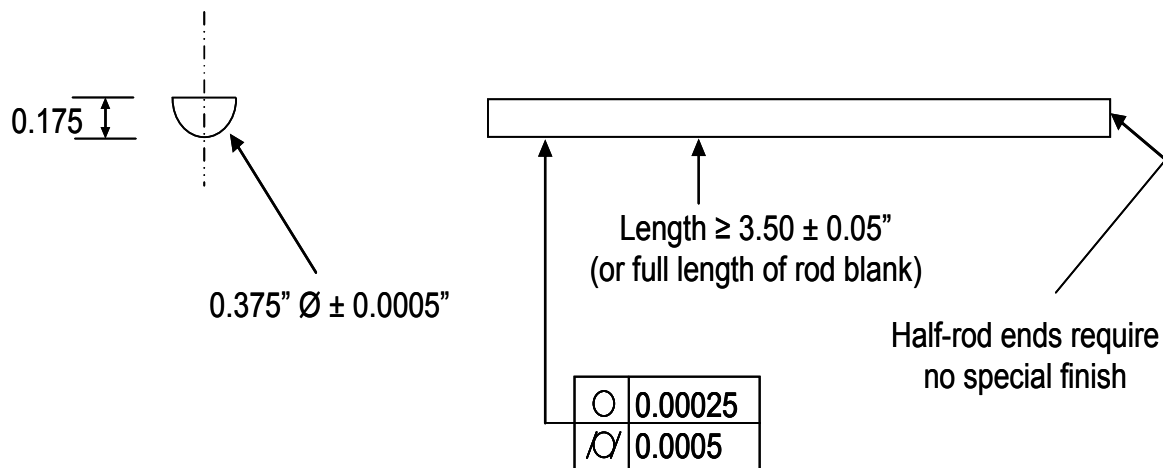
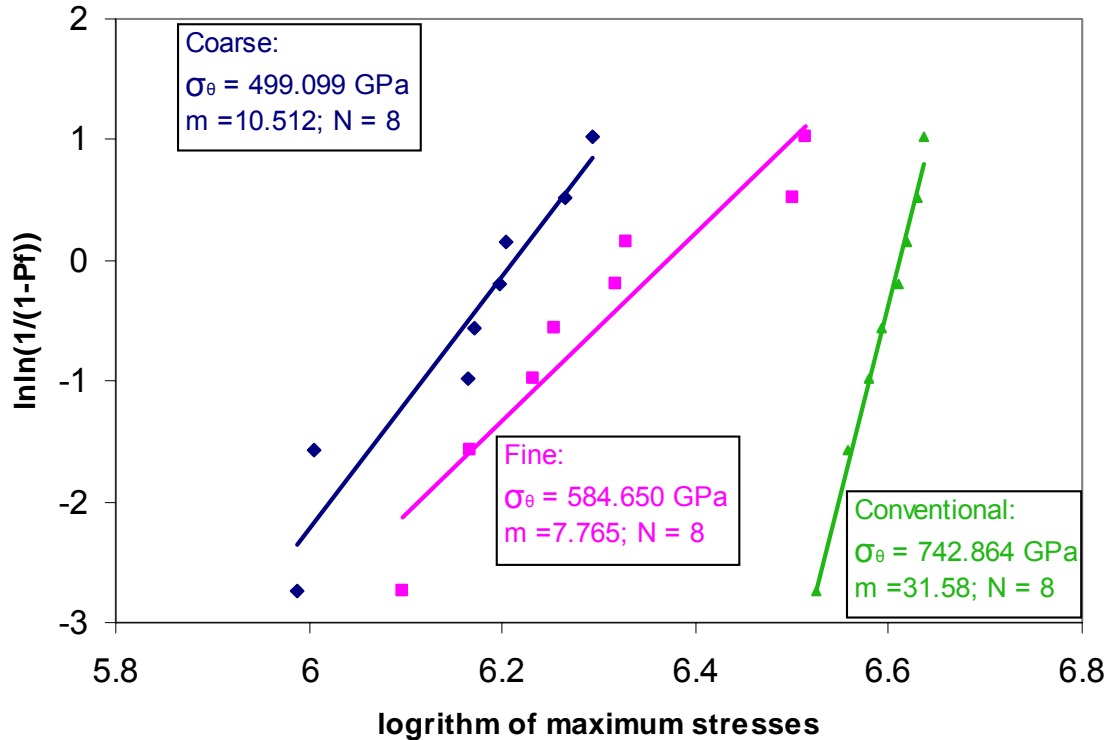


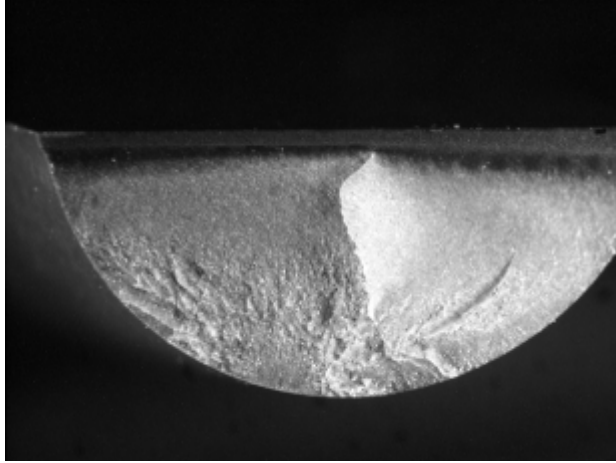
Figure 3-1: RCF half cylinder flexural strength specimen dimensions and tolerances



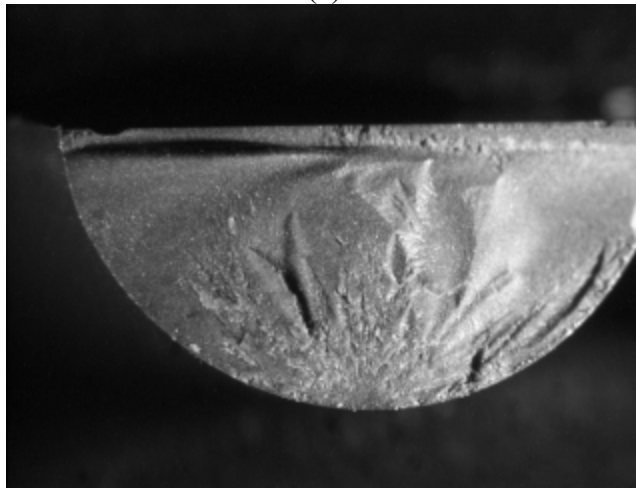
**Figure 3-2: Half RCF cylinder flexure strength of coarse, fine and RCF-Conventionally machined SRBSN specimens**

Weibull analysis of the test results is shown in Figure 3-2. The RCF-Conventionally machined specimen had a superior effective strength compared with coarse and fine machined specimens, where it was ~30% better than fine finished specimens and ~50% better than coarse finished specimens. With a fracture toughness of 6 MPa√m, and a crack geometry factor 1.5, according to Griffith law, the flaw sizes of coarse, fine and RCF-conventionally finished half RCF cylinder were 64, 47 and 29 microns respectively.

The optical fractography of the weakest specimens in each batch of coarse, fine and RCF-conventionally finished specimens is shown in Figure 3-3, with the remaining optical fractography of half RCF cylinder shown in Appendix 7.2. The trend displayed in half RCF cylinder flexure strength offers a positive result that coarse, fine and RCF-conventionally finished SRBSN balls have various qualities of subsurface (flaw size), which can be verified by C-Sphere flexure strength tests. This variation can then be linked to RCF test results, which can provide an important reference to the machining-fatigue life relationship.



(a)



(b)



(c)

**Figure 3-3: Optical fractography of the weakest coarse, fine and RCF-Conventionally finished specimens, from top to bottom respectively.**

## 3.2 C-Sphere Test

A test coupon called the “C-Sphere” flexure strength specimen was developed to enable the study and measurement of a strength and linked flaw size. Enabling the identification of flaw type (usually surface- or near-surface located) and measurement of its size in finished ceramic balls is important for the study of strength, but more importantly, for the study and predictability of RCF performance (a response limited by surface- or near-surface-located flaws or in changes thereof). It has been reported that a critical depth of ring cracking in RCF is 5-20 microns below the surface; the C-Sphere specimen is ideal for studying near-surface depths.

### 3.2.1. C-Sphere Geometry

The C-Sphere specimen was produced through the controlled slotting of a ceramic sphere. It was then diametrically loaded (or flexed) to initiate fracture at the sphere’s surface or “outer fibre”. The C-Sphere is analogous to a “C-ring” flexure specimen that is produced through the slotting of a ceramic ring. A description of the C-Sphere flexure strength specimen follows and a comparison of the C-Sphere flexure strength distributions of coarse, fine and RCF-Conventionally machined Ceralloy 147-31N SRBSN and two other commercially available Silicon Nitride bearing grade materials is presented.

To work towards an optimized C-Sphere geometry, a finite element analysis (FEA) model was created in ANSYS. The testing of the common ball diameter of 12.7 mm (0.50 in.) was the focus. Candidate slot widths of 3.175 mm (0.125 in.) and 6.35 mm (0.25 in.) were considered because they are common sizes for grinding wheel thicknesses, and the C-Sphere machining would therefore be likely to be economical and have associated quick turn-around time. Slot depth was varied until a slot-width-slot-depth combination produced at least a 10-times higher outer fibre surface tensile (hoop) stress than any other surface tensile stress located elsewhere on the coupon. The geometry of the final C-Sphere is shown in Figure 3-4. An offset between the original ball’s centre-line and the centre-line of the 3.175 mm radius was deemed necessary because if the offset was zero or too small, then significant tensile stresses would be created on the C-Sphere’s interior

with the high likelihood that fracture would be initiated there because of both the high tensile stress and relatively rough surface finish produced by the grinding wheel.

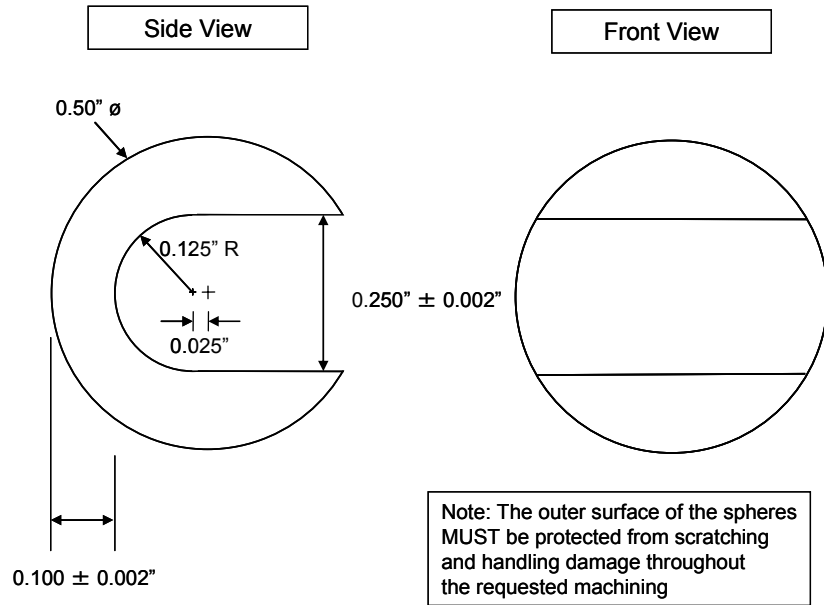


Figure 3-4: C-Sphere geometry

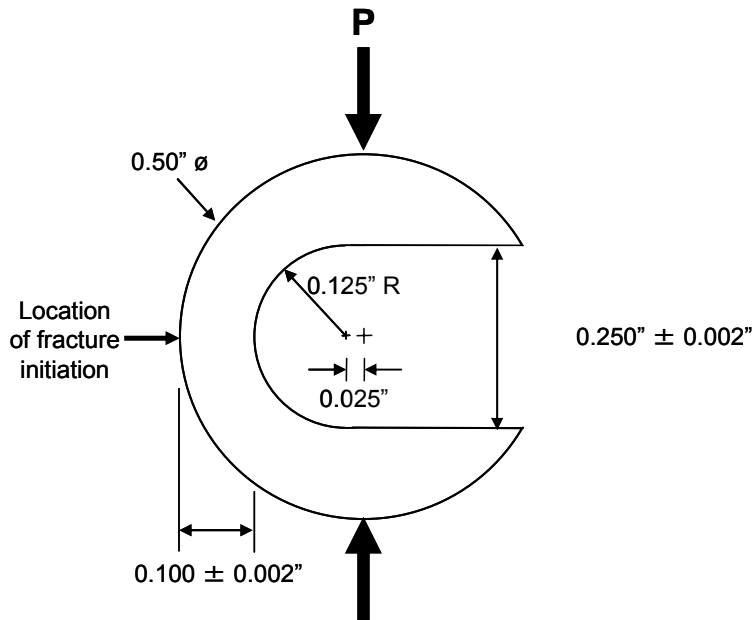
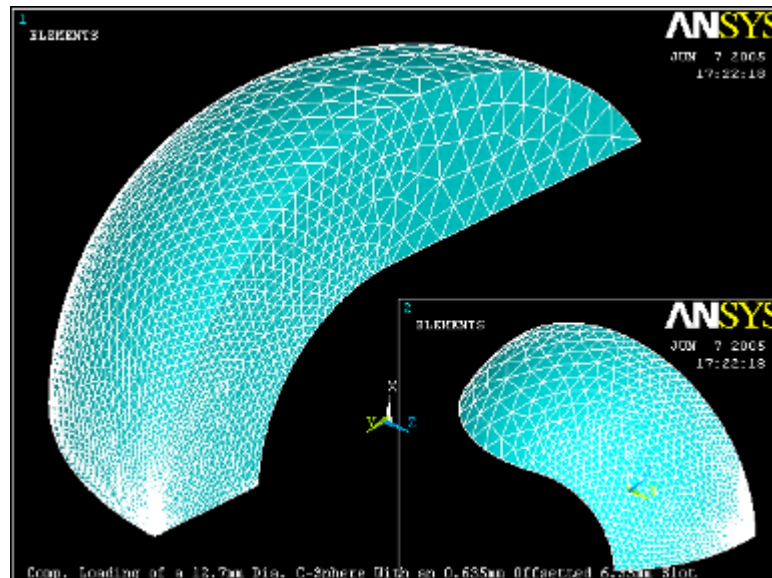


Figure 3-5: C-Sphere flexure strength loading schematic.

The final offset size (0.635 mm) resulted in a C-Sphere geometry that, when diametrically compressed, produced an outer-fibre tensile stress much larger than that on the ground interior and therefore a high likelihood that fracture would (desirably) occur there. The point load was applied at the apex of the C-Sphere specimen, as shown in Figure 3-5.

### 3.2.2. C-Sphere FEA Characteristics

Figure 3-6 shows a quarter-symmetry model for the C-Sphere specimen and the mesh distribution that was ultimately used to evaluate its effective volume and area. Solid95 tetrahedral elements were used, and a 100 N point load was applied to the sphere's apex. As can be seen from the figure, fine mesh density was used in the region where high tensile stresses would develop, gradually getting coarser towards the area where the load was applied and the overhang section.



**Figure 3-6: Mesh distribution for  $\frac{1}{4}$  symmetry model of the C-Sphere specimen.**

The issue of artificially high stress concentration within the narrow zone under the applied point load and its effect on the computed effective sizes was considered. In the virtual world of FEA, the load was applied as a perfectly concentrated point load which caused stress singularity in that region. This is an idealisation of what physically takes place where a distributed load acting over a narrow area is actually applied. In other

words, as the mesh gets finer the stress under the load will increase indefinitely making the model and hence the effective sizes mesh dependent.

To understand the issue of stress singularity under the point load, both nodal and element first principal stress distributions are shown in Figures 3-7 and 3-8 for the intermediate and fine mesh models, respectively. A nodal plot smoothes the stress distribution by averaging the stresses at that point in all the elements having that node in common. This smoothing is masking the very high stresses taking place within the individual elements, which if not removed would yield erroneous effective size calculations. This is because when the effective size is computed, the stress distribution is normalised with respect to the maximum effective stress in the component. If this maximum effective stress is incorrect, due for example to a localised stress concentration as is the case for this model, then the computed value would be incorrect. In order to unmask the high nodal stresses, element stress plots are used which display the actual nodal stresses as computed for each element.

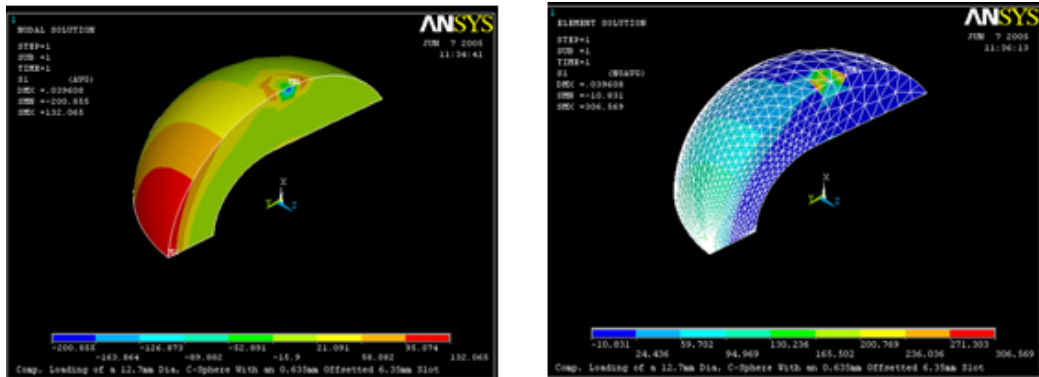


Figure 3-7: Intermediate mesh

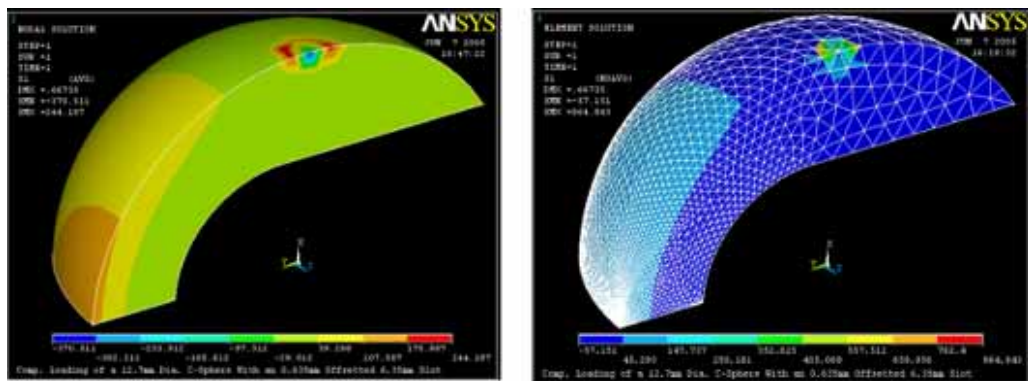
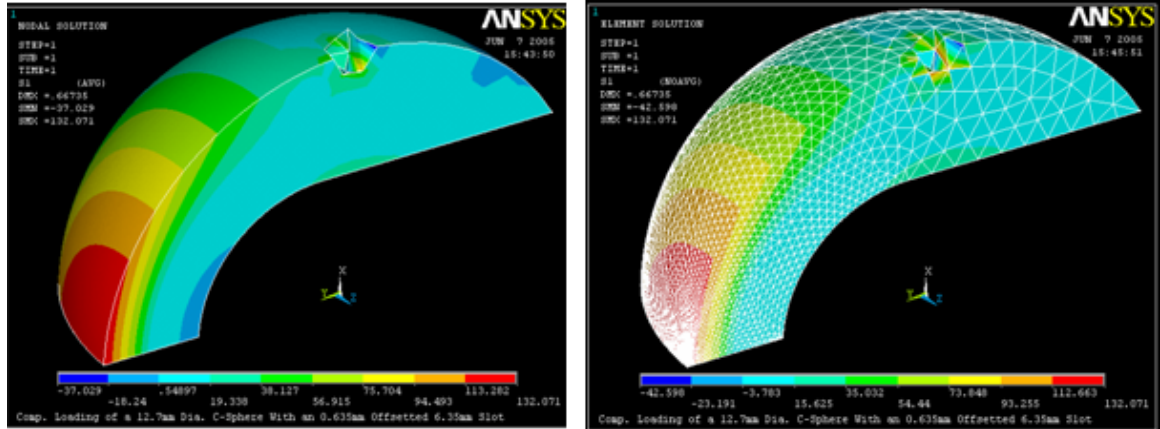


Figure 3-8: Fine mesh

Figure 3-7 shows the nodal and element first principal stress distributions for the C-Sphere specimen using the intermediate mesh model. As can be seen from the nodal plot the maximum tensile stress is computed to be 132.1 MPa taking place at the side of the sphere as expected. However, when the element stress plot is examined, the high tensile stress (306 MPa) region shifts to the area under the load which is obviously an artefact of the point load effect. For the fine mesh model (Figure 3-8), both nodal and element stress plots show the highest tensile stress region to be under the point load, with the maximum first principal nodal and element stresses increasing to 244 MPa, and 644 MPa, respectively. Figures 3-7 and 3-8 clearly show that the stresses under the load are extremely mesh-dependent and will keep changing as the mesh changes, while for the rest of the specimen the stresses have long converged even for the coarse mesh specimen model.

In order to take out the effect of localised stress concentration on the effective size calculations, the artificially high stressed elements under the load were removed. The remaining elements, comprising the vast majority of the specimens, were then used to assess the specimen's effective sizes. Figure 3-9 shows the nodal and element stress distribution plots for the C-Sphere model, with the highly-stressed elements carved out. One could then observe from these plots how the maximum tensile stress of 132 MPa shifts back to the side of the specimen where it should be. The fact that both the nodal and element stress plots yield the same stress distribution indicates that the suspect elements were successfully removed and that the remaining model can now be used to compute the effective sizes. Hence, it is the model of Figure 3-9 that was utilised to compute the effective area and effective volume for the C-Sphere specimen.



**Figure 3-9: a) nodal first principal stress distribution, and b) element first principal stress distribution for the C-Sphere specimen, using the fine mesh model with the elements within the high stress concentration zone (under the load) carved out.**

Figures 3-10 and 3-11 show the effective area and effective volume as a function of Weibull modulus for the C-Sphere specimen, respectively. The effective sizes were computed using the following equations:

$$A_e = \left( \frac{\sigma_0}{\sigma_e} \right)^m \ln \left( \frac{1}{1 - P_f} \right) \quad \text{Eq. 3-1}$$

$$V_e = \left( \frac{\sigma_0}{\sigma_e} \right)^m \ln \left( \frac{1}{1 - P_f} \right) \quad \text{Eq. 3-2}$$

Where  $A_e$  is the effective area,  $V_e$  is the effective volume,  $\sigma_0$  is the scale parameter,  $m$  is the Weibull modulus,  $\sigma_e$  is the maximum effective stress (computed by CARES/Life), and  $P_f$  is the probability of failure (computed by CARES/Life). The effective sizes are independent of the scale parameter since they only vary with geometry, loading, and the Weibull modulus. Hence, the scale parameter was assigned a random value in order to carry out the reliability and effective size calculations. Weibull effective volume/area is used to scale Silicon Nitride strengths from one component size to another, or from one loading configuration to another. Larger specimens or components are likely to be weaker, because of the greater chance of them having a larger, more-severe flaw. Therefore, the effective volume/area in the C-sphere means the volume/area for comparison with other component size/geometry at certain Weibull modulus.

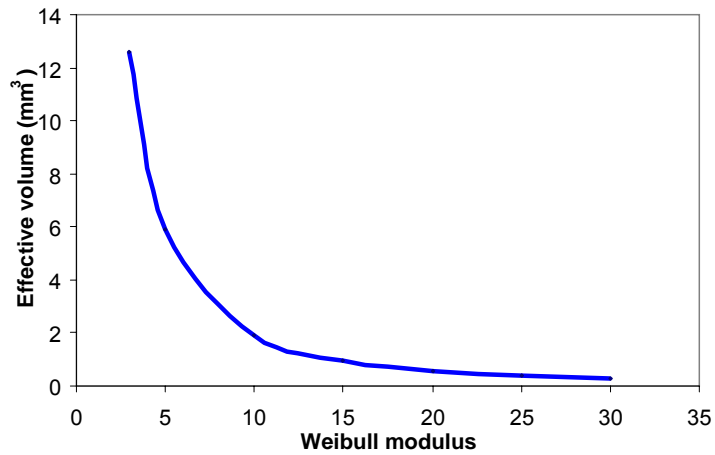


**Figure 3-10: Effective volume in relation to Weibull modulus.**

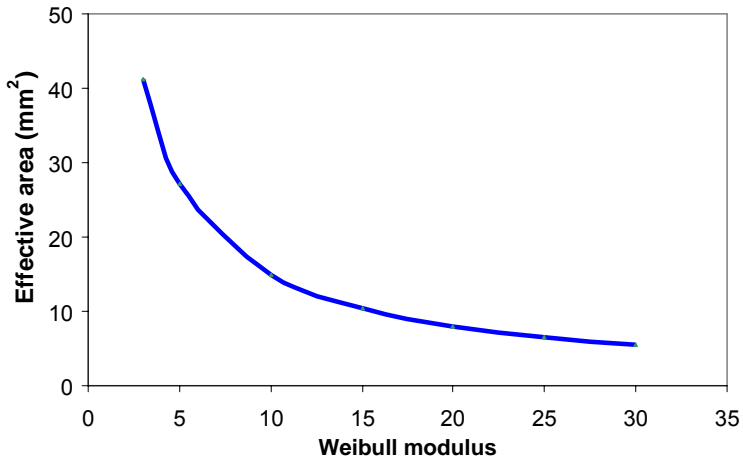


**Figure 3-11: Effective area in relation to Weibull modulus.**

### 3.3.3. C-Sphere Flexure Test

Three grades of Ceralloy 147-31N balls, NBD200 and SN101C balls with 12.7 mm diameter were machined into C-Sphere flexure strength specimens, which is shown in Figure 3-12. Grinding of the slot was performed in a two-step process using a Type 1F1 diamond plated grinding wheel (5 in. dia. x 0.25 in. thick with a full 0.125 in. radius or 127 mm dia. x 6.35 mm thick x 3.175 mm R) for the final grinding. C-Sphere flexure specimens were monotonically and compressively loaded to failure (as shown in Figure 3-13) using an electromechanical universal testing machine at a crosshead displacement rate of 0.5 mm/min. The loading rate was based on the previous successful C-ring test configuration and experience. The 0.5mm/minute loading rate was considered to be able

to capture the onset of failure under compressive loading. A special jig as shown in Figure 3-14 was used to horizontally align the C-Sphere slot prior to loading. Load to fracture was recorded and used to determine C-Sphere flexure strength. Weibull strength distributions were determined using commercially available software. Optical fractography on the post test specimens, as shown in Figure 3-15 was conducted on all specimens to identify failure location. The fracture surfaces of a select few specimens were examined with scanning electron microscopy.



**Figure 3-12: C-Sphere specimens as received from contract manufacturer**

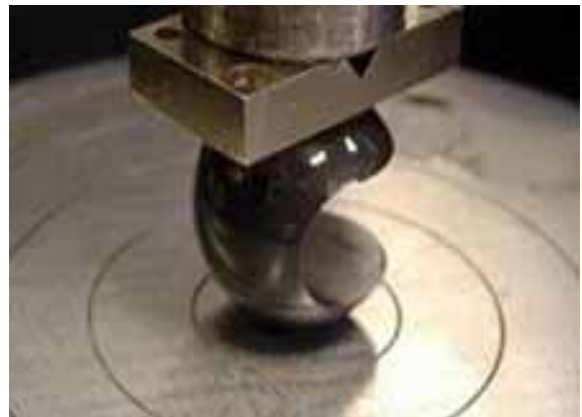


**Figure 3-13: C-Sphere surface strength testing**

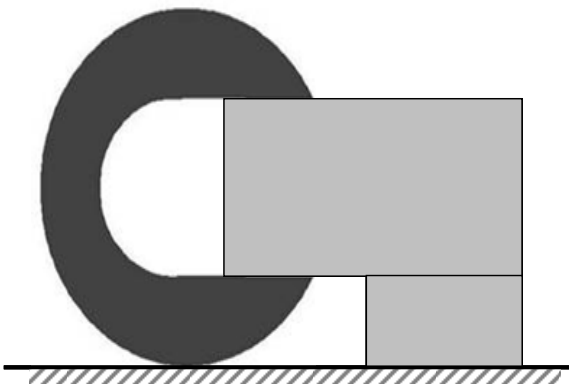


**Figure 3-14: Special jig to position C-Sphere on the test cell.**



**Figure 3-15: Fractured specimen**

#### 3.2.4. C-Sphere Test Results and Discussion

The C-Sphere characteristic strength of the SN101C was approximately 40% higher than that for the NBD200 (1081 MPa versus 778 MPa) while their Weibull moduli were

statistically equivalent (6.0 and 6.5, respectively) – as shown in Figure 3-16. Optical fractography showed that failure always initiated at the surface but not necessarily always exactly at the apex of the outer fibre. The fractography of failure locations of NBD200 specimens are shown in Figures 3-17 and 3-18. Selected specimens were studied under SEM. Magnified failure origin and locations are shown in Figures 3-19 and 3-20. Selected SEM fractography is also shown in Appendix 7.3. According to the effective area dependence on a Weibull modulus shown in Figure 3-11, the effective area for a Weibull modulus of  $\sim 6$  is approximately  $20 \text{ mm}^2$ . As a comparison, the effective area for an ASTM C1161B bend bar is approximately  $100 \text{ mm}^2$  for a similar Weibull modulus. For a hypothetical situation where the same surface-type strength-limiting flaw is operative in both specimen geometries, the characteristic strength of that bend bar geometry should be  $\sim 80\%$  of that for the C-Sphere. Work has been carried out as to how to interpret the meaning of C-Sphere strength and fractography and how that may be related to potential RCF performance. For a fracture toughness of  $6 \text{ MPa}\sqrt{\text{m}}$ , and a crack geometry factor of 1.5, the estimated Griffith flaw size for the specimen shown in Figures 3-17 and 3-18 would be approximately 30 microns respectively. That is of the size scale that has been shown to be a critical size for crack penetration during RCF.

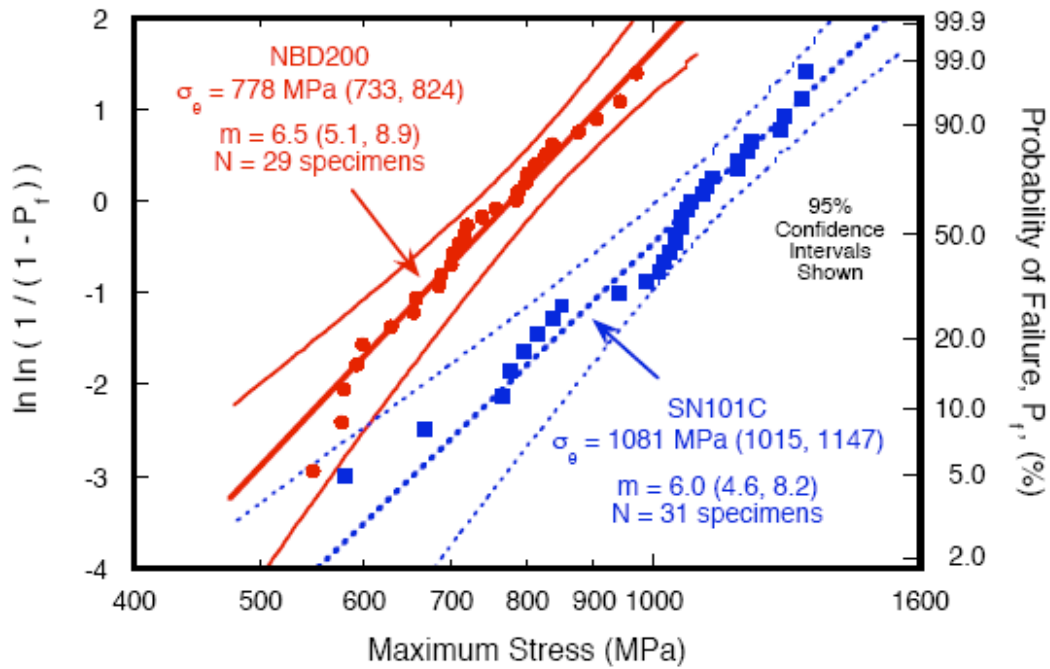
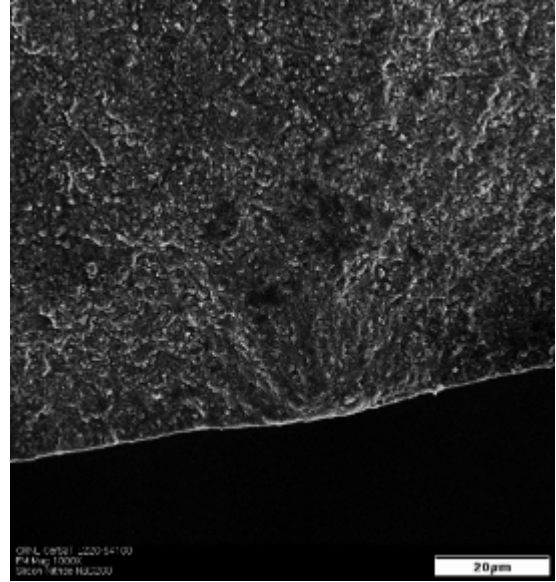
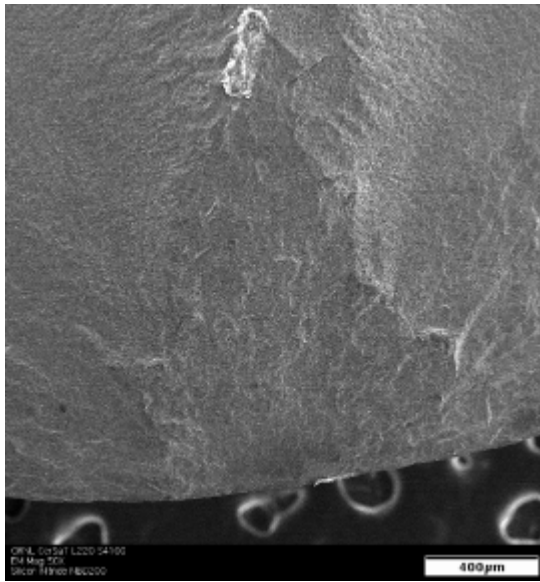
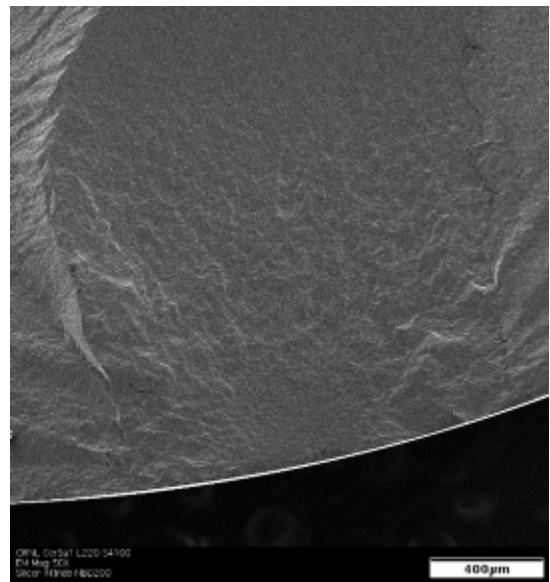
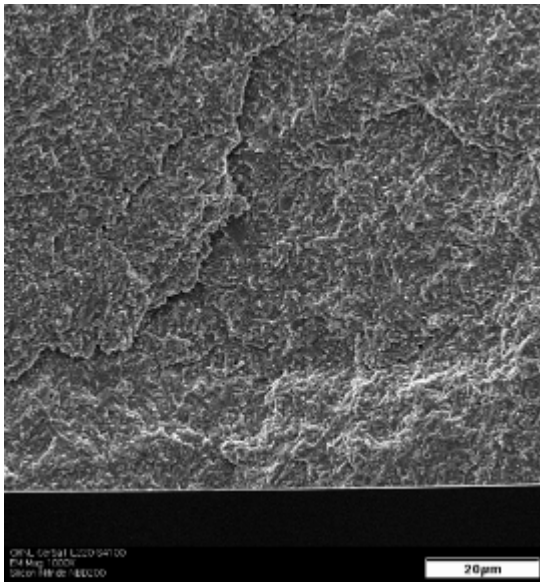


Figure 3-16: C-Sphere Weibull strength distribution of NBD200 and SN101C Silicon Nitride



**Figure 3-17: Fractography of NBD200 specimen number 5 at 50x and 1000x respectively**



**Figure 3-18: Fractography of NBD200 specimen number 7 at 50x and 1000x respectively**

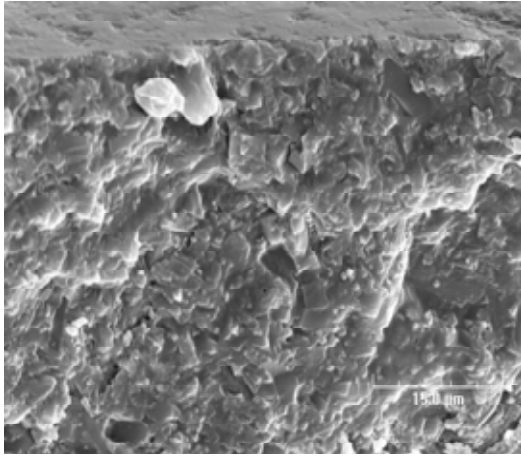


Figure 3-19: Crack initiation location

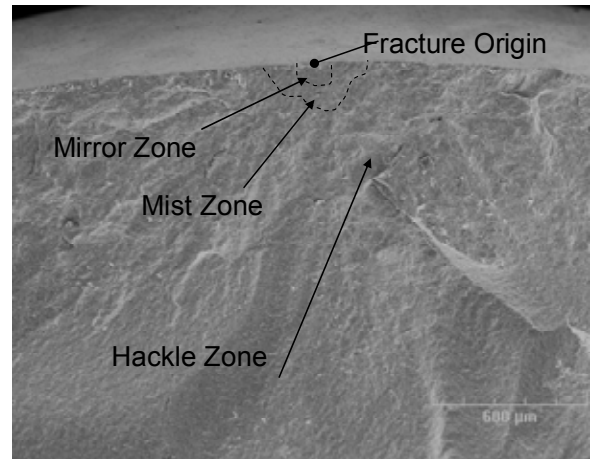


Figure 3-20: Crack initiation origin

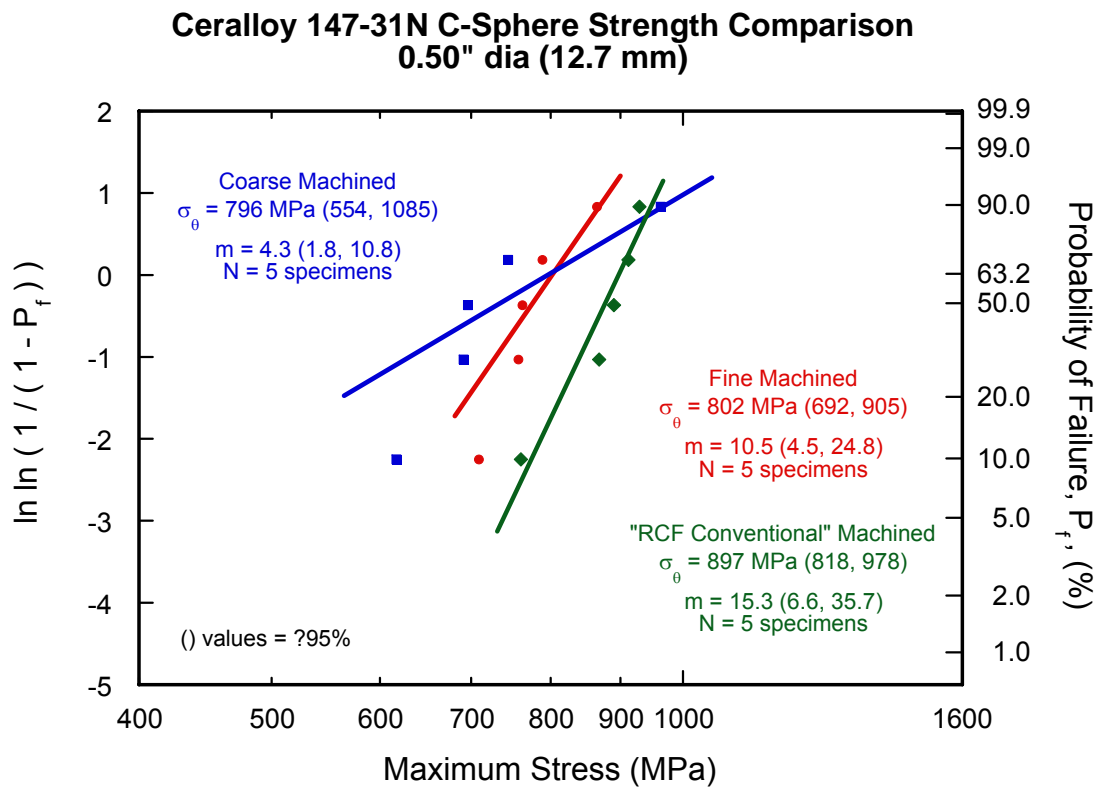
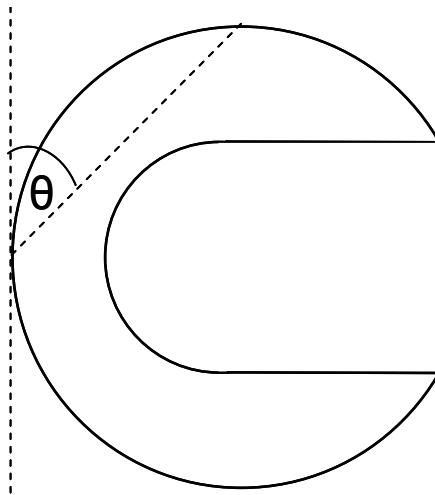


Figure 3-21: C-Sphere Weibull Strength Distribution of Ceralloy Specimens.

C-Sphere flexure strength of coarse, fine and RCF-Conventionally finished Ceralloy specimens are shown in Figure 3-21. The RCF-Conventional Ceralloy specimens had a superior effective strength compared with fine and coarse Ceralloy specimens. It was ~12% and ~13% better than fine and coarse specimens respectively. The trend

corresponds well with half RCF cylinder flexure strength described in section 3.1. With a fracture toughness of  $6 \text{ MPa}\sqrt{\text{m}}$  and approximate crack geometry factor of 1.5, the effective Griffith flaw sizes of coarse, fine and RCF-Conventionally finished specimens are 25.3, 24.8 and 19.9 microns respectively. As mentioned above, these size scales are critical to crack penetration scale in a rolling contact fatigue test. The variation on the flaw sizes in this scale may influence the rolling contact fatigue life of the coarse, fine and RCF-conventionally finished specimens. Investigation was carried out to link the C-Sphere results and RCF results of these three batches of specimens. The RCF results can be seen in Chapter Five.

It is worth mentioning that due to the brittle nature of Silicon Nitride, the surface strength is sensitive to surface defects. As a result of this, the C-Sphere specimen may not necessarily fail at the highest stress location at the outer-fibre of the C-Sphere hoop. It can fail at an angle to the outer-fibre. Theta is defined as the angle between the tangential lines of failure location and outer-fibre location as shown in Figure 3-22.



**Figure 3-22: Definition of angles of failure location**

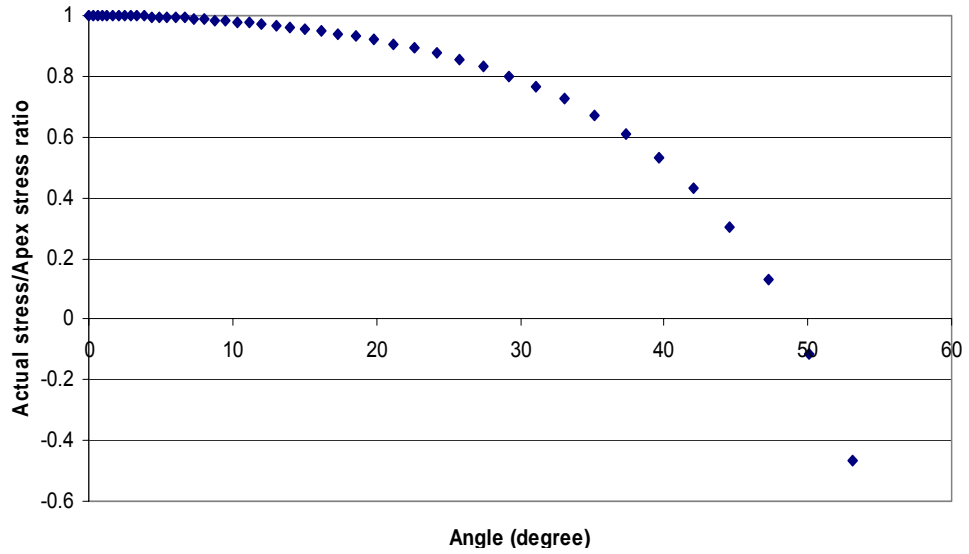


**Figure 3-23: Actual failure stress in relation to failure location angle**

As a result of the difference in failure location, the actual failure stress needs to be exchanged in relation to the failure location theta. Figure 3-23 shows the exchange rate at different theta angles. The failure location was taken into consideration when C-Sphere test results were analysed.

# CHAPTER 4: ELASTIC PROPERTY AND RESIDUAL STRESS OF SILICON NITRIDE

## 4.1 RUS Measurement of Elastic Properties of Silicon Nitride

Due to variations of in the materials property in different batches of Silicon Nitride specimens, a precise measurement of the elastic property is important to compare the rolling contact fatigue result since the elastic property of Silicon Nitride is an important parameter in calculating the contact stress between contact elements. In this chapter, an RUS technique to measure the elastic properties of Silicon Nitride is introduced.

### 4.1.1 Mechanical Measurement of Elastic Properties of Materials

Mechanical laboratory measurements of the elastic properties of materials are broadly classified into three groups: quasi-static, resonance and time-of-flight. These three types reflect the ratio of the wavelength of the mechanical signals used to the size of the specimen under test. Time-of-flight methods measure the transit time of various elastic wave types across the specimen and sometimes alterations in the wave's shape due to attenuation and other phenomena inherent to the sample. These measurements assume wavelengths which are short compared to sample dimensions. For typical specimen lengths of the order of a few centimetres that implies frequencies above 0.5 million Hz. Resonance techniques measure the frequencies of the specimen's elastic resonances, or free oscillations. These frequencies reflect the size, shape and elastic property of the specimen. Each corresponds to a particular bundle of bouncing, interconverting travelling waves which conspire to exactly repeat at intervals of  $1/f$ , where  $f$  is the resonance frequency. The experimental apparatus is simple and easily adaptable to a wide range of sample sizes and shapes. For typical centimetre-sized specimens, the frequency of measurement is normally higher than 5,000 Hz, up to 500,000 Hz. The interpretation of observed frequencies is explained later. Quasi-static methods, such as cyclic loading, subject the sample to deformations that are slow compared to any of its natural mechanical resonances, so that the sample is close to mechanical equilibrium at all times during the test. By measuring the applied stresses and the strains induced, we can infer

the sample's elastic property. Cyclic loading measurement can be made from frequencies between 0-5,000 Hz.

Quasi-static	Resonance	Time of flight
Centimetre to meter-sized	Centimeter-sized	Centimetre-sized
0 – 5, 000 Hz	5,000 – 500, 000 Hz	> 500, 000 Hz

**Table 4-1: Comparison of three techniques broadly used to measure elastic properties of materials.**

The RCF specimens which have a diameter of 12.7 mm and identical spherical shape are good candidate specimens for resonance and time-of-flight measurement. Due to the relative simplicity of resonance measurement equipment and interpretation of data, Resonance Ultrasound Spectroscopy (RUS) measurement is widely used in the laboratory.

#### 4.1.2 RUS Measurement Equipment

The RUS measurement was carried out on the Quasar International Resonance Ultrasound Spectroscopy as shown in Figure 4-1.



**Figure 4-1: Quasar International Resonance Ultrasound Spectroscopy.**

The Silicon Nitride specimen was secured by three acoustic probes, which contained one acoustic generator and two acoustic receivers. All three probes were connected to an acoustic processor for data analysis. The schematic of the measurement setup is shown in Figure 4-2.

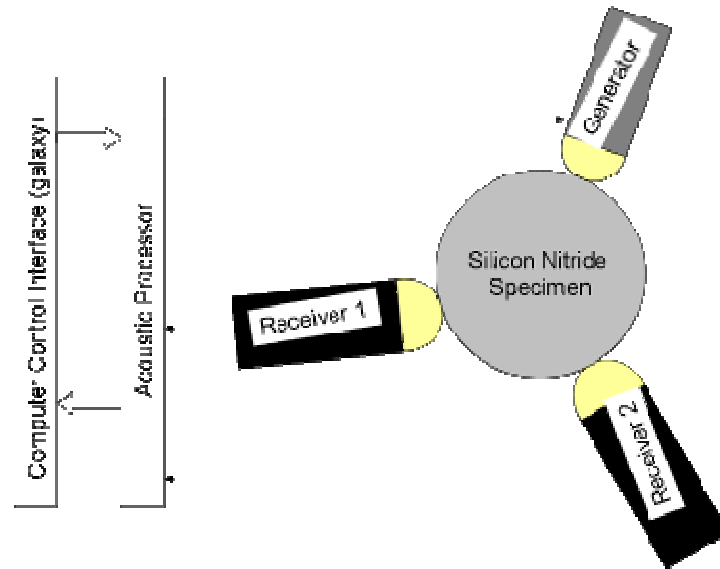


**Figure 4-2: Schematic of RUS measurement**

#### 4.1.3 RUS Measurement Methodology

RUS is based on the principle that the mechanical resonance of a component depends on its shape, density, and elastic properties in a manner such that a measurement of the resonant frequencies provides a signature that is unique to the component. A resonance spectrum is generated by sweeping the frequency of an ultrasound signal applied to the components and by detecting its resulting resonance frequencies. Changes in the shape, density or elastic properties, or introduction of defects, lead to a variation of this signature. Advantages of RUS include: high sensitivity - very small deviations in  $E$ ,  $G$ , and  $\nu$  are detectable; quick testing - testing duration is only a few seconds, and; flexural, torsional, and longitudinal resonance modes being excited - which enables modal signature analysis that produces independent determinations of  $G$  and  $E$  or  $\nu$ . The excitation of only one of those three modes is limiting because it requires the assumption of a value of  $E$  (or  $\nu$  more commonly) to determine the values of all three elastic constants.

An example of a RUS spectrum is shown in Figure 4-3. The frequencies at which there are resonances are unique to the geometry and density of the material and the specific values of  $E$ ,  $G$ , and  $\nu$ ; knowledge of the geometry (i.e. accurate diameter measurement of a sphere, etc.) and density (a parameter easy to accurately measure with simple

geometries) facilitate RUS analysis. This fact allows the RUS user to accurately determine E, G, and  $\nu$  by numerically varying the values of E, G, and  $\nu$  until a unique, three-way combination produces a match of experiment and modal resonance theory.

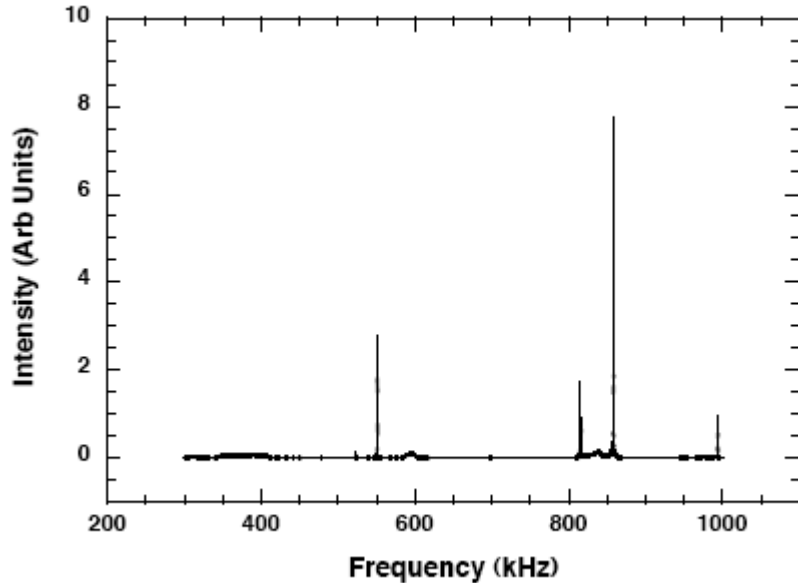


Figure 4-3: RUS Spectrum

The RUS's software does not accommodate analysis of materials in a spherical geometry so modal analysis resulting from finite element analysis, FEA, (e.g. ANSYS), in combination with the capturing of resonance frequencies from any two of the three resonance modes (i.e. flexural, torsional, and longitudinal), was used to accomplish this. The method consists of (1) running three FEA modal analyses for a given geometry and material density, with the “bracketing” of two of the three elastic constants (e.g. E and  $\nu$ ), and (2) fitting their functionalities to the measured resonance frequencies. For example, if the specimen was a half inch diameter Toshiba TSN03NH Silicon Nitride ball, and its E and  $\nu$  were estimated to be 320 GPa and 0.28, respectively, then the three E -  $\nu$  combinations for the three modal analyses could be chosen to be: 320 GPa - 0.20; 400 GPa - 0.20, and; 400 GPa - 0.35. These FEA results then enable the determination of the torsional frequency ( $f_{tors}$ ) and a flexural resonant frequency ( $f_{flex}$ ) as multilinear functions of E and  $\nu$  for the modelled geometry and density; namely,

$$f_{\text{tors}} = A_t + B_t \cdot E + C_t \cdot \nu \quad \text{Eq. 4-1}$$

$$f_{\text{flex}} = A_f + B_f \cdot E + C_f \cdot \nu \quad \text{Eq. 4-2}$$

where  $A_t$ ,  $B_t$ , and  $C_t$  are regression constants for  $f_{\text{tors}}$  and  $A_f$ ,  $B_f$ , and  $C_f$  are constants for  $f_{\text{flex}}$ .

Torsional ( $f_{\text{tors}}$ ) and flexural ( $f_{\text{flex}}$ ) resonance frequency are measured with the RUS and then applied against Eqs 4-1 and 4-2. above. A unique combination of  $E$  and  $\nu$  does not represent the measured torsional or flexural frequency singly since there is actually a locus of  $E$ - $\nu$  pairs that does this. However, a unique  $E$ - $\nu$  combination does result when those two resonances are combined, see Figure 4-4. For example, the locus of  $E$  and  $\nu$  that satisfies a torsional frequency of 401.2 kHz intersects the locus of  $E$  and  $\nu$  that satisfies the flexural frequency of 529.3 kHz at one  $E$  and  $\nu$  pair - it is that  $E$  and  $\nu$  pair that satisfy Eqs. 4-1 and 4-2 and that are the elastic properties of the test. That unique  $E$  and  $\nu$  pair, when re-inputted in the modal analysis, will predict resonant frequencies that match all the experimentally identified RUS peaks in a spectrum, such as shown in Figure 4-3. This action serves as a verification of the determined  $E$  and  $\nu$  pair.

#### 4.1.4 RUS Measurement Results

Six batches of specimens with 10 in each batch were examined using RUS measurement. The residual stress measurement was carried out in Japan by a collaborator Professor Tobe. The method and specification of the measurement was discussed and decided while Professor Tobe visited Bournemouth University.

Figure 4-5 shows the results of three batches of SRBSN specimens with coarse, fine and RCF-Conventional finishing conditions respectively. The RUS results indicated that the difference of subsurface damage introduced in the machining process did not significantly affect the elastic property of Silicon Nitride. The exceptions in the data shown in the circle were largely due to the mass variation of the specimens, which was possibly a result of inhomogeneity or porosity in the primary processing. In order to be consistent in the RCF test results, these specimens were excluded from the tests.

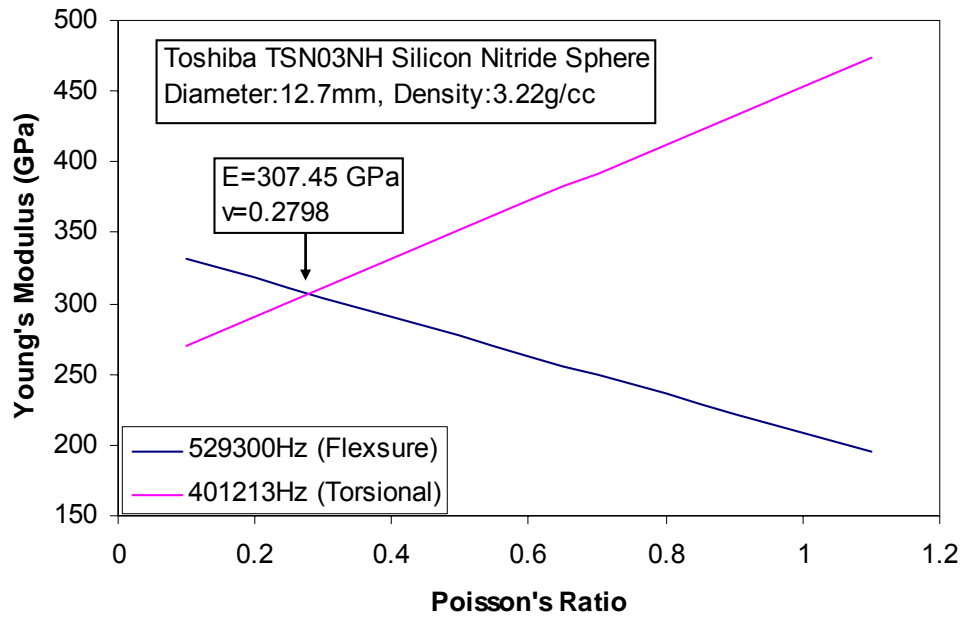


Figure 4-4: A unique combination of elastic properties satisfies both resonance frequencies

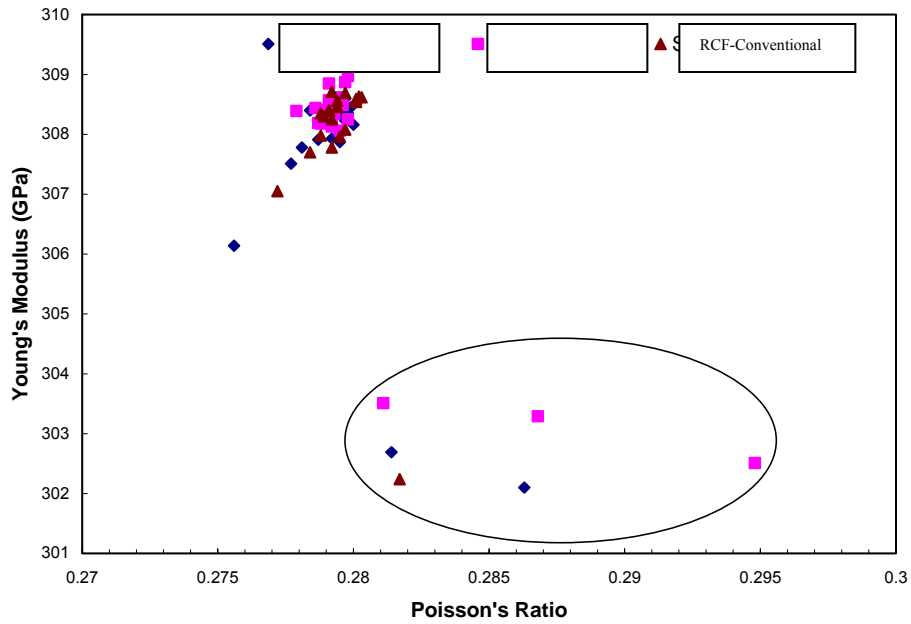
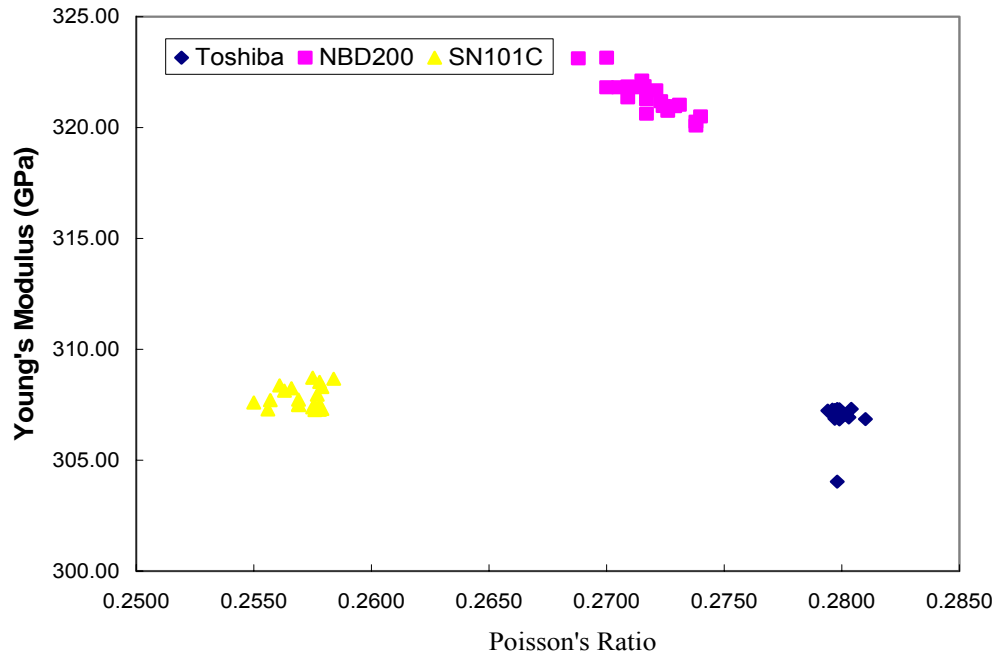


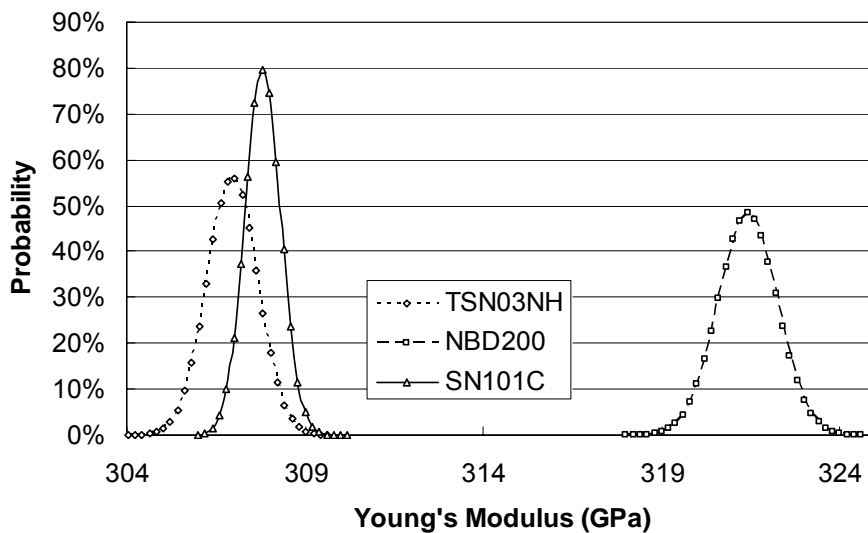
Figure 4-5: Elastic properties of Ceralloy 147-31N SRBSN measured from RUS Spectroscopy

Figure 4-6 shows the results of another three batches of Silicon Nitride material representing Toshiba TSN03NH, NBD200 and SN101C respectively. These three Silicon Nitride specimens were all subjected to the HIPing process, but the difference in additives and processing parameters gave them different elastic properties.



**Figure 4-6: Elastic properties of three HIPed Silicon Nitrides.**

The normal distribution of the measured Young's modulus below shows that NBD200 material had a higher Young's modulus than TSN03NH and SN101C material. TSN03NH material had a narrower range of distribution, which indicates that TSN03NH has better consistency in material processing and specimen geometry control in the manufacturing process.



**Figure 4-7: The normal distribution of elastic properties measured on three commercial grade HIPed Silicon Nitrides**

The variation in Young's modulus can result in a change in Hertzian Contact Stress when the Silicon Nitride balls are subjected to RCF testing. Without accurate Young's modulus measurement and Poisson's ratio measurements, the generic Young's modulus and Poisson's ratio of 315 GPa and 0.280 were used when calculating the Hertzian contact stress. As shown in Figure 4-8 below, these two values could vary depending on the supplier of the Silicon Nitride ball, and they also varied within the same batch of specimens from the same supplier. To ensure an accurate account of Hertzian stress, the RUS measurements were fed into the Hertzian stress calculation model when SRBSN Silicon Nitride balls were RCF tested.

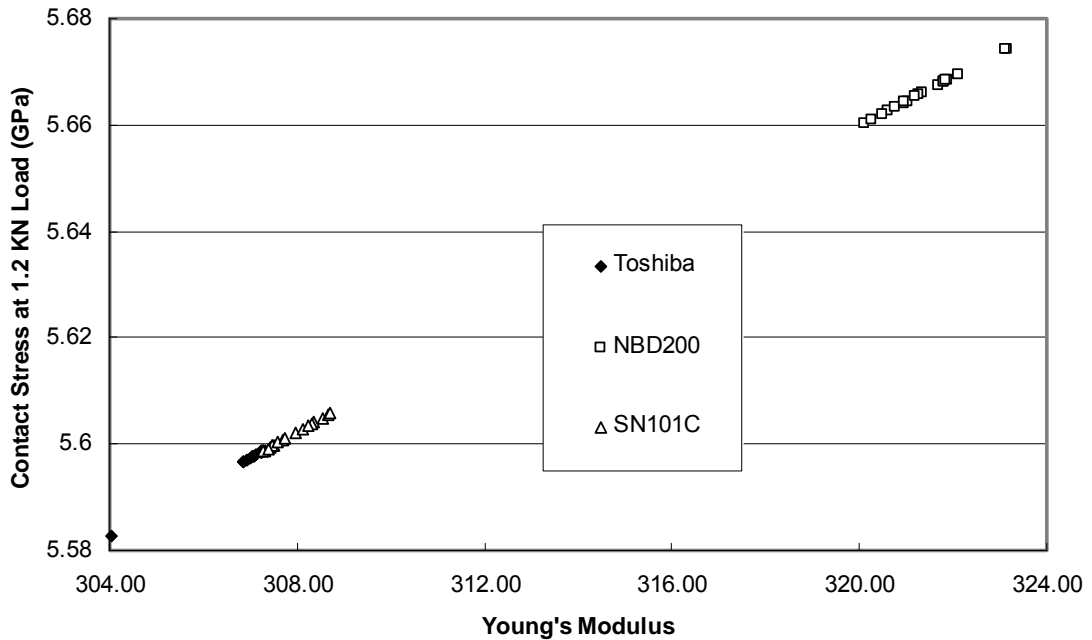


Figure 4-8: The effect of Young's modulus on Hertzian contact stress

## 4.2 Residual Stress Measurement

### 4.2.1 Type and Measurement of Residual Stress

Depending on the characteristic length, residual stress can be classified into types I, II and III. These three types of stress equilibrate in different length scales. Type I stress is a macroscopic stress which equilibrates over a large dimension which normally corresponds to the size of the structure. In the case of ball bearing elements, type I stress equilibrates over the ball diameter, which is around 12.7 mm. Type II stress is a mesoscale stress which equilibrates over several grains within the microstructure. In the case of Silicon Nitride, the Silicon Nitride phase grain size is around 4-10 microns. The characteristic length of type II stress of Silicon Nitride is around 10-100 microns (~3-10 times of grain size). Type III stress is a microscopic stress which equilibrates within a particular grain. The characteristic length is smaller than a typical grain size, and in the case of Silicon Nitride, it is smaller than 10 microns. Type III stress is normally caused by defects in the crystal structure in a crystalline material, such as dislocation, vacancy etc. The schematic in Figure 4-9 illustrates types I, II, III stresses.

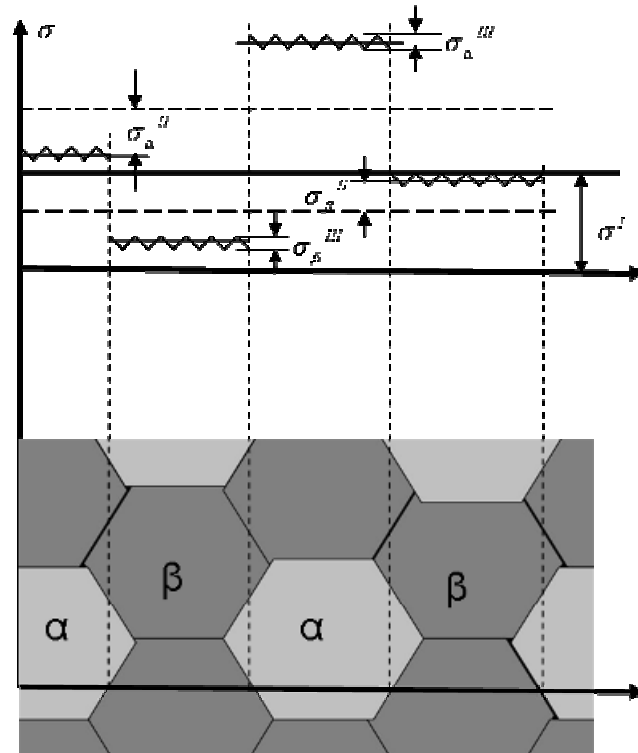
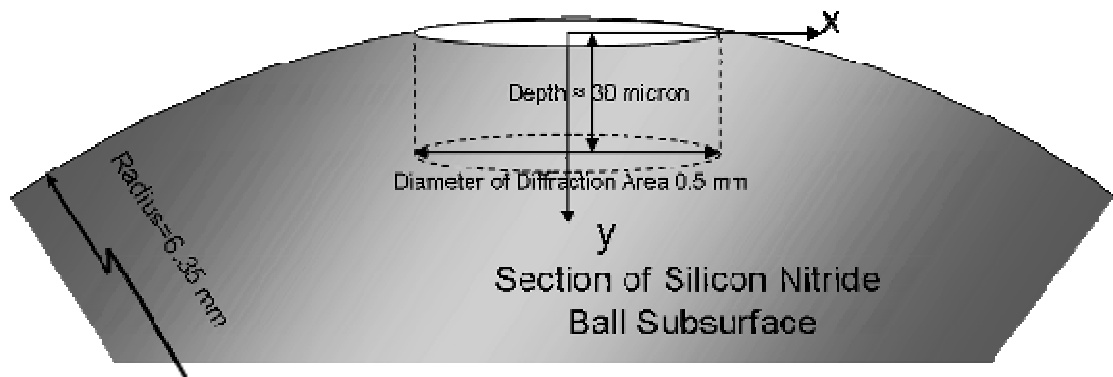


Figure 4-9: Three types of residual stresses classified by the length scale

By broad classification, residual stress measurement technique can be put into three groups, mechanical stress measurement, diffraction methods, and other methods, which include Raman spectroscopy, photo-elasticity, magnetic method and ultrasonic method etc. By the nature of the measurement, the techniques can be classified into non-destructive and destructive techniques. The most widely used mechanical stress measurement techniques include hole drilling and curvature method. In this study the X-ray diffraction technique is used to study the residual stress of SRBSN Silicon Nitride ball elements. According to the residual stress classification discussed earlier, the residual stress measured on Silicon Nitride balls is type II residual stress as the typical length in the measurement is 30 microns in depth, as shown in Figure 4-10.



**Figure 4-10: The penetration and measured volume on Silicon Nitride using XRD technique**

One of each specimen with coarse, fine and RCF-Conventional machining conditions was measured to quantify the residual stress of these specimens using X-ray diffraction technique. The measurements were carried out in Japan with the XRD machine shown below in Figures 4-11 and 4-12.



**Figure 4-11: XRD machine**



**Figure 4-12: XRD machine specimen chamber**

The residual stress of SRBSN Silicon Nitride can be introduced through two processes, sintering and machining. Sintering process normally introduces compressive residual stresses as the density of the Silicon Nitride powder is reduced at high temperature and high pressure. There is argument over whether grinding or lapping processes increases or reduce the compressive residual stress. As the coarse, fine and RCF-conventional specimens are machined from the same bill of raw material with the same sintering process, it is assumed that the compressive residual stress value prior to the beginning of the grinding process is the same, and the variation in compressive residual stress value can only be introduced by the grinding process.

#### **4.2.2 Residual Stress Result and Discussion**

Five measurements on each specimen were carried out, and residual stress measurement results are shown in Tables 4-2 to 4-5 below. When the measurement was carried out on the coarse specimen, a different sampling time of 120 seconds was selected. In order to maintain the consistency for comparison, the measurement on the coarse specimen was redone at 1200 seconds sampling time.

No.	Sampling Time (seconds)	Compressive Residual Stress	Reliability(+/-)
1	1200	57.237	71.62
2	1200	120.703	87.87
3	1200	248.948	44.98
4	1200	137.816	115.42
5	1200	11.26	61.18
Average	1200	115.1928	76.214

**Table 4-2: Residual stress of coarse SRBSN specimen**

No.	Sampling Time (seconds)	Compressive Residual Stress	Reliability(+/-)
1	120	283.883	92.18
2	120	345.362	59.45
3	120	365.289	48.95
4	120	315.019	72.16
5	120	467.312	78.65
Average	120	355.373	70.278

**Table 4-3: Residual stress of coarse specimen with 120 seconds sampling time**

No.	Sampling Time (seconds)	Compressive Residual Stress	Reliability(+/-)
1	1200	313.752	55.13
2	1200	285.128	50.33
3	1200	264.081	38.34
4	1200	426.994	59.72
5	1200	326.392	90.93
Average	1200	323.2694	58.89

**Table 4-4: Residual stress of fine SRBSN specimen**

No.	Sampling Time (seconds)	Compressive Residual Stress	Reliability(+/-)
1	1200	331.55	36.09
2	1200	357.042	53.14
3	1200	384.396	54.33
4	1200	335.444	36.73
5	1200	361.982	43.97
Average	1200	354.0828	44.852

**Table 4-5: Residual stress of RCF-conventional specimen**

The residual stress measurements with the reliability values are shown in Figure 4-13. Measurements on RCF-Conventional specimens had the smallest variation with higher reliability. In contrast, measurements on coarse specimens had the largest variation with lower reliability. The difference in reliability and variation was an attribute of the measurement technique rather than the intrinsic property of the specimens on which the measurements were carried out.

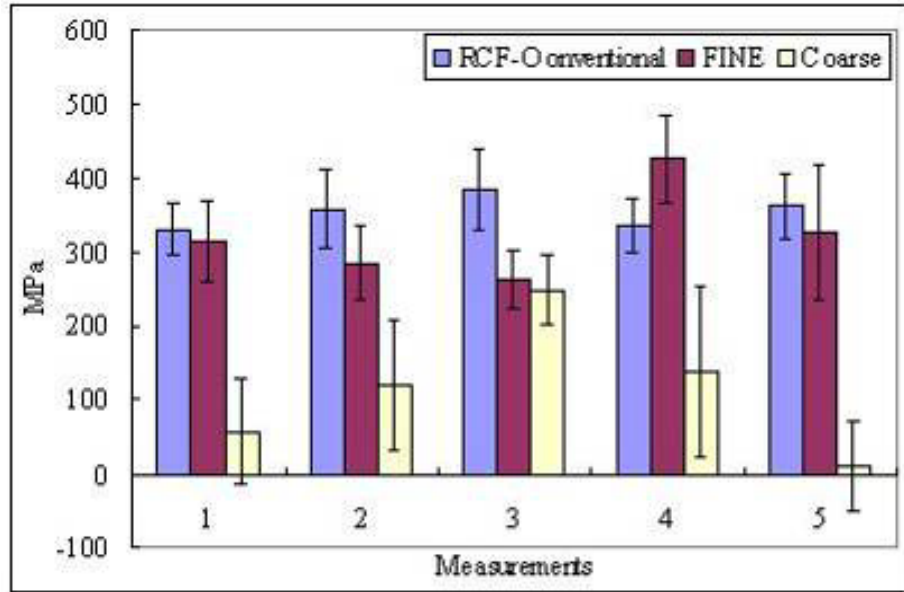


**Figure 4-13: Residual stress of SRBSN specimens with three surface finishing conditions**

The average values of five residual stress measurements of coarse, fine and RCF-conventional specimens are compared in Figure 4-14. The coarse specimen had the lowest average compressive residual stress value, and the RCF-conventional specimen had the highest average compressive residual stress value. The variation in residual stress value could only be a result of the different machining process of these specimens, as the compressive residual stress value should be the same after the sintering process and prior to grinding process. As the coarse specimen was the most aggressively-machined with the larger and coarser grit diamond-dressed grinding wheel, the aggressive machining procedure could be a mechanism to reduce the compressive residual stress. This corresponds to the higher values in the less aggressively-machined fine and RCF-conventional specimen. As compressive residual stress is beneficial to the RCF performance of the specimen, the coarse specimen with a lower residual stress value is

expected to perform worse even without taking into account the subsurface damages introduced by the aggressive machining based on this observation.

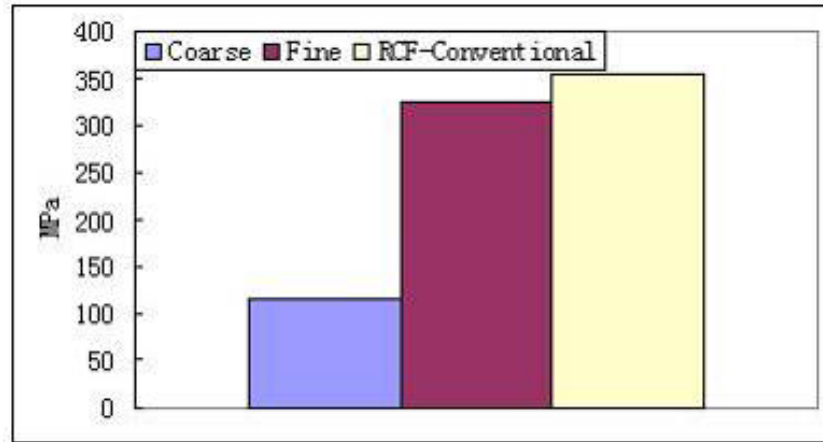


**Figure 4-14: Comparison of average residual stress of specimens with three surface finishing conditions**

It is also interesting to note that varying the sampling time can change the result of residual stress measurement significantly. Figure 4-15 compares the measurement on the coarse specimen with 120 seconds and 1200 seconds sampling time. The compressive residual stress value measured with 120 seconds sampling time was significantly higher than with 1200 seconds sampling time. The actual reason for this variation is not understood in this study, and better understanding of the mechanism is worth pursuing in future works.

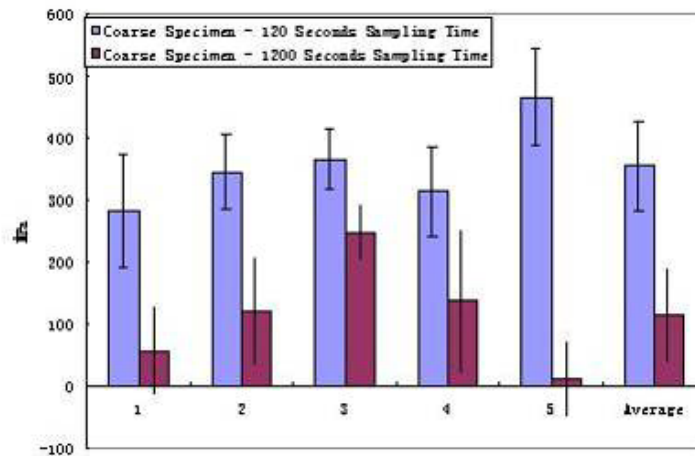


**Figure 4-15: Coarse specimen with different sampling time**

# CHAPTER 5: ROLLING CONTACT FATIGUE

## 5.1 Rolling Contact Fatigue Methodology

Rolling Contact Fatigue of ceramics has been studied on various tribotesters over the years. In the United Kingdom, a widely used method is a four-ball test, where three steel plenary balls are driven by a ceramic ball. In the United States, the ball-on-rod is a popular setup, where three steel balls are driven by a ceramic rod. This section presents the methodology of conducting rolling contact fatigue using both types of tester. The mechanism of these two types of tribometers is described in detail, including the contact geometry, contact stress etc. Comparison are also drawn with these two types of tester.

### 5.1.1 Modified Four Ball Test

A PLINT modified four-ball tribotester is used to investigate the RCF performance of Silicon Nitride balls. The setup of the four-ball test is shown in Figure 5.1 below. The upper Silicon Nitride ball is press-fitted into a steel collet, which is driven by a spindle to rotate at a speed up to 20000 rpm. Three AISI 52100 steel balls are used as contact balls. Lubricant level is maintained in the cup by either topping up at regular intervals or through a timer connected to a micropump.

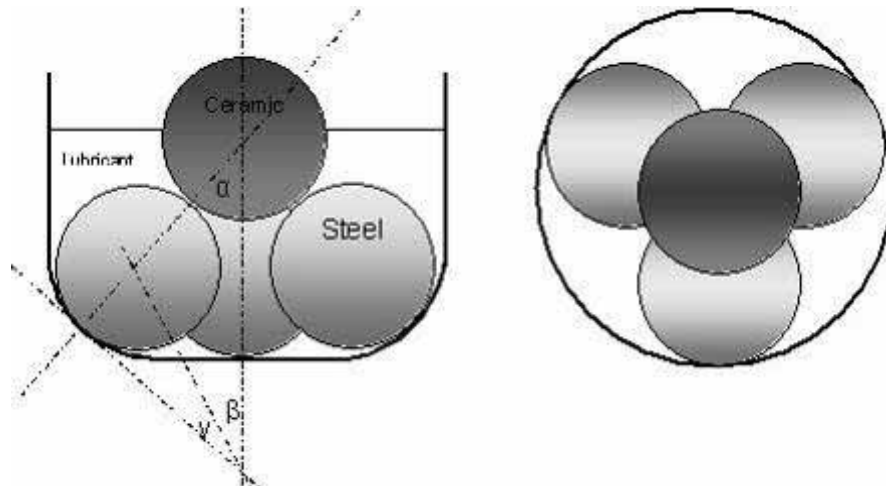


Figure 5-1: The schematic of four-ball contact

The ceramic ball and steel balls are of the same diameter. From the contact geometry shown in Figure 5-2, the Hertzian contact stress can be calculated through Eqs 5-1 to 5-4, where  $R_1$  is the effective radius,  $E_1$  is the effective modulus,  $P_{\text{machine}}$  is the pneumatic loading applied through spindle.

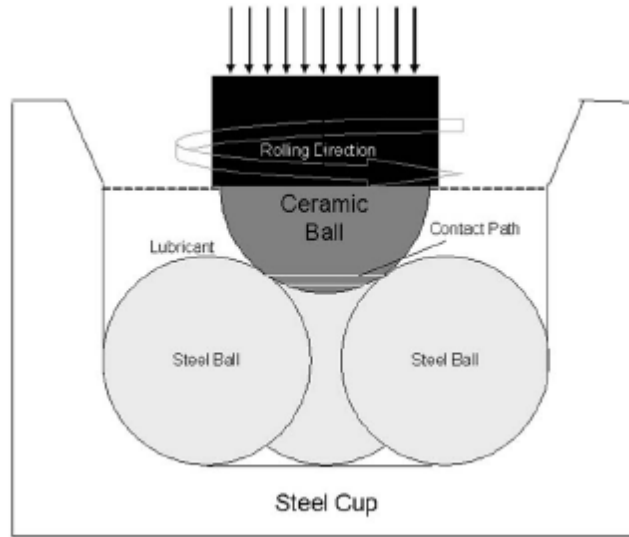


Figure 5-2: Four ball contact geometry

$$\frac{1}{R_1} = \frac{1}{R_{\pm}} + \frac{1}{R_0} \quad \text{Eq. 5-1}$$

$$P = \frac{P_{\text{machine}}}{3 \cos(35.3^\circ)} \quad \text{Eq. 5-2}$$

$$\frac{1}{E_1} = \frac{1-\nu_{\pm}^2}{E_{\pm}} + \frac{1-\nu_0^2}{E_0} \quad \text{Eq. 5-3}$$

$$P_0 = \left[ \frac{6PE_1^2}{\pi^3 R_1^2} \right]^{\frac{1}{3}} \quad \text{Eq. 5-4}$$

$P_0$  is the calculated Hertzian contact stress, which can be accurately controlled by adjusting the pneumatic loading  $P_{\text{machine}}$  from the machine load cell input. The relationships between  $P_{\text{machine}}$  and  $P_0$  are shown in Appendix 7.4. The tribometer is capable of running at a speed of up to 20000 rpm and a load of up to 4 kN  $P_{\text{machine}}$ , however, for the majority of the tests carried out on this machine in this study, the speed is set at 5000 rpm, and  $P_{\text{machine}}$  load is adjusted to achieve 5.6 GPa compressive Hertzian stress. For Silicon Nitride and steel ball contact, 5.6 GPa Hertzian contact stress is normally achieved by applying approximately 1.2 kN  $P_{\text{machine}}$  loading.

### 5.1.2 Ball-on-Rod Test

The ball-on-rod RCF bench tester has been widely used in the United States to examine rolling contact fatigue performance of steel and Silicon Nitride materials. In order to systematically examine the RCF performance of Ceralloy 147-31N SRBSN, tests are performed on a ball-on-rod tester in order to compare the results acquired from the modified four-ball tester.

Compared with the modified four-ball machine which has a pneumatic loading system, the ball-on-rod tester only has a spring-loading system. The advantage of a spring loading system is that it simplifies the design of the tester, hence it can reduce the fixed cost of performing RCF test. It also makes calibration easier to perform. However due to the nature of spring-loading, the exact load applied to the specimens cannot be justified. During the course of the experiments, the test rod rotates at the centre of the head where insignificant change of alignment, due to events such as wear of contact balls and races, could result in the tilting of the test head, which in turn could affect the load applied to the test coupons. The test head needs to be calibrated after three tests, or in order to achieve an optimal result, be calibrated after each test. The detail of the ball-on-rod machine and calibration of its test head is described in Appendix 7-5. The contact geometry of the ball-on-rod tester is shown in Figure 5-3. The Hertzian stress can be developed through classical contact mechanics theory and the deduction of the Hertzian contact stress is shown in Appendix 7-6.

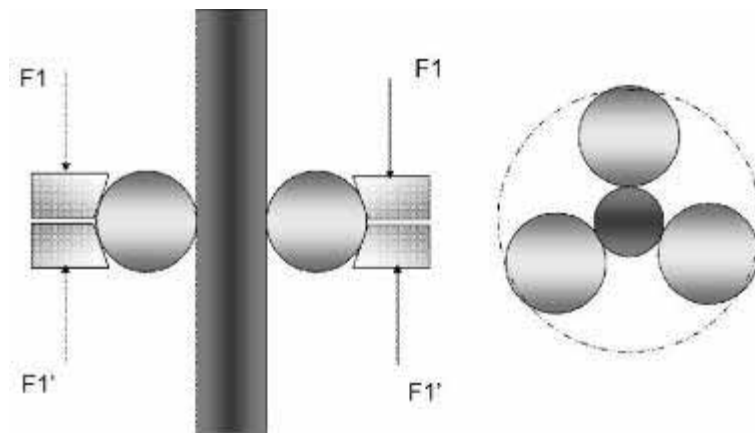


**Figure 5-3: Ball-on-Rod contact geometry**

The RCF rod is driven by an electric motor rotating at a fixed speed of 3600 rpm. The steel balls are pressed against the Silicon Nitride rod by a spring. The load from the spring is adjustable to achieve desired Hertzian contact stress. Drift lubrication is applied to the top of the Silicon Nitride rod and the lubricants flow down the Silicon Nitride rod as a result of gravity. The lubricants are collected at the bottom of the test head in a tray to be recycled.

### 5.1.3 Four-Ball and Ball-on-Rod Tribometers: Comparison

The characteristics of the two testers are compared in Table 5-1. From the comparison, it can be seen that the four-ball tester, with a computered controlled pneumatic loading system, offers better flexibility and reliability than the ball-on-rod tester. However, the ball-on-rod excels in simplicity and multi-testing at the same time with its four test heads per machine. The ball-on-rod tester also gives 2.5 fatigue cycles per revolution, which is more than the 2.25 cycles per revolution of the four-ball tester.

The ball-on-rod tester test head is driven by a motor rotating at a fixed speed of 3600 rpm, and compared with the adjustable speed motor on the modified four-ball machine, it offers less flexibility. The modified four ball machine also offers the capability to vary the temperature of the test environment by heating up the the test chamber using an electrical heating device. This provides the possibility to investigate temperature effect on the rolling contact performance of Silicon Nitride.

From the lubricant point of view, the ball-on-rod tester has an advantage of drift lubrication which can prevent the debris staying in the contact chamber, hence preventing the onset failure of debris effect. The four-ball machine has three built-in sensors to monitor the vibration, temperature and torque of the specimens undergoing an RCF test. If the data acquired through the test exceeds the pre-set value, the alarm is automatically triggered which signals either fatigue failure or any unexpected event. The fatigue failure is monitored by a vibration transducer attached to the test head on a ball-on-rod tester, which stops the tester when excessive vibration is detected.

Machine	Loading	Speed	Lubrication	Calibration	Temperature control	Fatigue cycles per revolution	Data Acquisition	Sensor
Four-ball	Computer controlled pneumatic system	Computer controlled adjustable speed up to 20,000 rpm	Lubricant sealed into the cup	Complicated. Accuracy can be guaranteed. Not needed when change of load.	Yes	2.25	Automatic	Temperature, Vibration, Torque
Ball-on-Rod	Manual spring-loading	Fixed speed 3600 rpm, (unless change of motor)	Drift lubrication which requires lubricant recycling	Simple, is required every four tests or each time of changing load, Accuracy cannot be guaranteed.	No	2.5	Manual	Vibration

Table 5-1: Comparison between modified four-ball machine and ball-on-rod machine

Micro-slip is of great significance in rolling contact fatigue and it happens at the lower edge of the contact area. It occurs due to material deformation in the contact area. As two balls in contact are compressed together, the contact area can be calculated according to Hertzian contact. The difference in absolute velocity in the contact area of the two balls results in micro-slip. For the modified four ball, the micro-slip has been calculated previously, and the negative slip as a function of upper ball loading is shown in Figure 5-4. The relative lower negative slip of ceramic and ceramic contact is a result of high rigidity of ceramic. The spin/roll ratio at the lower edge of the contact area decreases with the increasing upper ball loading.

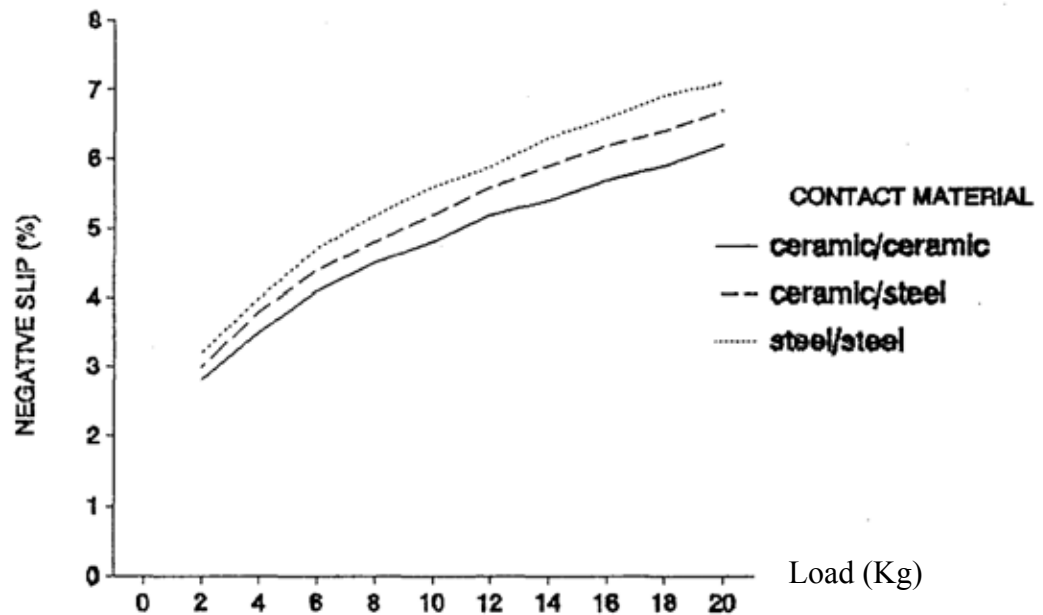


Figure 5-4: Negative slip of ball-ball contact of modified four ball machine (Hadfield 1993).

The micro-slip in the contact area of ball-on-rod rig is also analysed. Given the ball/rod contact geometry and motor-driven rod rotating direction, the micro-slip is considered to be minimal, and the ball-on-rod contact is considered to be close to pure rolling contact.

#### 5.1.4 Surface Defects and Artificial Defects Introduction

Surface defects can be found in commercial Silicon Nitride bearing elements. Among those defects, star defects and ring cracks are the most common types. In rolling contact fatigue test, the defects are the place where RCF spalls initiate, so understanding of the generation of these defects and their propagation under contact stresses is crucial to bearing manufacturer. Ring cracks are generated during handling or logistics processes, where Silicon Nitride balls collide with each other or collide with other hard surfaces. They can be found in commercial Silicon Nitride where they act as the main fatigue-life-limiting defects. The natural ring cracks found on the commercial ball surface are relatively small, so it is hard to investigate their impact on rolling contact fatigue life in a reasonably short time on a bench tester. In order to do this, artificial cracks are created. Artificial cracks are created on the coarse, fine, RCF-conventional machined SRBSN ball surfaces and lapped SRBSN ball surfaces to accelerate the failure of the test specimens. A modified Plint TE 15 impact tester, as shown in Figure 5-5, is used to generate the cracks. A test specimen is attached to a pendulum, and released at a 60 degree angle to collide with a fixed contact ball, as shown in Figure 5-6. The schematic of the artificial crack creation process is shown in Figure 5-7. The energy absorbed during the contact can be calculated by the potential energy lost. The contact ball used for the artificial crack generation is Toshiba HIPed Silicon Nitride. Figures 5-8 show the artificial crack under ultra-violet (UV) light after dye penetration.



**Figure 5-5: Plint TE 15 impact tester**



**Figure 5-6: Fixed contact ball**

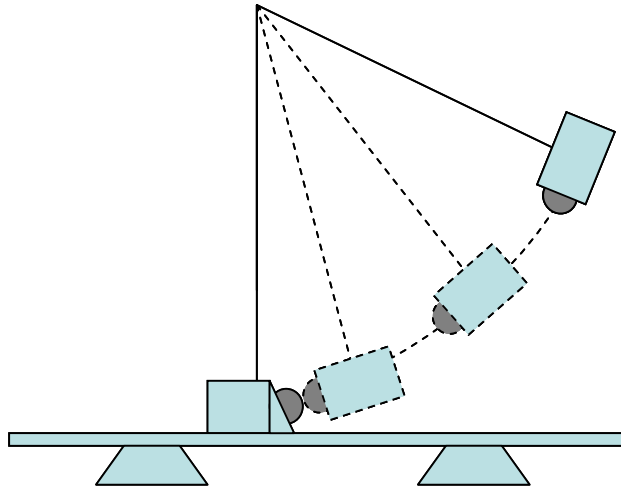


**Figure 5-7: Schematic of artificial crack creation**

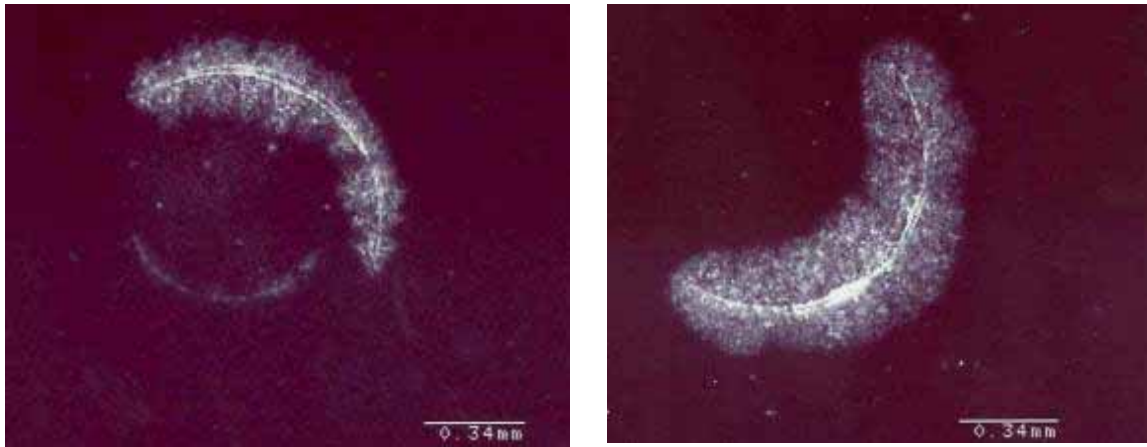


**Figure 5-8: Artificial crack under UV light**

The characteristics of the cracks can be further quantified using an electron microscope to measure the crack gap, using Zygo interferometer to measure the height of the crack gap if required. The pictures show typical 60 degree cracks artificially created on a core drilled SRBSN.

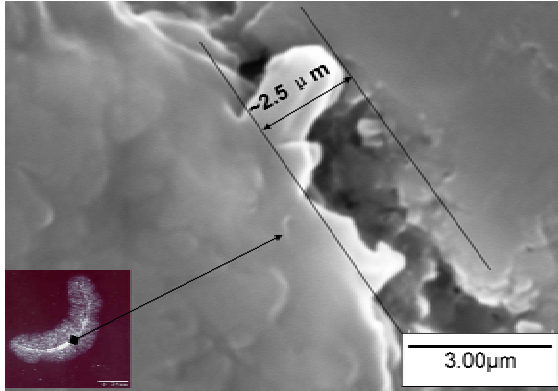


Figure 5-9: Crack gap under SEM

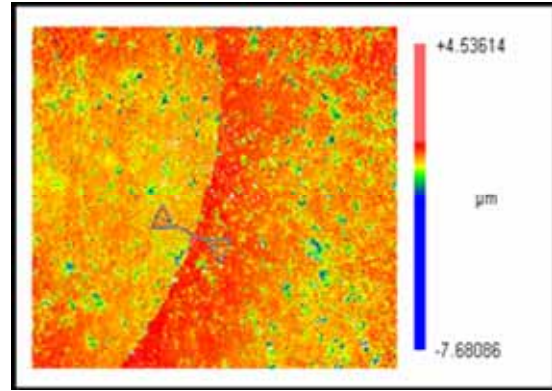


Figure 5-10: Crack as visualised on Zygo interferometer

The centre of contact path on the upper Silicon Nitride balls situated at 1.17 mm above the bottom of the ball. In order to classify the position of the crack within the contact path, the positioning parameters of the crack, and some typical positions of the crack are shown in Figure 5-11.

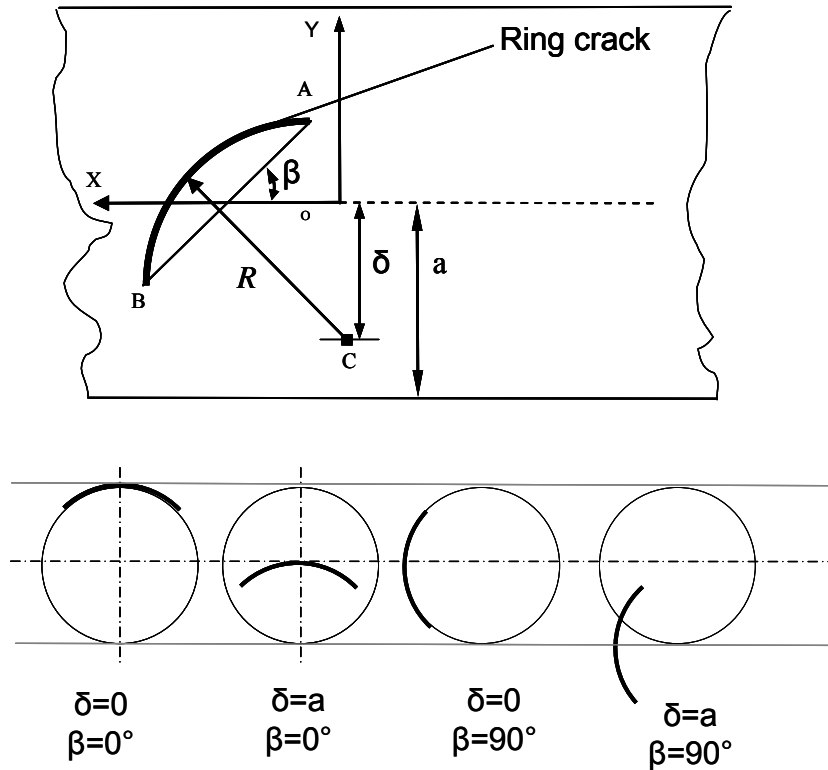


Figure 5-11: Positioning of cracks in the contact path of four-ball contact (Wang and Hadfield 2002).

As shown in the schematic,  $\beta$  measures the angle between the ring crack and the contact path centre line.  $2a$  is the width of the contact path, and  $R$  represents the radius of the ring crack.  $\delta$  measures the distance between the centre of the hypothetical ring crack circle and the centre line of the contact path. In this thesis, all the rolling contact fatigue investigations are carried out on SRBSN balls with artificial cracks created on the surface to accelerate the failure.

## 5.2 Rolling Contact Wear

The rolling contact wear of SRBSN ball and rod specimens with coarse, fine and RCF-conventional surface finishing conditions were studied on a modified four-ball tester and ball-on-rod tester respectively. Rolling contact wear is not an important issue of commercial grade Silicon Nitride ball-bearing elements such as NBD200 and Toshiba because of their good surface quality with an average roughness of 2-4 nm. However, the Ceralloy SRBSN Silicon Nitride balls were grinding finished to an average roughness of 100-300 nm. It was important to see if the surface roughness affected the rolling contact performance of Silicon Nitride balls or led to other failure mechanisms. Another important aspect to note is that with the rolling contact wear on the surface, the desired Hertzian contact stress can be significantly reduced as a result of the contact profile change as shown in Figure 5-12.

The ball diameters of steel and Silicon Nitride were  $R_1 = R_2 = 6.35$  mm, and by trigonometry calculation, the radius of curvature of the wear path was  $R_2' = 125$  mm. Contact stress reduction as shown in Figure 5-13 was achieved by applying classical Hertzian contact mechanics and simplifying the geometry of the contact path. For a Hertzian stress of 5.6 GPa prior to the wear of the contact path, it was reduced by more than 35% with the initiation of the wear. The reduction of contact stress due to contact profile change resulted in it being more difficult to initiate fatigue failure.

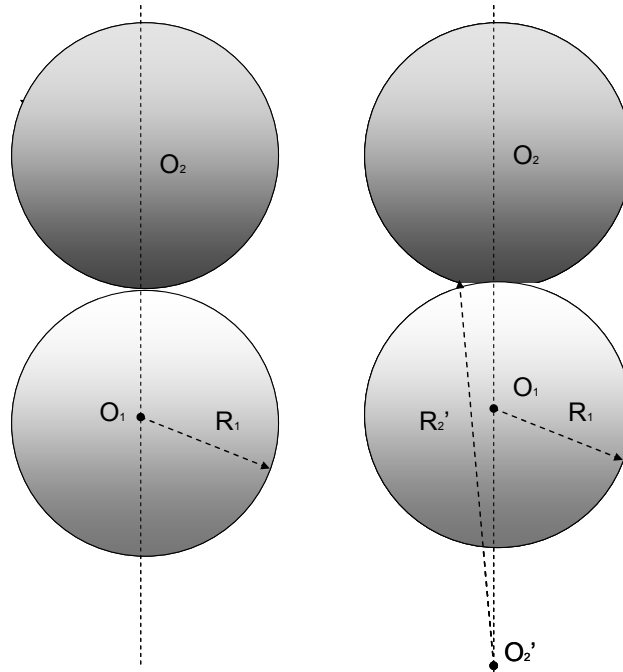


Figure 5-12: Contact geometry changed due to wear of Silicon Nitride

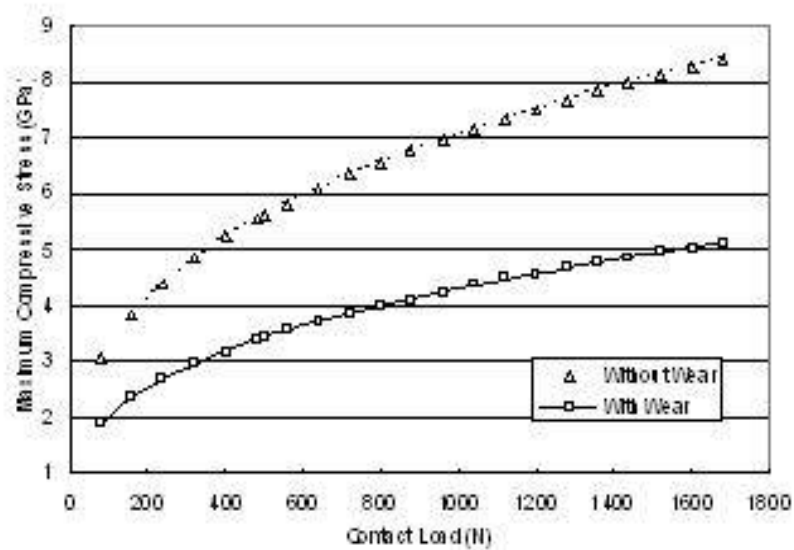
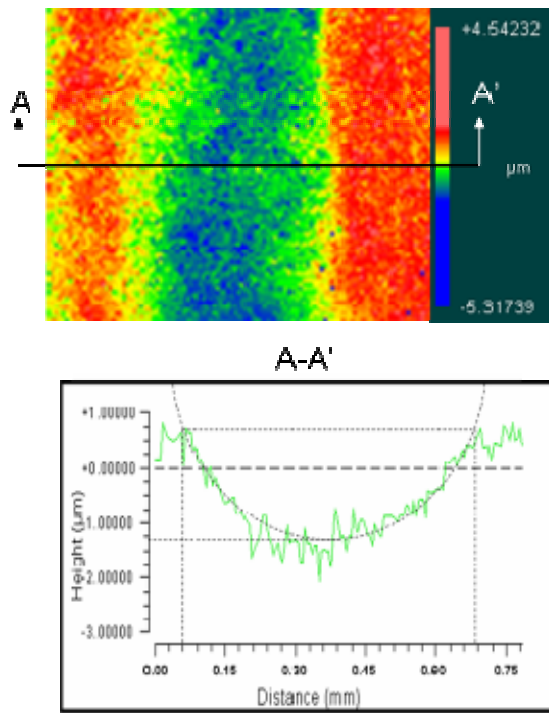


Figure 5-13: Contact stress reduction due to contact geometry change

As-machined Ceralloy 147-31N SRBSN rods and balls were tested on ball-on-rod and four-ball testers respectively. For all the tests, Castrol 75w90 transmission oil was selected as the lubricant due to the chemical compatibility, potential automotive application of SRBSN and the lubricant's relatively high viscosity to maintain a lubrication film to reduce the contact between Silicon Nitride surface asperity and the

steel ball surface. No spall failure was observed on either tester after 100 million stress cycles on all specimens with all surface finishing conditions. However, moderate wear was seen on the contact path on both rod and ball specimens. The surface profile of the contact path was examined by a Zygo optical interferometer. The results of rod specimens with coarse, fine and RCF-conventional surface-finishing conditions are shown in Figures 5-14, 5-15 and 5-16, respectively. By calculating the wear loss volume approximately, the ratio of volume loss of coarse, fine and RCF-conventional surface conditions was 1.5:1.3:1. There was a trend of decreasing wear volume loss from coarse, fine to RCF-conventional surface conditions on the RCF rod specimen.



**Figure 5-14: Contact path profile of RCF rod with coarse surface condition**

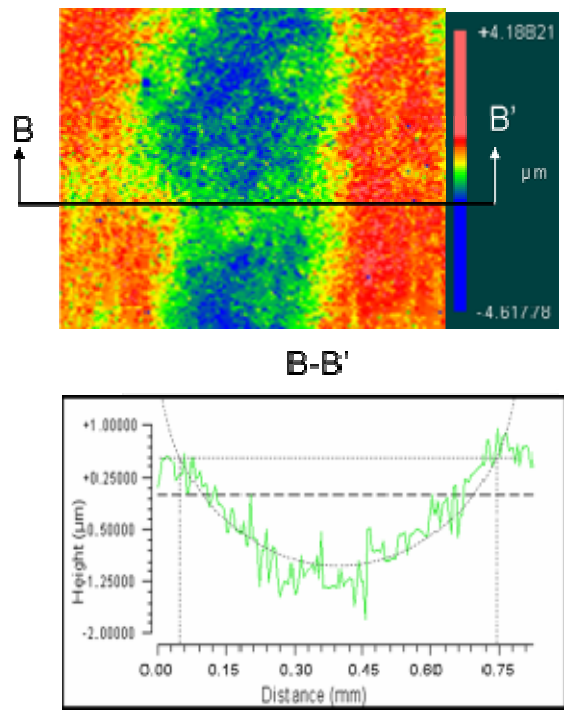


**Figure 5-15: Contact path profile of RCF rod with fine surface condition**

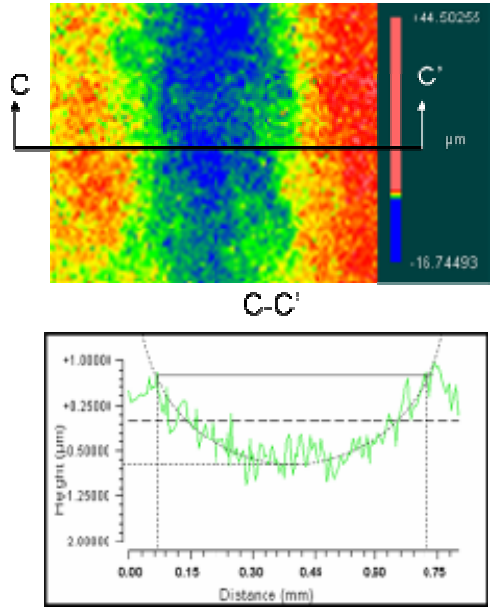


**Figure 5-16: Contact path profile of RCF rod with RCF-conventional surface condition**

The contact path profiles of the RCF ball with coarse, fine and RCF-conventional surface finishing conditions are shown in Figures 5-17, 5-18 and 5-19. In order to compare the wear volume loss, a cross section was taken in the middle of the contact path to acquire a 2-D profile. The 2-D contact profile of three specimens could be compared to form the basis of the wear volume loss comparison, and the result is shown in Figure 5-20. As shown in the figure, a trend of decreasing wear volumes from coarse to fine and RCF-conventional specimens was similar to the trend of rod specimens.

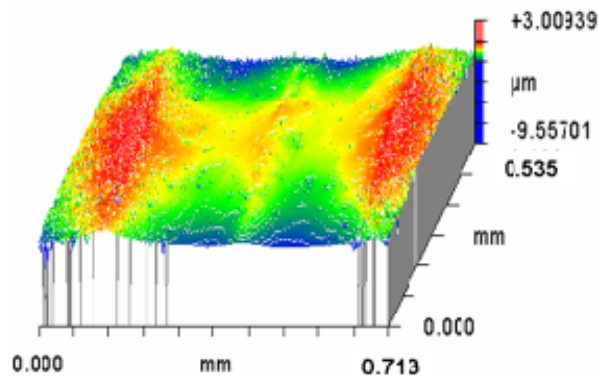


**Figure 5-17: Contact path profile of RCF ball with coarse surface condition**

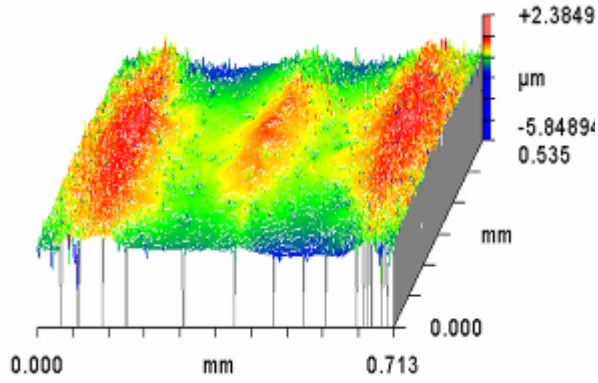


Figure 5-18: Contact path profile of RCF ball with fine surface condition.

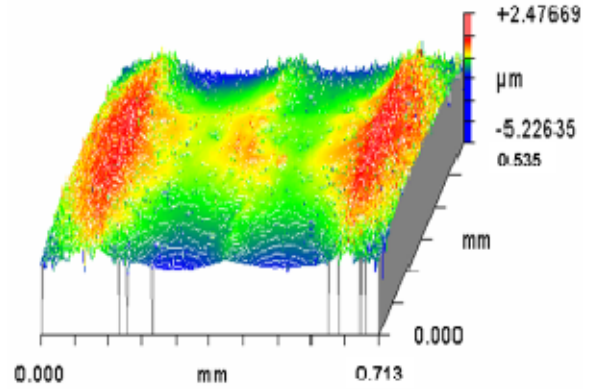


Figure 5-19: Contact path profile of RCF ball with RCF-conventional surface condition.

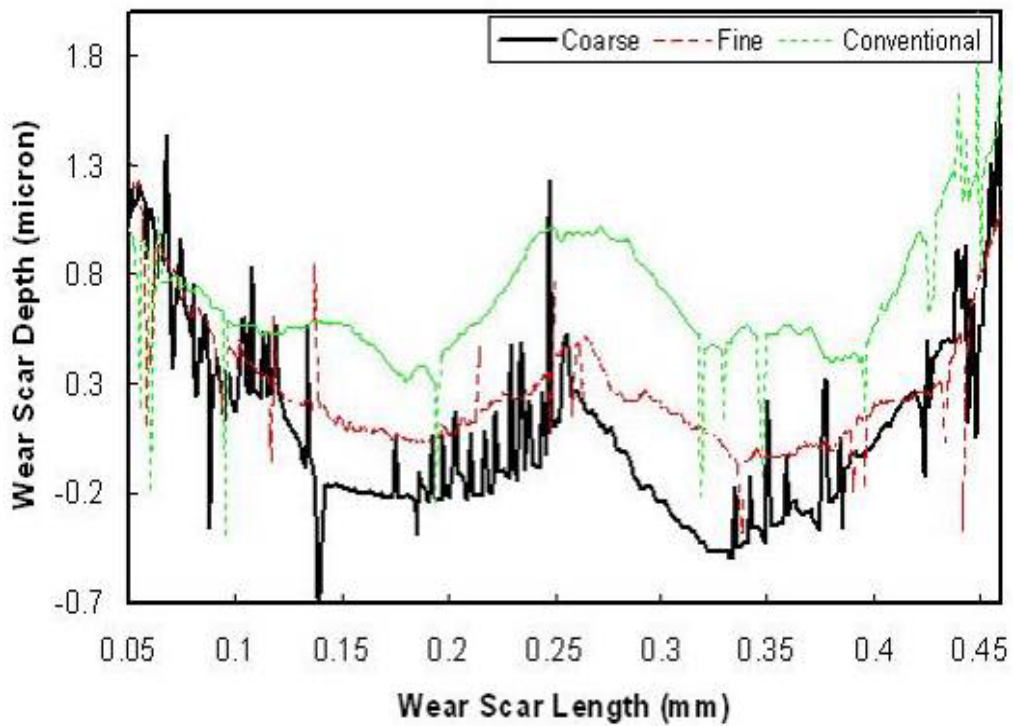


Figure 5-20: Wear volume loss comparison of three surface finishing conditions

## 5.3 Rolling Contact Fatigue

### 5.3.1 RCF Life of Lapped SRBSN Silicon Nitride

Two specimens from the in-house lapped SRBSN Silicon Nitride specimens were tested on the modified four-ball machine with 30 and 60 degree cracks created on their surface to investigate the RCF performance of bearing grade SRBSN. The artificial cracks were created using the technique described in Section 5.1.4. The surface profile of the 30 degree crack was examined using a Zygo interferometer, and the images are shown in Figure 5-21.

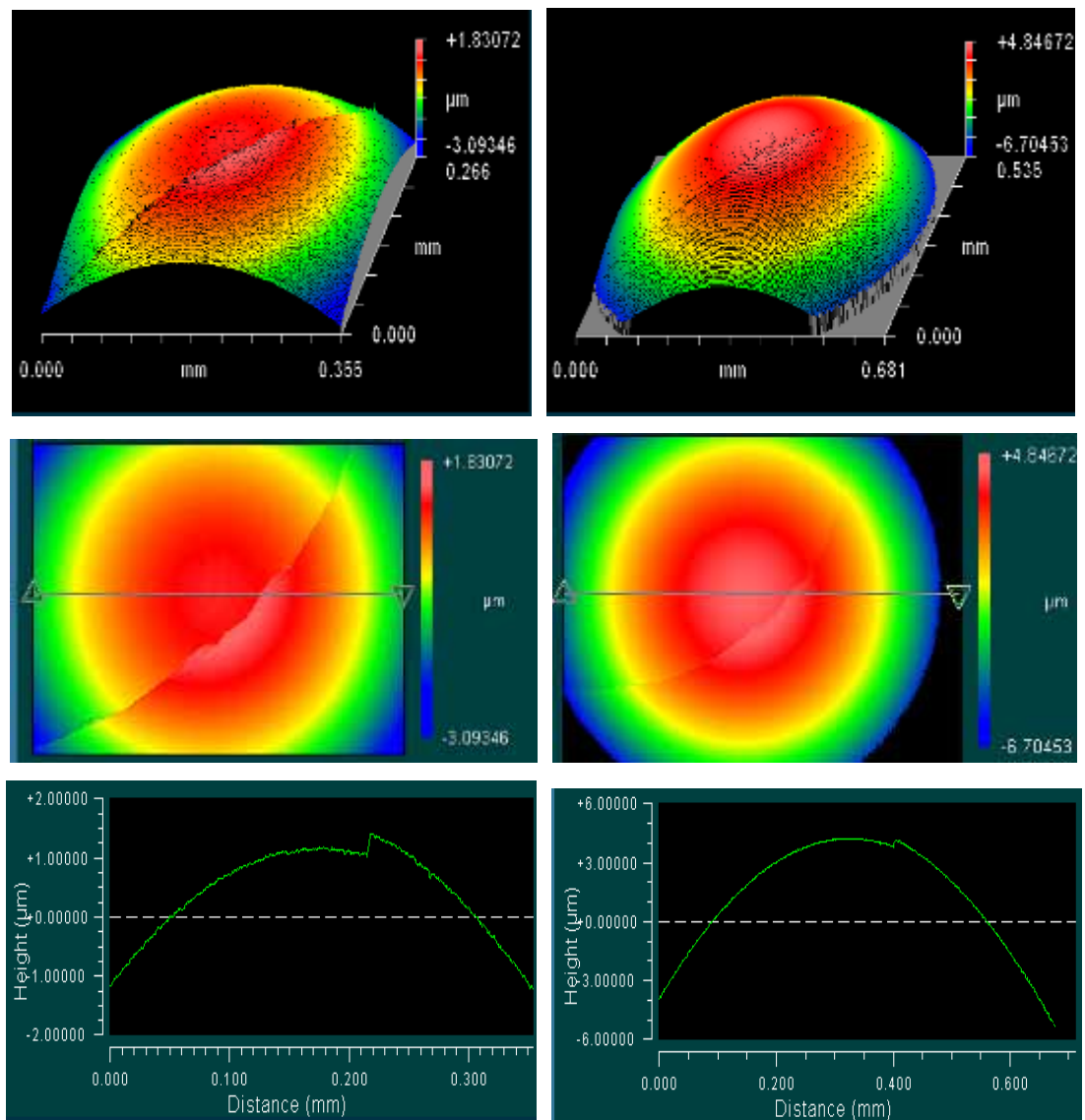
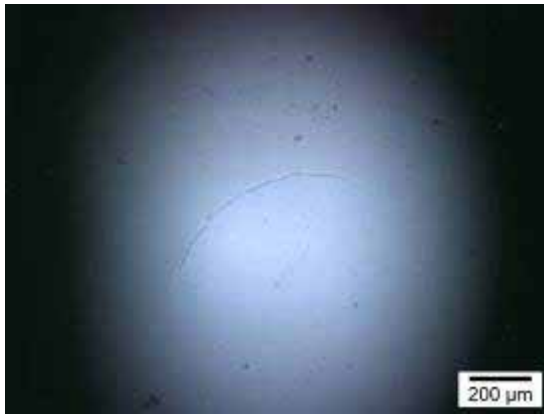


Figure 5-21: Profile of 30 degree crack seen on a Zygo interferometer

The 30 degree artificial cracks were positioned on the contact path with  $\beta=90$  degrees, and an RCF test was performed with 5.6 GPa nominal maximum Hertzian stress, 5000 rpm spindle speed and Castrol 75w90 lubricant. The deterioration and progression of the artificial crack is shown in Figures 5-23 to 5-26 below. The specimen failed at 130 minutes with the four-ball machine triggered by excessive vibration caused by the development of the spall.



**Figure 5-22: 30 degree artificial crack – 0 minutes.**



**Figure 5-23: 30 degree artificial crack – 0 minute**



**Figure 5-24: 30 degree crack after 31 minutes**



**Figure 5-25: 30 degree crack after 130 minutes**

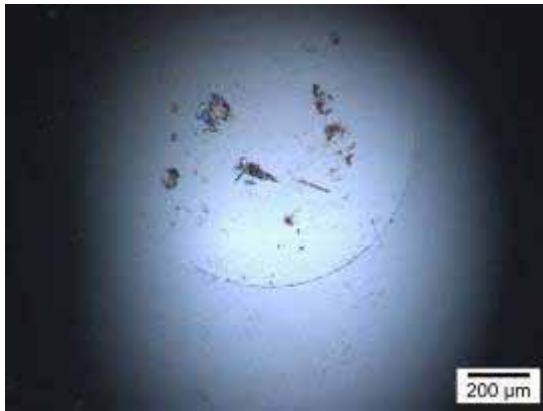


Figure 5-26: 60 degree crack – after 0 minutes



Figure 5-27: 60 degree crack – after 0 minutes

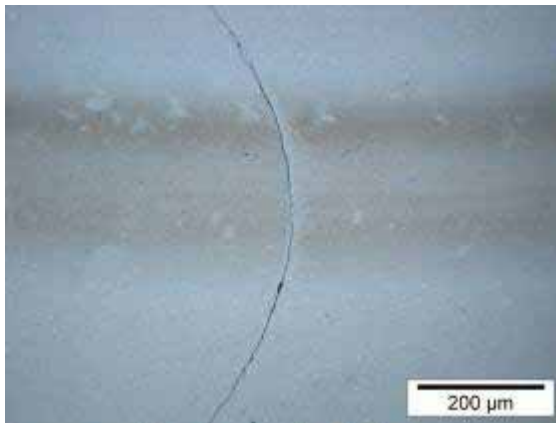


Figure 5-28: 60 degree crack – after 15 minutes.

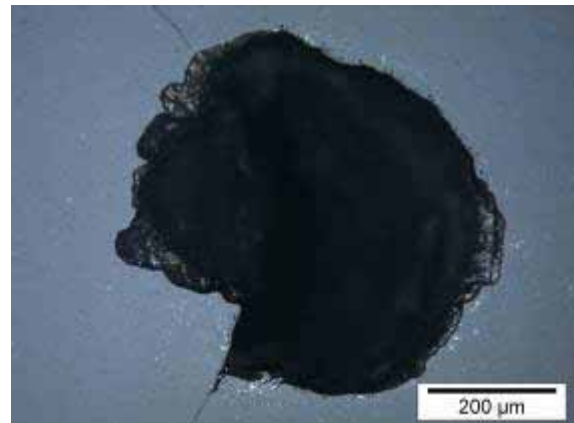


Figure 5-29: 60 degree crack - after 45 minutes

The RCF test was repeated with another SRBSN specimen which had a 60 degree artificial crack on the surface, as shown in Figure 5-26 to 5-27 above. The four ball machine setup was unchanged and the 60 degree crack positioned onto the contact path with  $\beta=90$  degrees. The machine was stopped after 15 minutes to examine the positioning of the crack as shown in Figure 5-28. The four-ball machine vibration sensor was triggered, and the machine was automatically stopped after 45 minutes running. Optical microscope examination showed that a fatigue spall had developed on the surface, as shown in Figure 5-29. The RCF testing of pre-cracked commercial grade SRBSN showed that they had similar fatigue lives compared with pre-cracked commercial grade HIPed Silicon Nitride (HIPed Silicon Nitride data for comparison is unpublished). However, it is inconclusive to say that commercial grade SRBSN is comparable with commercial grade

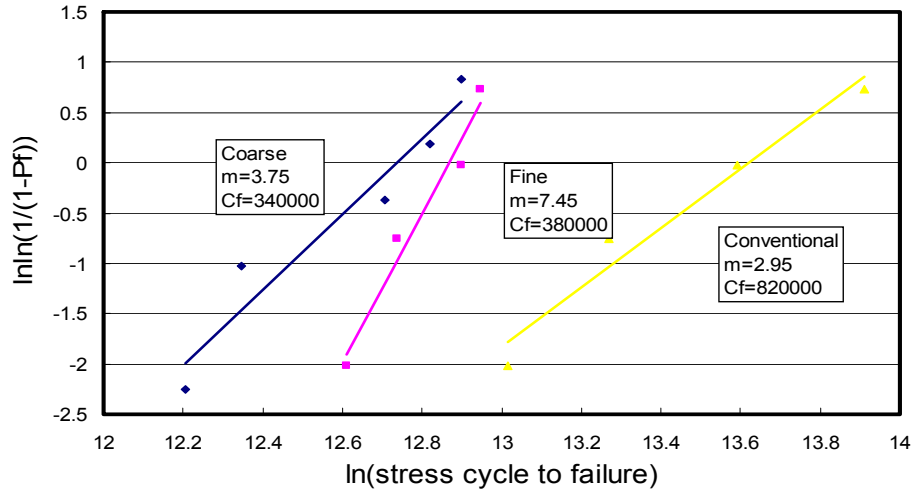
HIPed Silicon Nitride in terms of RCF performance. Comparing rolling contact fatigue developed through natural cracks can be more conclusive. This, however, it is not in the scope of this research.

### 5.3.2 RCF Life of Core Drilled SBRSN Silicon Nitride

Five balls in each batch of coarse, fine and RCF-conventional conditions were tested. For all the tests, Castrol 75w90 transmission oil was used as lubricant. The applied Hertzian contact stress between the upper ball and lower balls was 5.6 GPa, and the spindle speed was 5000 rpm, which resulted in 11250 stress cycles per minute. Their fatigue lifetimes relative to the positioning parameters are summarised in Table 5-2. Two specimens, Fine-05 and RCF-conventional-05, were not positioned accurately in the contact path, and these two specimens were excluded from the analysis. From the Weibull analysis results shown in Figure 5-30, we can see that RCF-conventional specimens show an extended lifetime compared with fine and coarse specimens with identical artificial cracks on the surface and cracks positioned in the contact path with the same positioning parameter.

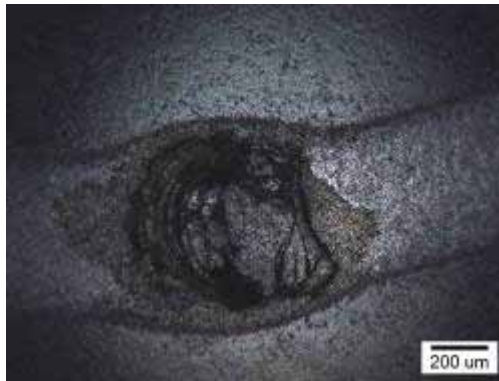
Specimen ID	Crack Position Parameter $\beta$	Crack Position Parameter $\delta$	Fatigue Life (No. of Stress cycles)
Coarse-01	90°	0	$2 \cdot 10^5$
Coarse-02	90°	0	$3.7 \cdot 10^5$
Coarse-03	90°	0	$2.3 \cdot 10^5$
Coarse-04	90°	0	$4 \cdot 10^5$
Coarse-05	90°	0	$3.3 \cdot 10^5$
Fine-01	90°	0	$4.1 \cdot 10^5$
Fine-02	90°	0	$3.0 \cdot 10^5$
Fine-03	90°	0	$4.2 \cdot 10^5$
Fine-04	90°	0	$3.4 \cdot 10^5$
Fine-05	90°	0.5a	$1.2 \cdot 10^7$
RCF-conventional-01	90°	0	$4.8 \cdot 10^5$
RCF-conventional-02	90°	0	$8 \cdot 10^5$
RCF-conventional-03	90°	0	$1.5 \cdot 10^6$
RCF-conventional-04	90°	0	$4.5 \cdot 10^5$
RCF-conventional-05	45°	0.5a	suspended

Table 5-2: RCF results of Ceralloy 147-31N SRBSN



**Figure 5-30: Weibull analysis of RCF test results of coarse, fine and RCF-conventional conditions.**

The rolling contact fatigue spall profiles of failed specimens are shown in Figures 5-31 to 5-44 for selected coarse, fine, and RCF-conventional specimens. All the specimens exhibited the same feature with spalling developed from the artificial crack.



**Figure 5-31: Coarse-01**



**Figure 5-32: Coarse-02**

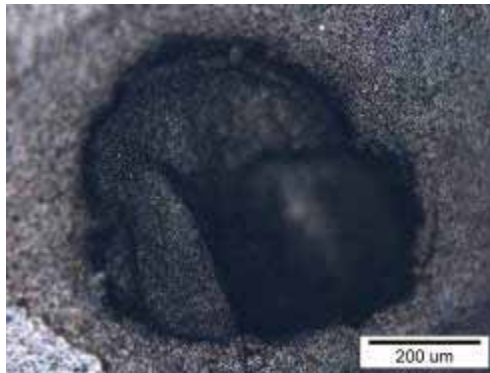


**Figure 5-33: Coarse-03**



**Figure 5-34: Coarse-05**

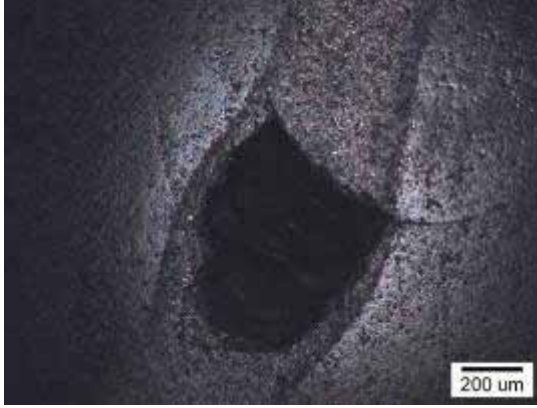


**Figure 5-35: Fine 01**



**Figure 5-36: Fine 03**

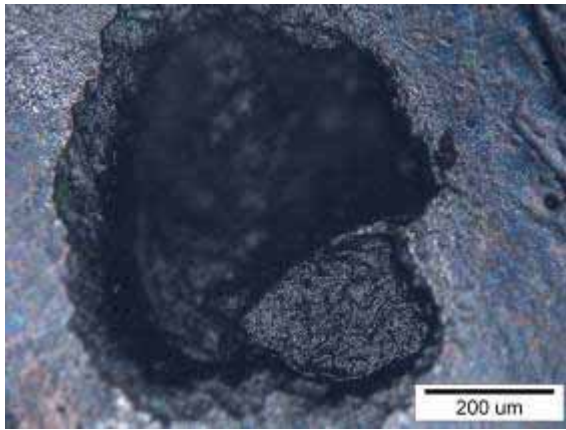


**Figure 5-37: Fine-04**



**Figure 5-38: Fine-05**

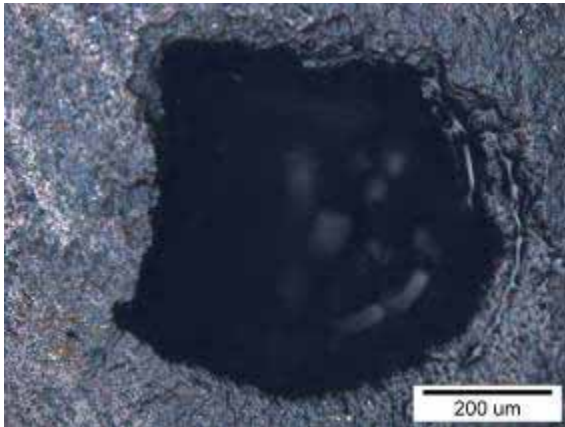


**Figure 5-39: RCF-Conventional-01**

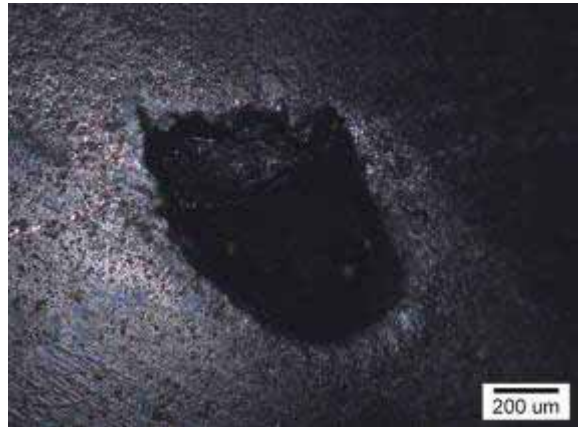


**Figure 5-40: RCF-Conventional-03**



**Figure 5-41: RCF-Conventional-04**

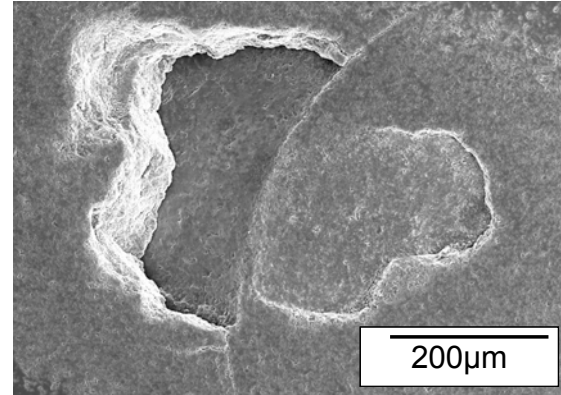


**Figure 5-42: RCF-Conventional-02**

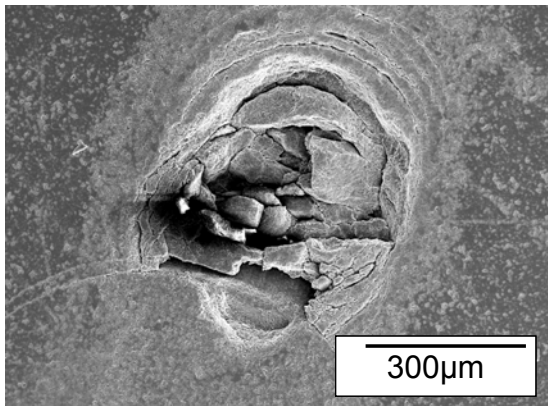


**Figure 5-43: Fine-02**

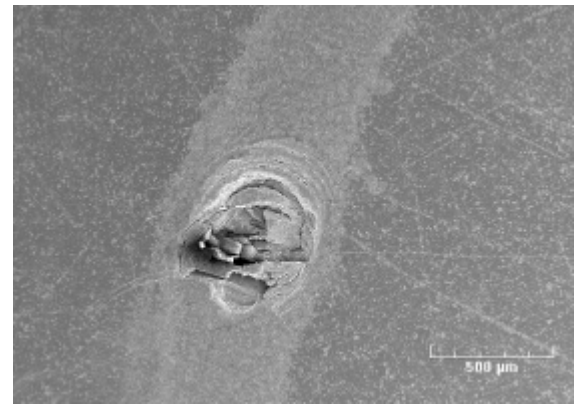


**Figure 5-44: Fine-02**

The coarse specimen had the worst RCF performance, with characteristic stress cycles to failure  $C_f = 3.4 \cdot 10^5$ . The characteristic stress cycles to failure of RCF-conventional specimens was  $8.2 \cdot 10^5$ , which was significantly better than that of coarse and fine specimens. However, in order to improve the reliability of RCF results, more tests should be run to give a statistically confident conclusion. Although there are variations on the geometry of the spalls from specimen to specimen, there is evidence that secondary cracks are developed in the spalling process.

## 5.4 Effect of Lubricant Viscosity

The RCF tests carried out on four-ball and ball-on-rod testers were lubricated, and the viscosity of lubricants can have an effect on the RCF life of Silicon Nitride. Given Silicon Nitride's existing and potential application in the automotive industry, three lubricants were selected to study the viscosity effect on RCF performance of Silicon Nitride after consultation with a lubricant specialist in the driveline department of a major lubricant manufacturer. The test temperature was controlled at ambient and elevated level of 100 °C, which is the approximate bulk engine running temperature. The properties of the lubricants are shown in Table 5-3.

Lubricant	Chemical	Type	Flash Point	Pour Point	Density at 15C(kg/m <sup>3</sup> )	Kinematic Viscosity (cSt)	
						40	100
002A	Poly-alpha-olefin (PAO)	Automotive Fluid	256	-60	847	53.8	8.98
003A	Paraffinic Oil with PAO 10-20 Percent	Automotive Fluid	208	-	837	64	11.8
004A	Paraffinic Oil with Additives	Automotive Fluid	220	-	867	79	12.3

**Table 5-3: Properties of three selected lubricants**

The absolute viscosity of the lubricant can be calculated using the Equation 5-5, where  $\eta$  (cP,  $1 \text{ N}\cdot\text{s}/\text{m}^2 = 1000 \text{ cP}$ ) is the absolute viscosity,  $t_m$  is the temperature in celcius. The absolute viscosity can be calculated from kinematic viscosity  $\eta_k$ , where  $\eta_k = \eta / \text{density}$ .  $S_0$  and  $G_0$  are dimensionless constants. The absolute viscosities of three lubricants are derived in Appendix 7.7. The temperature dependency of lubricant absolute viscosity is shown in Figure 5-45.

$$\log(\log \eta + 1.200) = -S_0 \log\left(1 + \frac{t_m}{135}\right) + \log G_0 \quad (\text{Eq. 5-5})$$

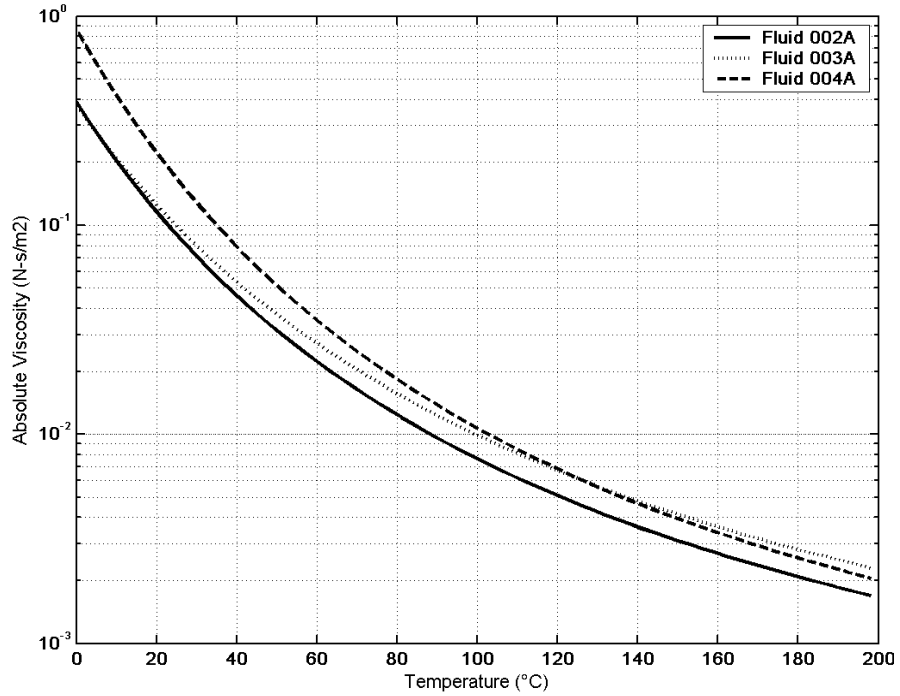


Figure 5-45: Relationship between absolute viscosity and temperature for three lubricants

The typical temperature profile of ceramic and steel ball contact on a four-ball machine is shown in Figure 5-46. For tests carried out at ambient temperature, the test chamber temperature rose slowly over time and stabilised at around 40 degrees after 100 minutes.

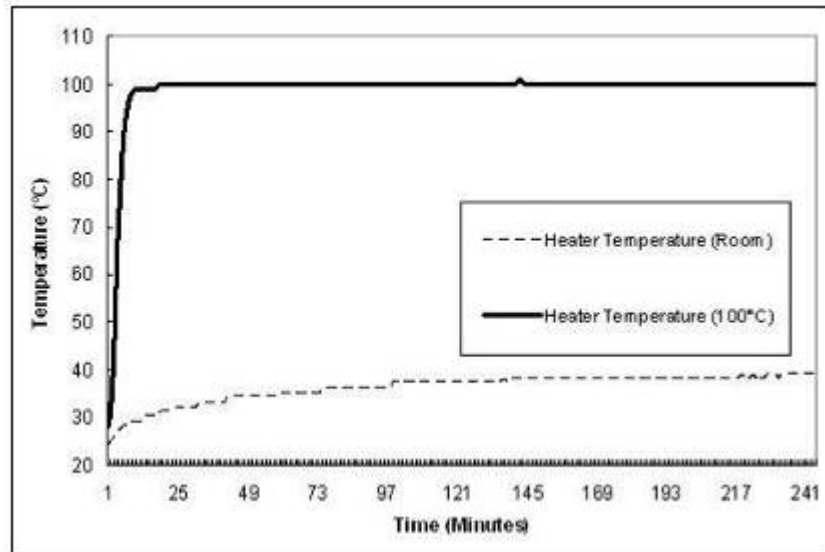


Figure 5-46: Temperature profile of four-ball machine at room temperature and elevated temperature

The pressure viscosity coefficients of the three selected lubricants were derived from data based on the chemical composition of the lubricants (Jones 1975), which is shown in Table 5-4. By using Eqs. 5-6 and 5-7, the pressure viscosity relationship can be derived. Figures 5-47 and 5-48 show the pressure-viscosity relationship for lubricants 002A, 003A and 004A at fixed temperatures of 40 degrees and 100 degrees.

Lubricant	Chemical	Pressure Viscosity Coefficient				
		38 °C	60 °C	80 °C	100 °C	150 °C
002A	Poly-alpha-olefin (PAO)	-	1.31	1.26	1.22	-
003A	Paraffinic Oil with PAO 10-20 Percent	1.88	-	-	1.51	1.19
004A	Paraffinic Oil with Additives	1.89	-	-	1.46	1.19

Table 5-4: Pressure viscosity coefficient of the lubricants

$$Z_1 = \frac{\xi}{5.1 \times 10^{-9} (\ln \eta_0 + 9.67)} \quad (\text{Eq. 5-6})$$

$$\log \eta + 1.200 = (\log \eta_0 + 1.200) \left(1 + \frac{P}{2 * 98}\right)^{Z_1} \quad (\text{Eq. 5-7})$$

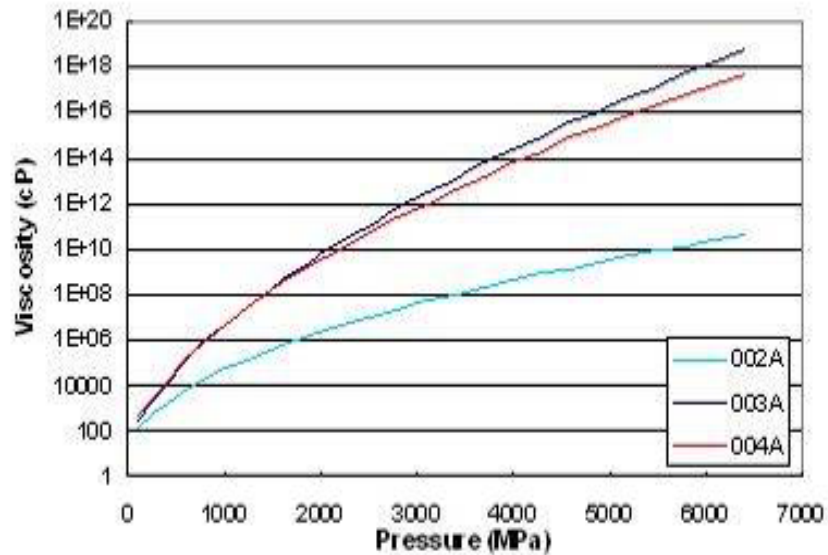


Figure 5-47: Pressure-viscosity relationship at 40 degrees

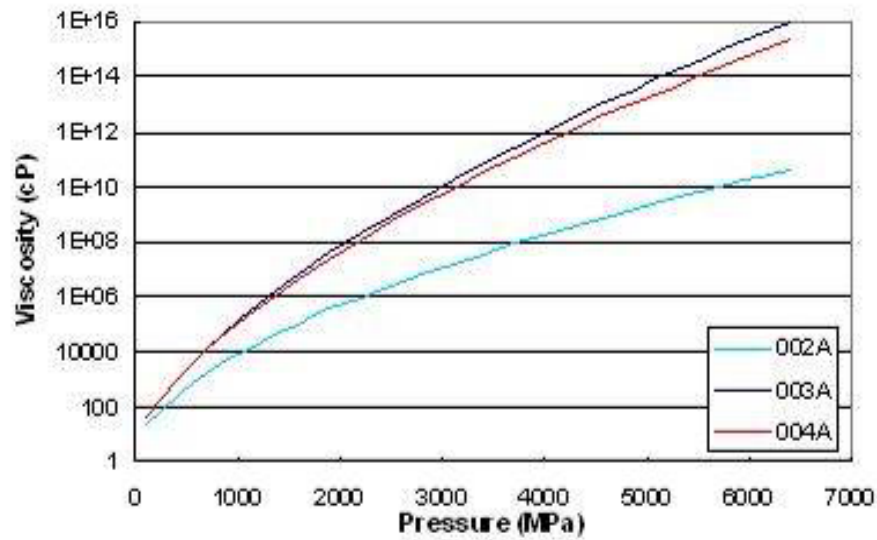


Figure 5-48: Pressure-viscosity relationship at 100 degrees

Six SRBSN ball specimens which were finished on the eccentric lapping machine were tested on the modified four ball machine to study the lubricant viscosity effect on the RCF performance of commercial grade SRBSN. Three lubricants were tested at ambient and elevated temperatures of 100 degrees respectively. The SRBSN ball specimens were pre-cracked with 30 degree impact cracks on the surface to accelerate the failure. The contact stress of the Silicon Nitride and steel ball contact was controlled at 5.6 GPa, and spindle speed was 5000 rpm. The test matrix, crack positioning parameters and RCF lives of six SRBSN specimens are summarised in Table 5-5.

Specimen ID	Temperature	Lubricant	Crack Position Parameter $\beta$	Crack Position Parameter $\delta$	Fatigue Life (No. of Stress cycles)
L-SRB-01	ambient	002A	90°	0	1.4*10 <sup>6</sup>
L-SRB-02	ambient	003A	90°	0	1.8*10 <sup>6</sup>
L-SRB-03	ambient	004A	90°	0	1.2*10 <sup>6</sup>
L-SRB-04	100	002A	90°	0	0.9*10 <sup>6</sup>
L-SRB-05	100	003A	90°	0	1.2*10 <sup>6</sup>
L-SRB-06	100	004A	90°	0	1.5*10 <sup>6</sup>

Table 5-5: RCF performance of lapped SRBSN balls studied on modified four-ball machine with three different lubricants

As shown in the RCF test results, at ambient temperature, the SRBSN ball RCF specimen lubricated with 003A lubricant had the best RCF performance, whereas 004A lubricant lubricated RCF test had the worst performance. At 100 °C, 004A lubricant reversed the trend to have the best RCF performance among three candidate lubricants, and 002A lubricated SRBSN ball specimen had the worst RCF life. For the test carried out at ambient temperature, the test chamber temperature stabilised at 40 °C after test start, so the in running lubricant temperature was the same as the test chamber temperature which was around 40 °C. At both of 40 °C and 100 °C, with 5.6 GPa contact stress, 003A lubricant had the highest pressure viscosity (as shown in Figures 5-47 and 5-48), with lubricant 002A having the lowest pressure viscosity. However, the RCF test results did not show any correlation between the RCF lives of the SRBSN specimens and their lubricant viscosities. The RCF life of the specimens is more likely to be driven by the surface/subsurface damage introduced during the artificial crack creation process. The scatter of the test results is also more likely to reflect the variation of artificial crack creation and positioning among six SRBSN specimens, which is more significant in terms of their impact on RCF performance than the viscosity variation. As a consequence, the lubricant viscosity effect on RCF performance of SRBSN is inconclusive from this study.

# CHAPTER 6: DISCUSSION AND CONCLUSIONS

## 6.1 Surface Strength, Residual Stress and Machining Process of Silicon Nitride

Flexure strength testing of Silicon Nitride reveals that there are variations of surface strength among SRBSN specimens with different surface finishing conditions. There are also variations in surface strength among three commercial grades of HIPed Silicon Nitride, as described in Section 3.2. The variation of surface strength of Silicon Nitride material is believed to be the effect of a combination of material microstructure, residual stress and machining process. The study of Silicon Nitride microstructure (see Section 2.1) through plasma etching and chemical etching reveals that all four specimens show needle-like grains interlocking with each other, with the length of the grain varying between 4 microns to 10 microns. The effect of microstructure on the surface strength of Silicon Nitride is complicated to quantify and is beyond the scope of the research presented in this thesis. However, the effect of residual stress and machining has been studied.

In terms of SRBSN, as discussed in Section 4.2, RCF-conventionally machined specimens have the highest compressive residual stress values among specimens with the three different machining conditions. The coarsely machined specimens have the lowest compressive residual stress values. RCF-conventionally machined specimens, with a combination of best surface finishing process, i.e. the best surface and subsurface quality and highest compressive residual stress, reveals the highest surface strength through half-rod flexure strength testing and C-Sphere flexure strength testing.

Although the study shows that a better surface finishing gives better surface strength of SRBSN, the surface finishing of SRBSN contributes up to 70% of the overall cost of a

Silicon Nitride component. A better surface quality does introduce extra cost of machining in the form of more expensive abrasives, and longer machining hours.

## 6.2 Surface Strength and Rolling Contact Fatigue

The C-Sphere and RCF tests reveal the same trend of increasing strength and fatigue life of coarse, fine and RCF-conventional specimens. This correlation can be explained by the analysis of the stress field of the C-Sphere specimen and four-ball contact. The failure of the C-Sphere specimen is perceived to be micro-crack propagation when the outer fibre is subject to tensile stress. The tensile stress field of the outer fibre was previously shown in Figure 3-9. During the specimen machining process, coarse specimens are the most aggressively machined, which results in a higher density and greater depth of induced micro-cracks. As described earlier, the size of the flaw where fracture initiates, determines the strength of the C-Sphere. For the coarse condition, there is a higher probability that deeper strength-limiting flaws (micro-cracks) are located at the maximum tensile stress area, and the size of the flaw causes a weaker strength in the coarse C-Sphere specimen. In the modified four-ball test, the upper Silicon Nitride ball is subject to Hertzian contact against the contact ball. For a perfect Silicon Nitride ball without any surface cracks (natural or artificial) positioned in the contact path, the maximum tensile stress generated on the surface due to Hertzian contact is not high enough to initiate a crack. As a result, the RCF life for a perfect Silicon Nitride ball is very long, and it does not normally fail within a reasonable testing time (100 million stress cycles). However, for a pre-cracked Silicon Nitride ball, due to the existence of an artificial crack, the stress field on the surface is changed, which is explained in Figure 6-1. There is a gap existing between the two crack edges. For the type of artificial cracks created in the RCF tests in this study, as described earlier, the width of the gap is measured at 2.5 microns for a 60 degree crack. As a result of the gap, when the section of the ball surface to the left of the crack is subject to contact stress, it creates a bending force which generates a tensile stress field on the specimen surface. Together with the stress field created due to Hertzian contact, when the overall tensile stress on the surface reaches a threshold, the micro-cracks will propagate to form a secondary crack on the surface. Due to the existence of a secondary crack, a tertiary crack was created under a similar scenario. This crack pattern

is then repeated as illustrated in Figure 6-2.

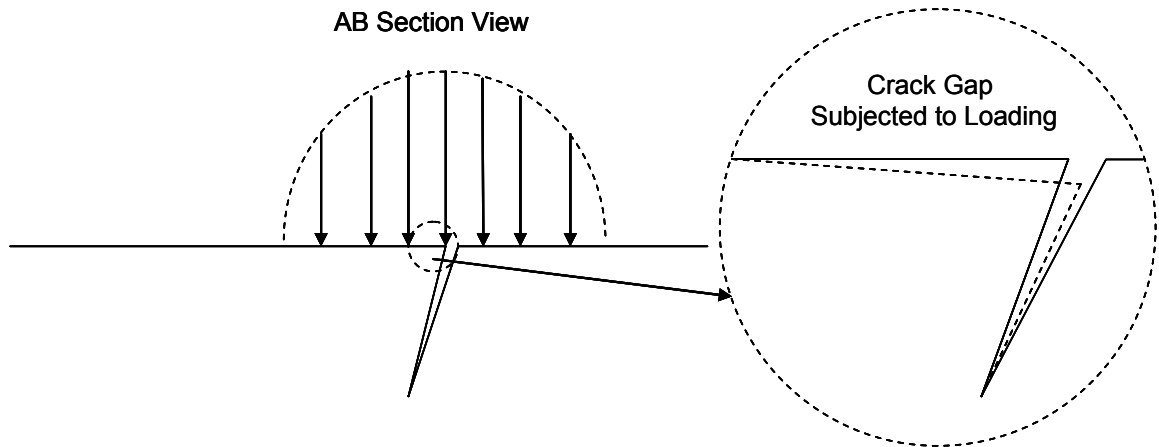


Figure 6-1: Secondary crack creation mechanism

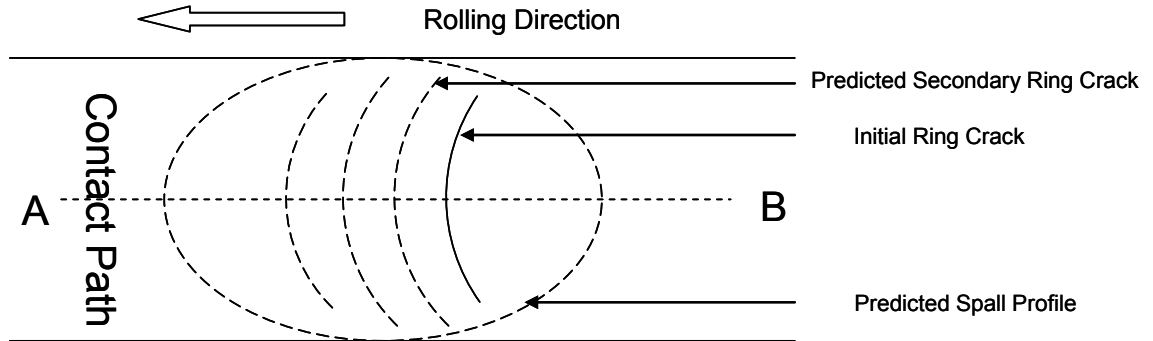
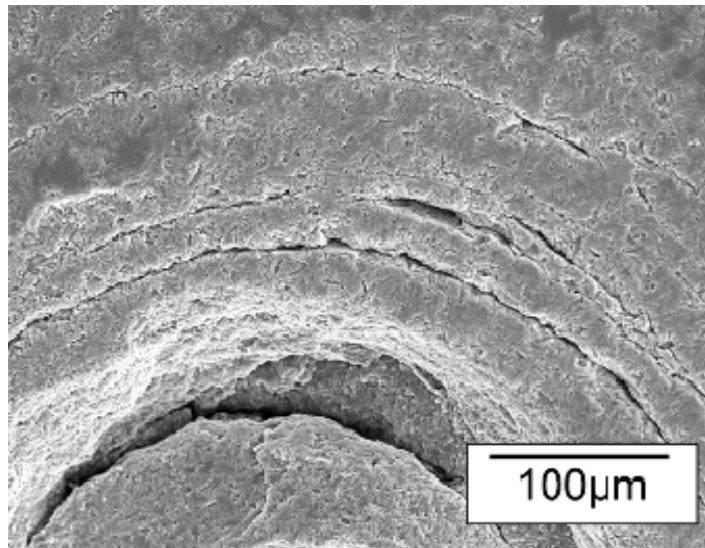
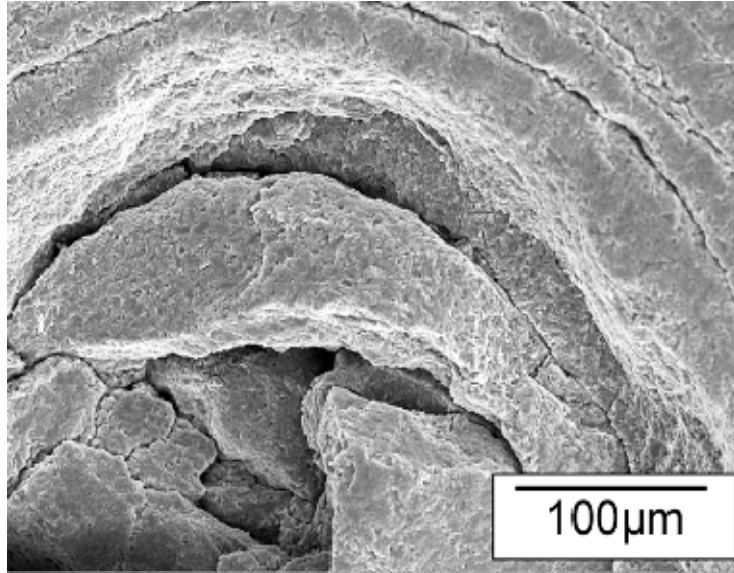


Figure 6-2: Spall formation mechanism



(a)



(b)

**Figure 6-3: SEM images of secondary crack creation**

The secondary and tertiary cracks propagate to meet the original crack thus forming a spall type of failure. Figure 6-3 shows the secondary cracks of Fine-02 specimen and associated spall failure. The mechanism of forming a secondary crack on the surface in a modified four-ball test is similar to micro-crack propagation in a C-Sphere test when it is interpreted by tensile stress on the surface. This explains the correlation between RCF results and C-Sphere results. The boundary element modelling of the artificial crack under Hertzian pressure was carried out by Wang and Hadfield (Wang and Hadfield 2002; Wang and Hadfield 2003), and the simulation results show the same conclusion.

### 6.3 Conclusions

The research presented in this thesis studies the rolling contact fatigue performance of Silicon Nitride through quantifying the surface finishing conditions and surface strength of Silicon Nitride. The main conclusions from the thesis are listed below.

- SRBSN has a rod-like interlocking grain structure, which is similar to commercial HIPed Silicon Nitride. However it has a much higher finishing rate than HIPed Silicon Nitride as was concluded through the study of the finishing process on an eccentric lapping machine. This conclusion is significant as the finishing of Silicon

Nitride contributes up to 70% of the Silicon Nitride component cost. The higher finishing rate makes SRBSN economically more attractive to bearing and other rolling component manufacturers.

- The study of residual stress through X-ray diffraction reveals that there is an increase in compressive residual stress by improving the surface finishing quality from coarse, fine to RCF-conventional surface finishing conditions. The compressive residual stress was introduced through the Silicon Nitride sintering and reaction-bonding process, and aggressive machining acts as a mechanism to reduce the compressive residual stress. As compressive residual stress is beneficial to RCF of Silicon Nitride, a better/less aggressive surface finishing is considered to improve RCF life from residual stress perspective.
- A combination of higher compressive residual stress and better surface quality contributes to a better surface strength of RCF-conventionally machined SRBSN through the quantification of the C-Sphere and half-rod tests.
- The most significant contribution of this study is to set up a link between the surface strength of SRBSN and the RCF performance of pre-cracked SRBSN, with the RCF-conventionally machined specimens showing the best surface strength and the longest RCF life. As RCF testing is normally lengthy and time-consuming, the surface strength of Silicon Nitride specimens can be used as a preliminary qualification technique to screen out the ‘weaker’ specimens prior to the start of the RCF testing. It is a cost-effective and efficient way to evaluate the potential RCF performance of candidate material.
- The effect of lubricant viscosity on RCF of SRBSN is studied. Three type of lubricants were used to carry out the RCF testing, however, it was concluded that the lubricant viscosity do not have a significant impact on the RCF performance of SRBSN.

## 6.4 Future Works

C-Sphere methodology for quantifying surface quality of Silicon Nitride spheres for use within rolling element bearings has potential for bearing manufacturers. More experimental information is required to assess the sensitivity of dimensional tolerances

on surface strength. In addition the modelling of surface and subsurface defects such as ring, cone and star types needs to be assessed and related to experimental information.

The effect of finishing rate and methodology does influence the fatigue mode and performance of Silicon Nitride rolling elements. Additional experimental information is required to assess the influence of coarse machining on defect fatigue durability and lubricant viscosity needs additional understanding.

# APPENDIX

## 7.1 Plasma Etching

The plasma etching process was carried out in the ORNL plasma etching machine shown in Figure 7-1. The machine is made up of a ventilation system, plasma etching chamber, vacuum pump and gas supply.



**Figure 7-1: Plasma etching machine**

The procedure followed was to put the vacuum button on the off position on the control panel as shown in Figure 7-2 in order to let the air in and reduce the plasma etching chamber pressure to ambient. The specimen was placed on the plastic holder and evacuated the chamber to 20 mTorr. The mixed gas valve was turned to and let the vacuum go back to around 220 mTorr. “Tuning” and “level” on the chamber control panel was adjusted until to make the indicator pointed “4”, and a purple light appeared, as shown in Figure 7-3. This indicated the start of the plasma etching process. The specimen was kept in the chamber for around 4 minutes and the gas valve then turned off. With the

vacuum button in the off position on the control panel the chamber pressure was returned to ambient. The specimen was removed and the chamber evacuated.



**Figure 7-2: Plasma etching machine control panel**

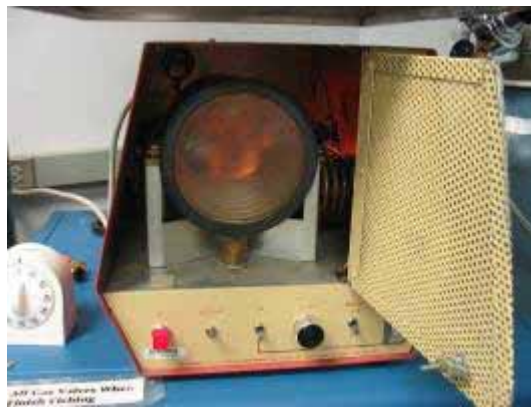


**Figure 7-3: Plasma etching chamber**

## 7.2 Half Rod Optical Fractography

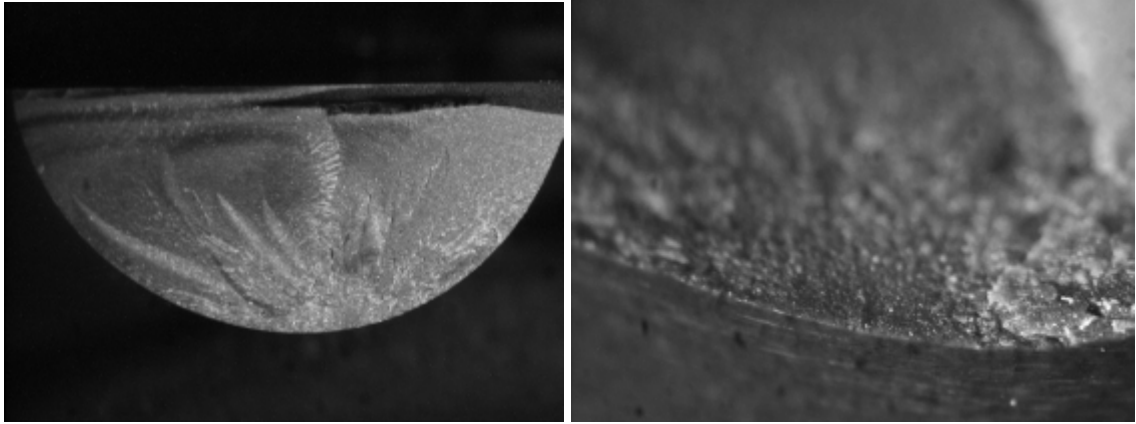


**Figure 7-4: Half RCF rod coarse 01**

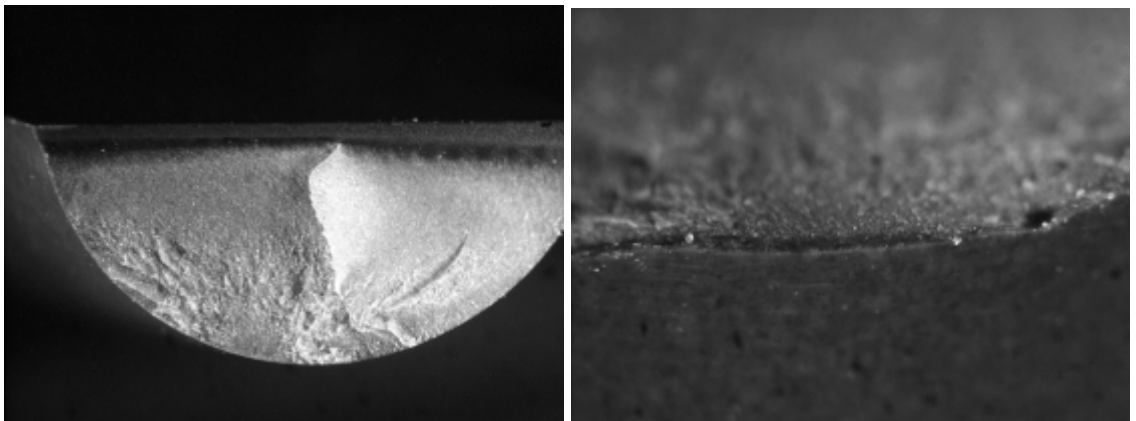


**Figure 7-5: Half RCF rod coarse 02**

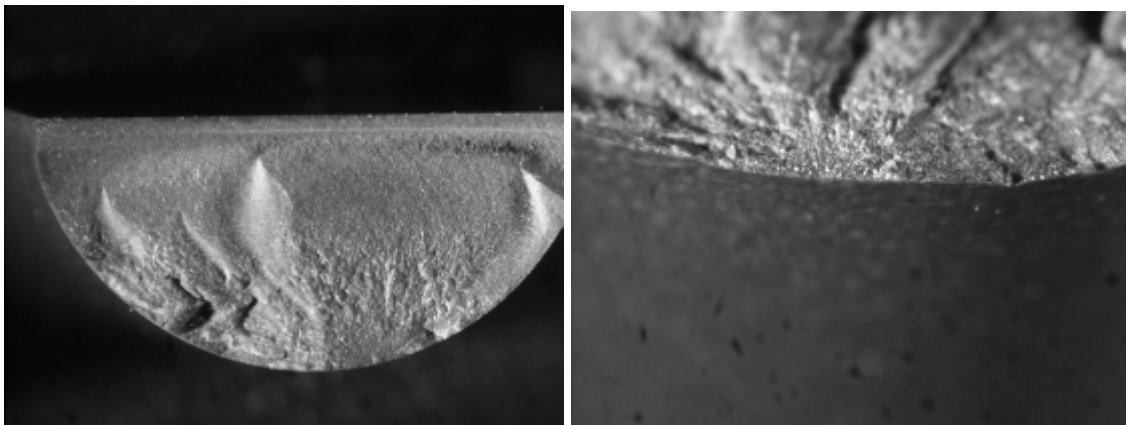


**Figure 7-6: Half RCF rod coarse 03**

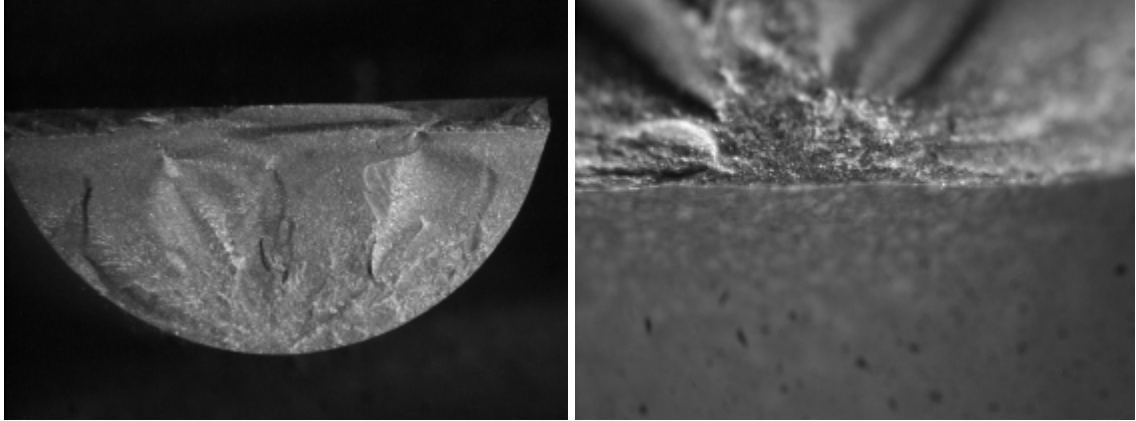


**Figure 7-7: Half RCF rod coarse 04**

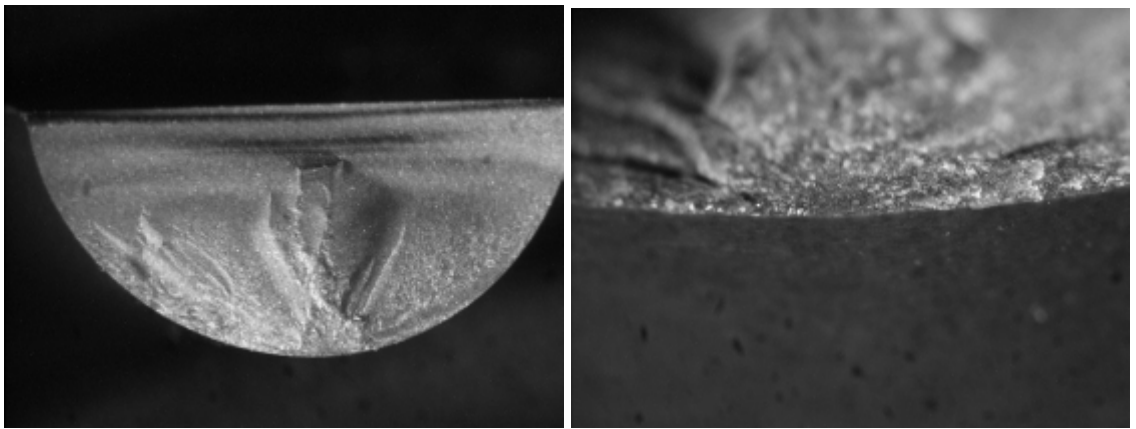


**Figure 7-8: Half RCF rod coarse 05**

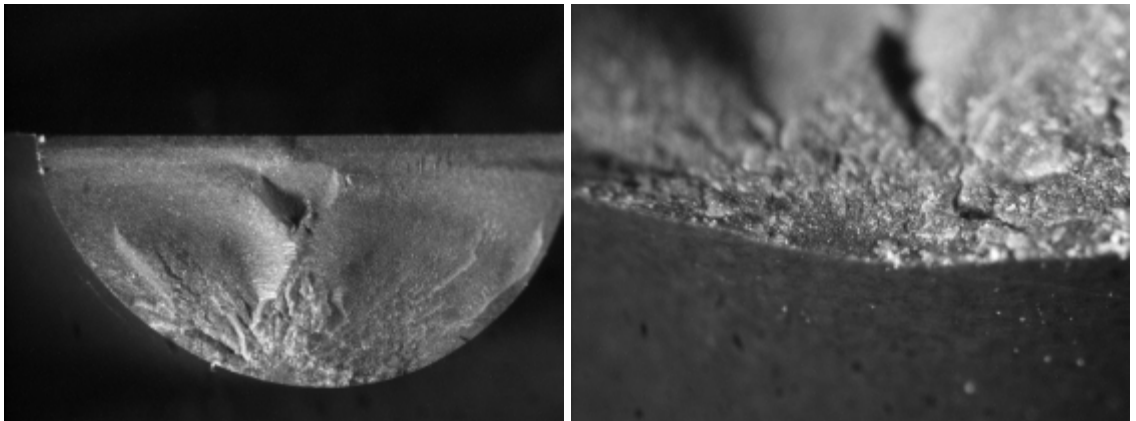


**Figure 7-9: Half RCF rod coarse 06**

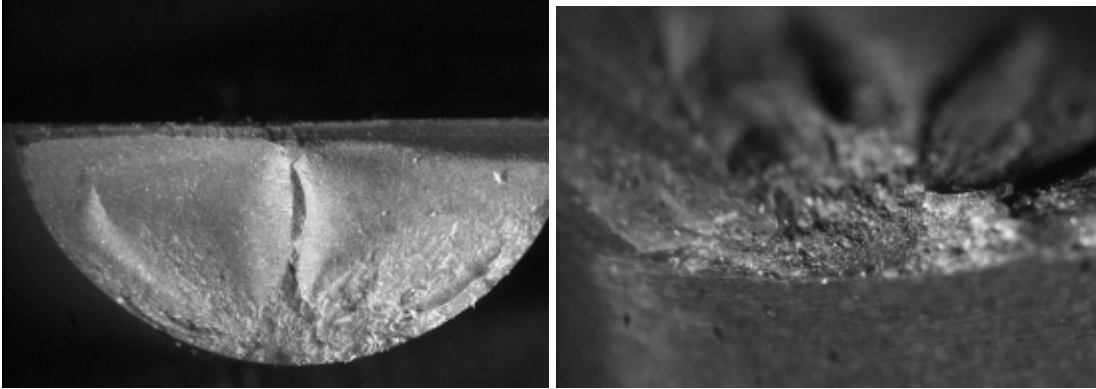


**Figure 7-10: Half RCF rod coarse 07**

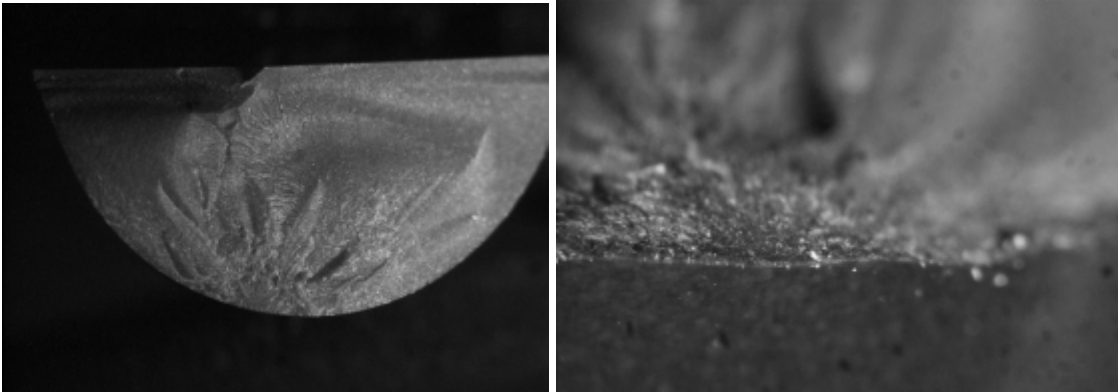


**Figure 7-11: Half RCF rod coarse 08**

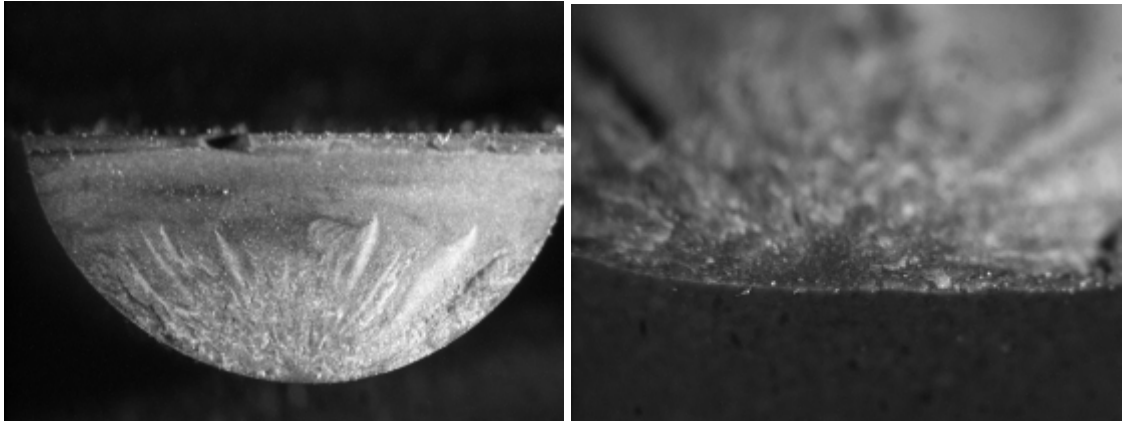


**Figure 7-12: Half RCF rod fine 01**

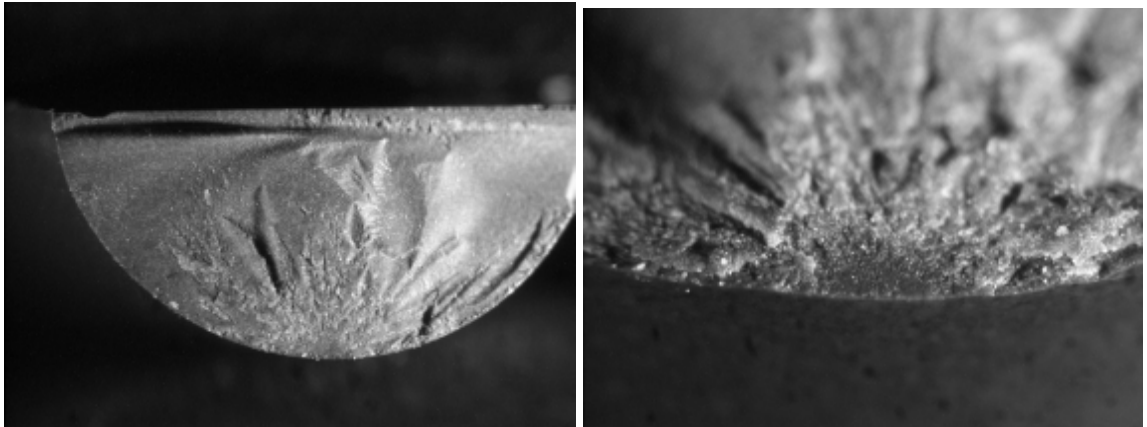


**Figure 7-13: Half RCF rod fine 02**

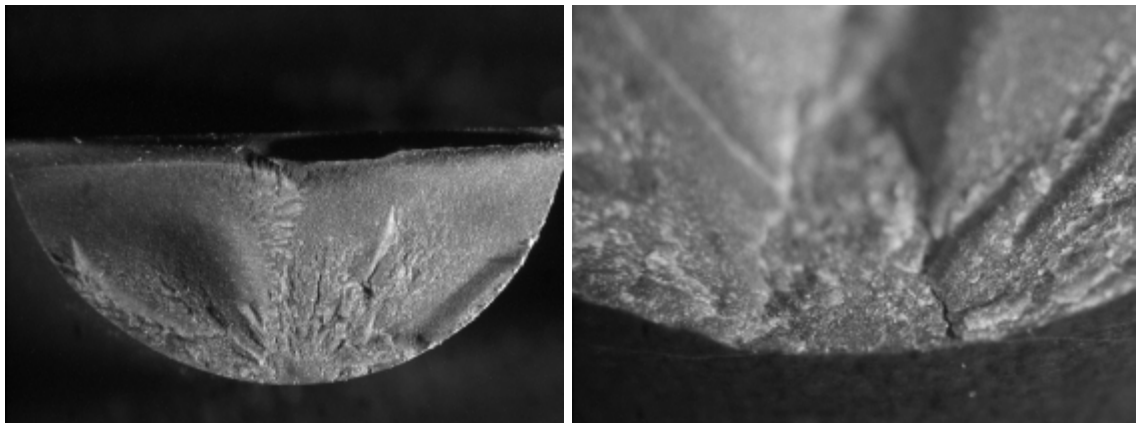


**Figure 7-14: Half RCF rod fine 03**

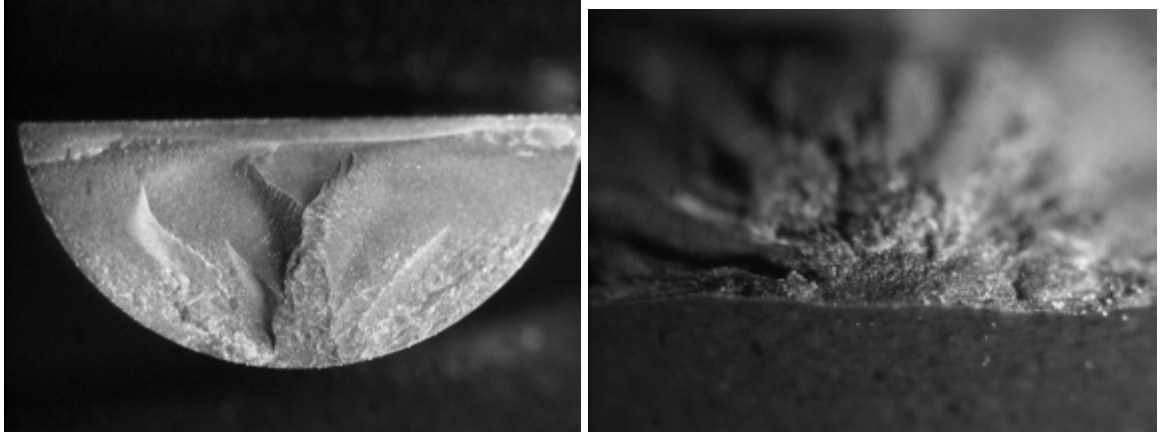


**Figure 7-15: Half RCF rod fine 04**

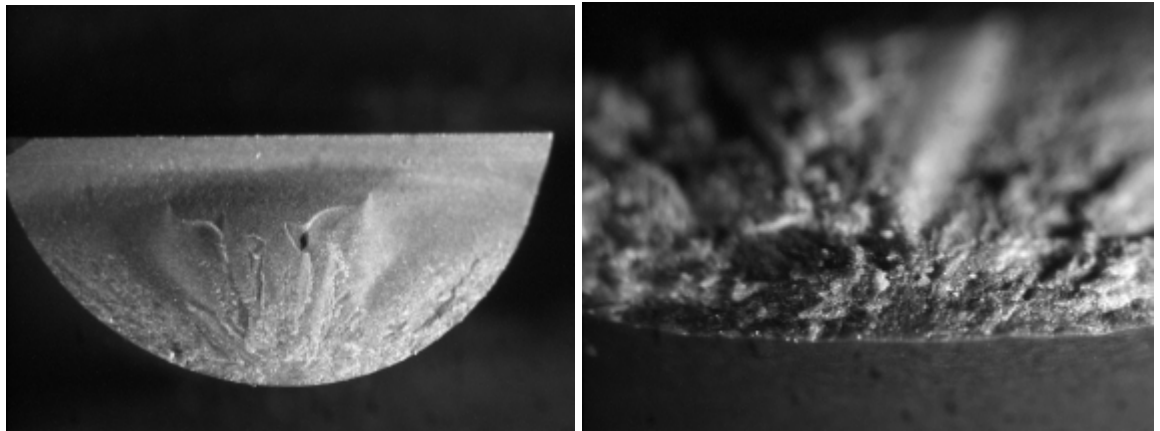


**Figure 7-16: Half RCF rod fine 05**

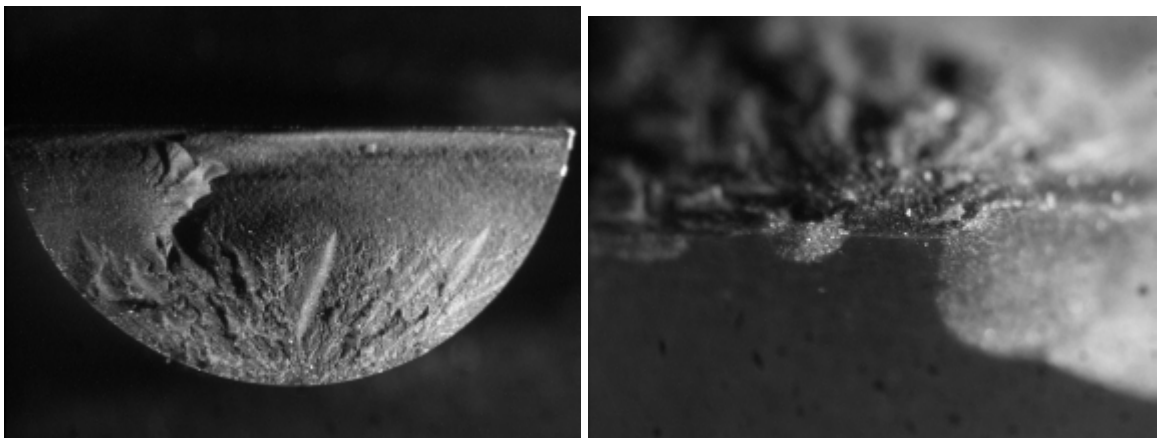


**Figure 7-17: Half RCF rod fine 06**

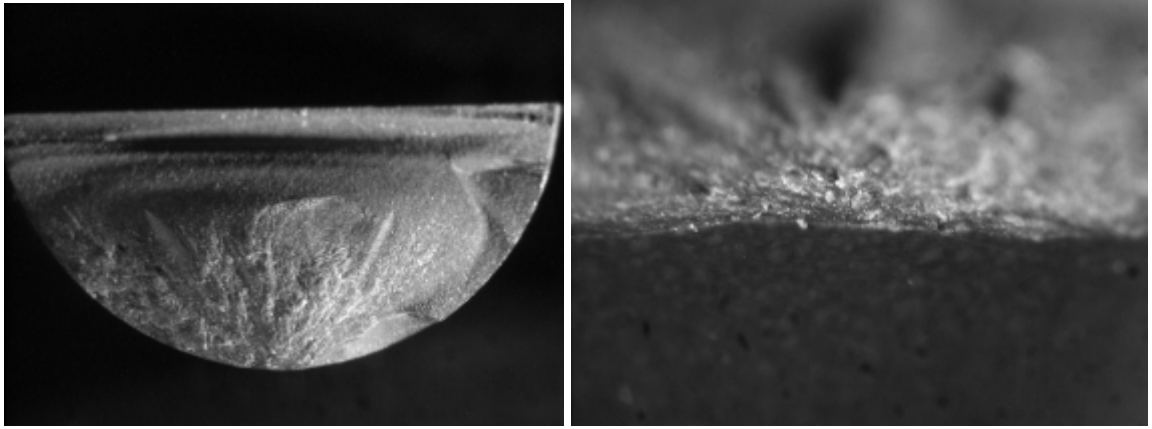


**Figure 7-18: Half RCF rod fine 07**

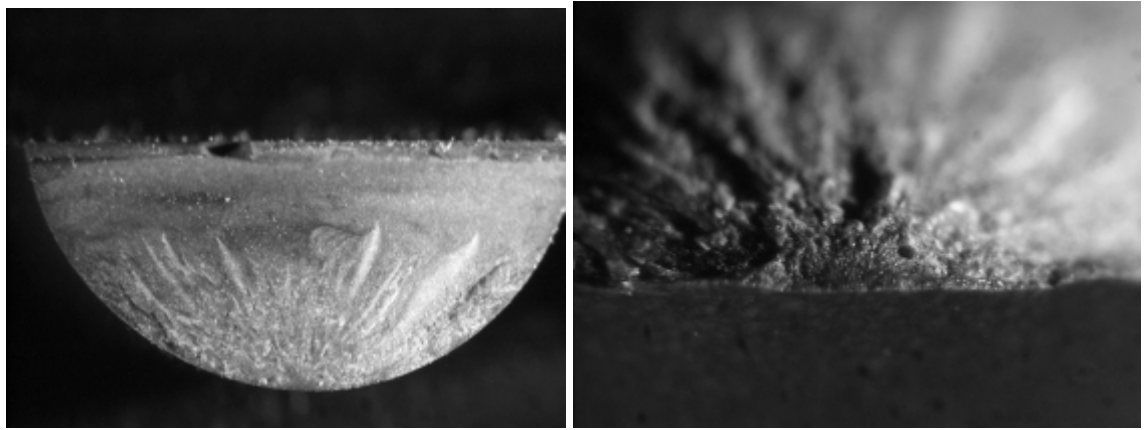


**Figure 7-19: Half RCF rod fine 08**

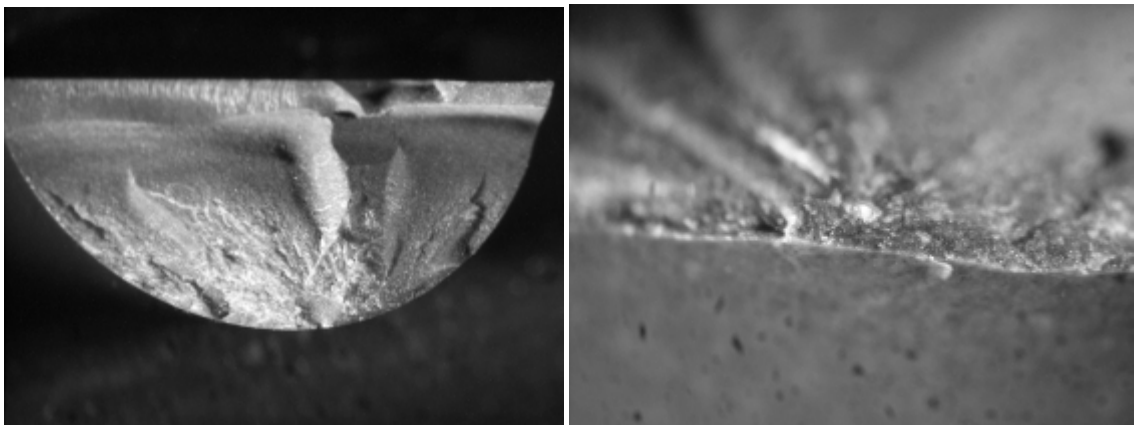


**Figure 7-20: Half RCF rod RCF-conventional 01**

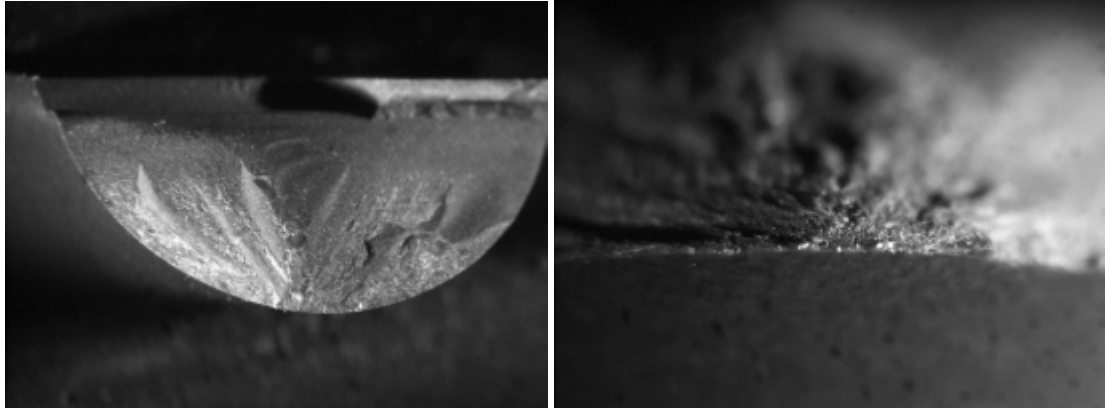


**Figure 7-21: Half RCF rod RCF-conventional 02**



**Figure 7-22: Half RCF rod RCF-conventional 03**

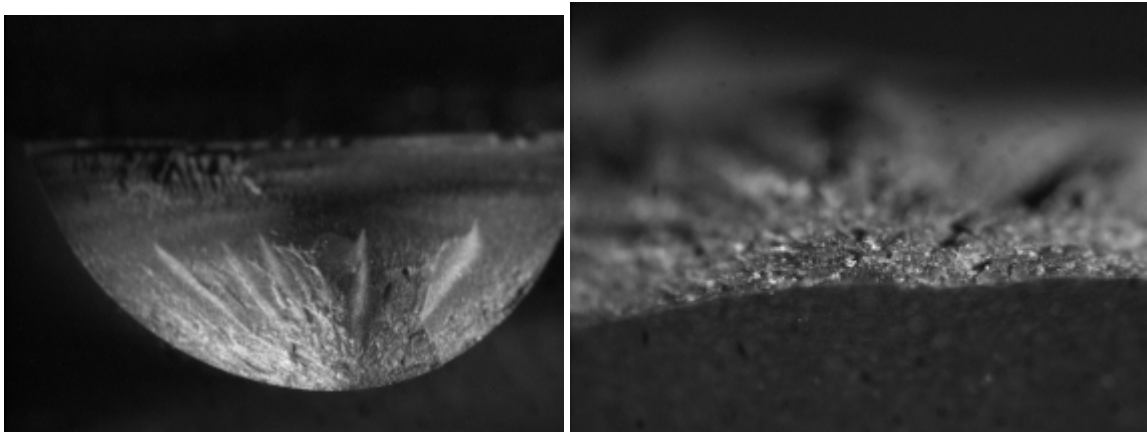


**Figure 7-23: Half RCF rod RCF-conventional 04**

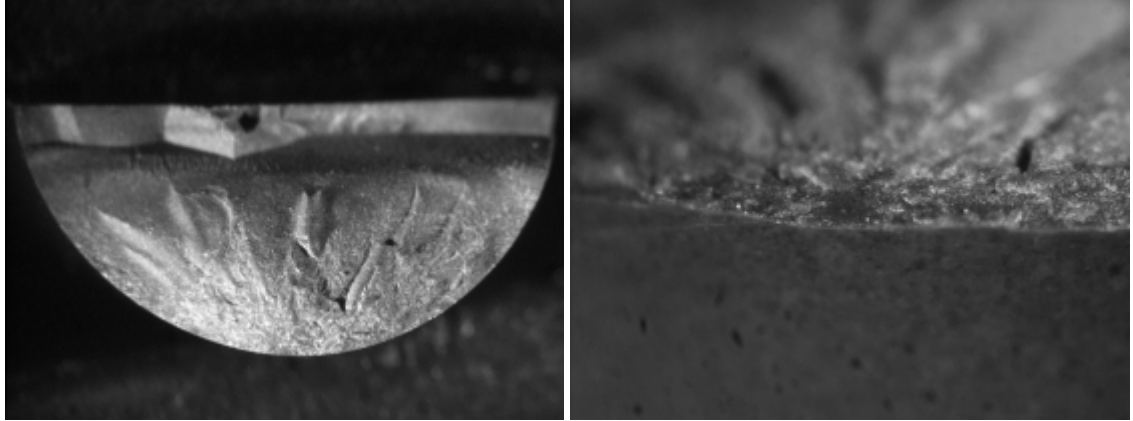


**Figure 7-24: Half RCF rod RCF-conventional 05**

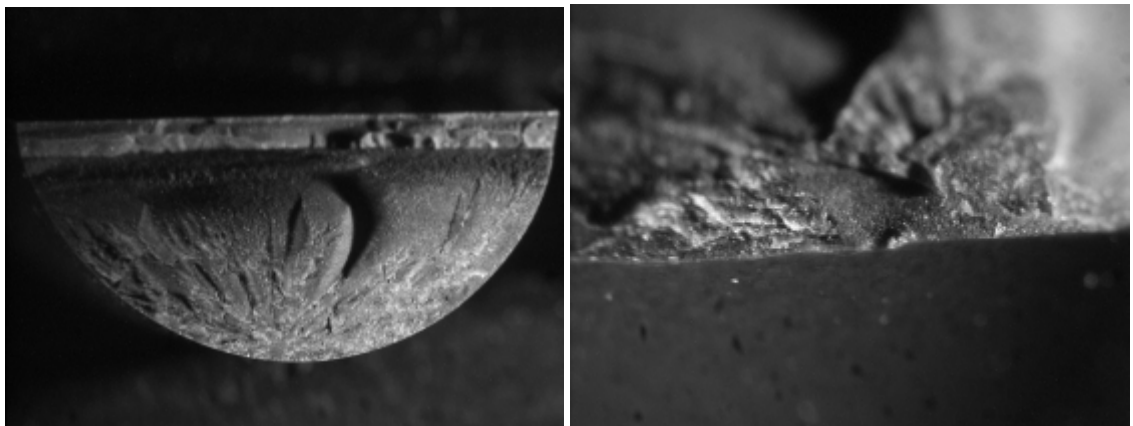


**Figure 7-25: Half RCF rod RCF-conventional 06**

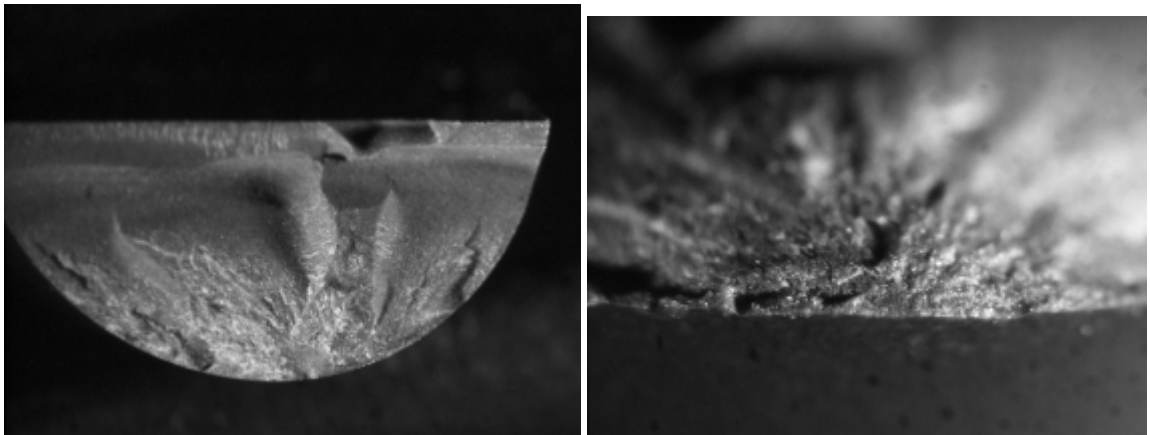


**Figure 7-26: Half RCF rod RCF-conventional 07**

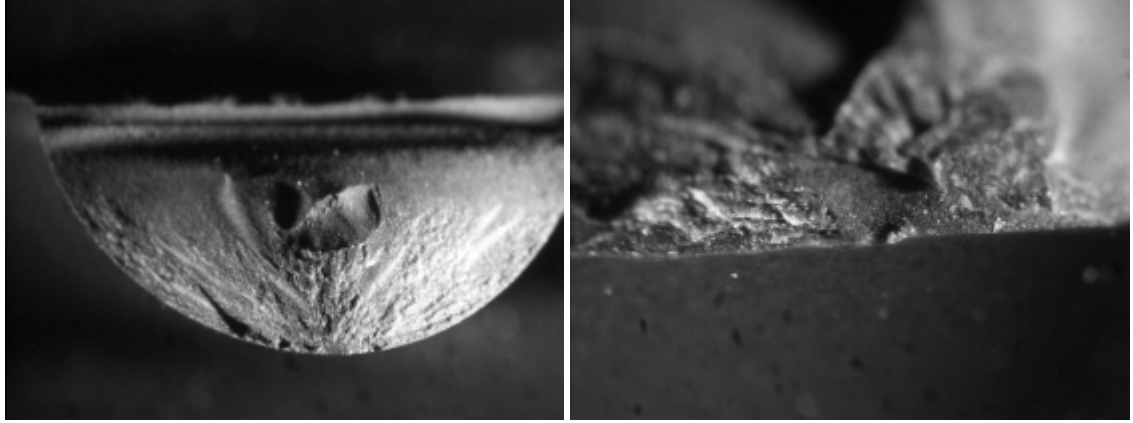


**Figure 7-27: Half RCF rod RCF-conventional 08**

### 7.3 C-Sphere SEM Fractography

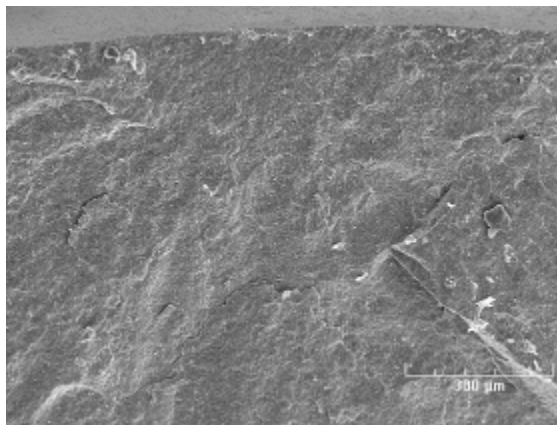
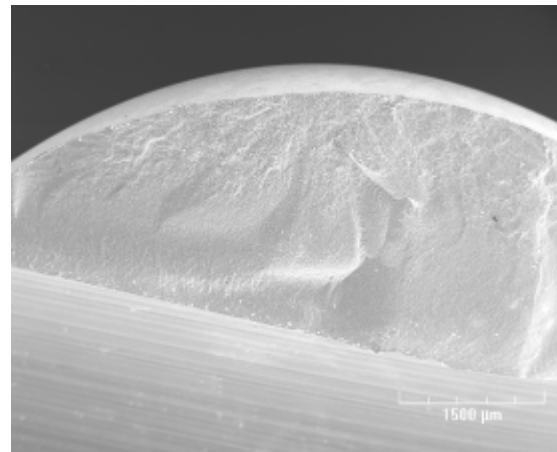
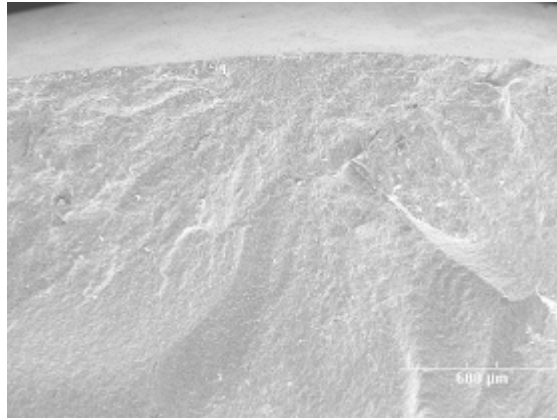


**Figure 7-28: C-Sphere SRBSN coarse 06**

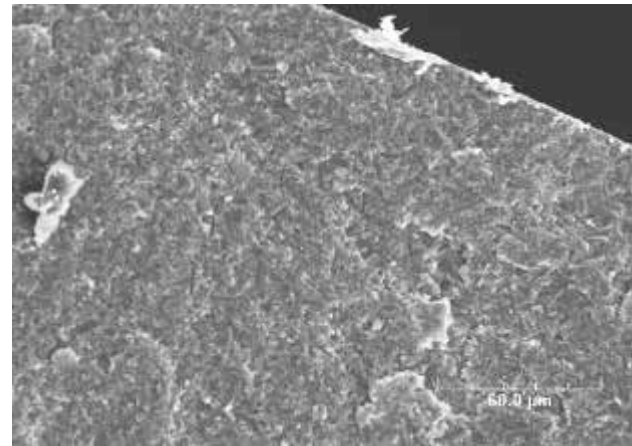
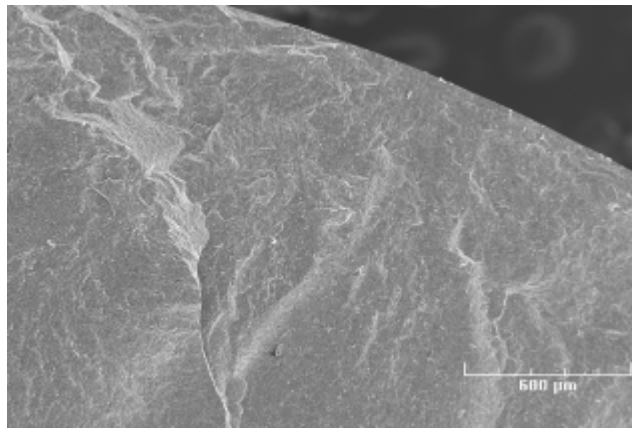
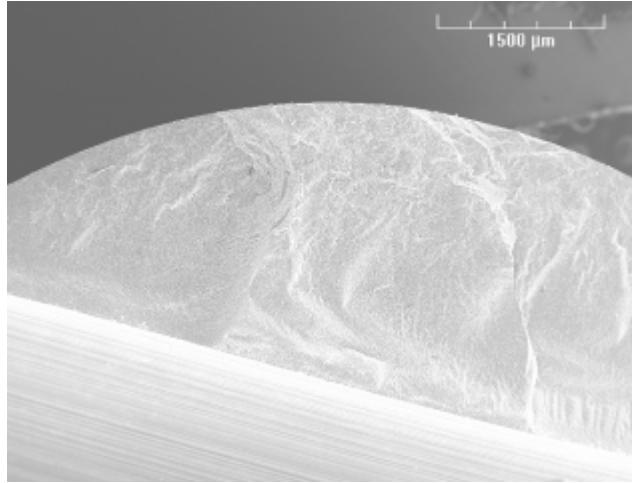


**Figure 7-29: C-Sphere SRBSN coarse 07**

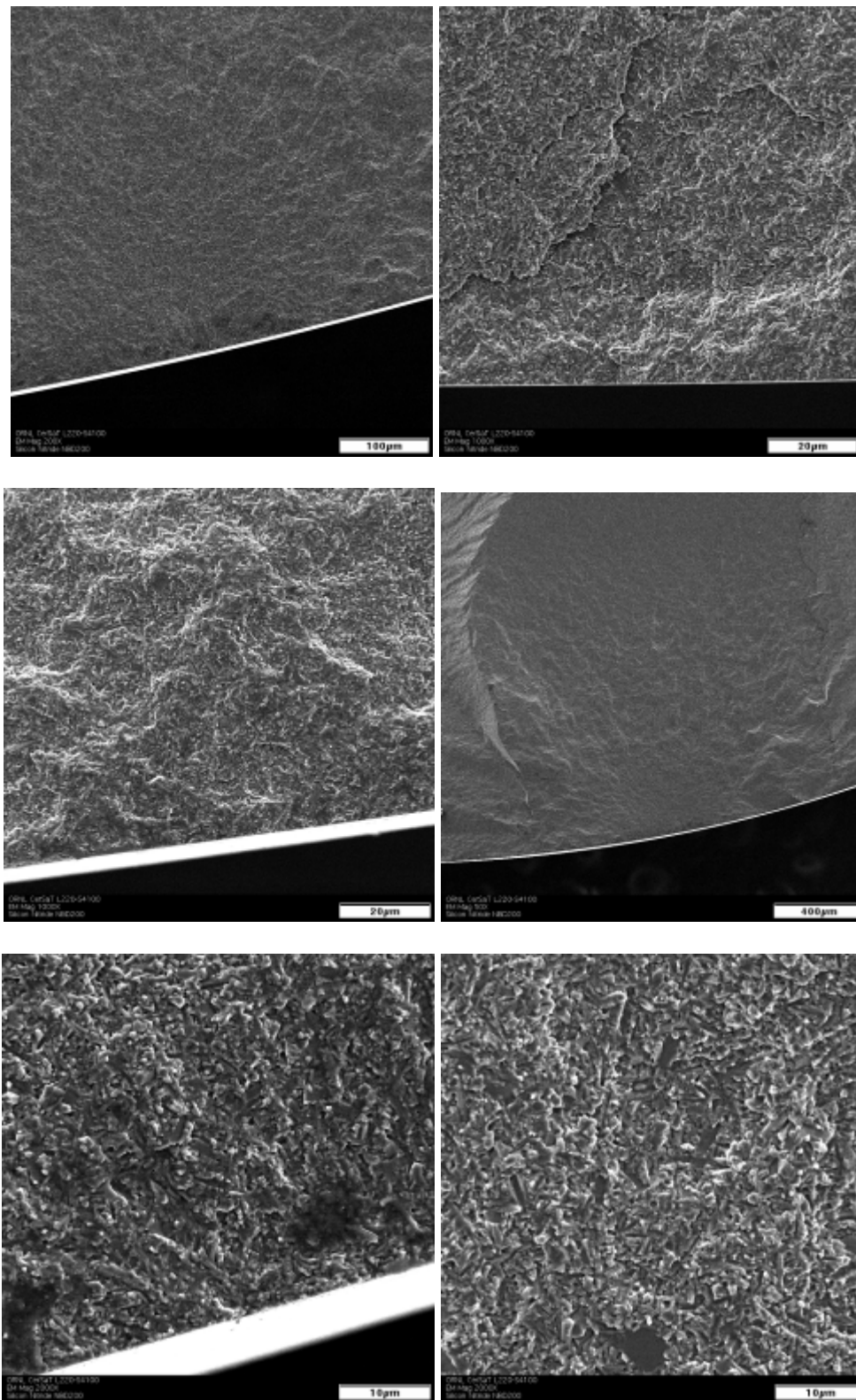


Figure 7-30: HIPed NBD200 specimen 07

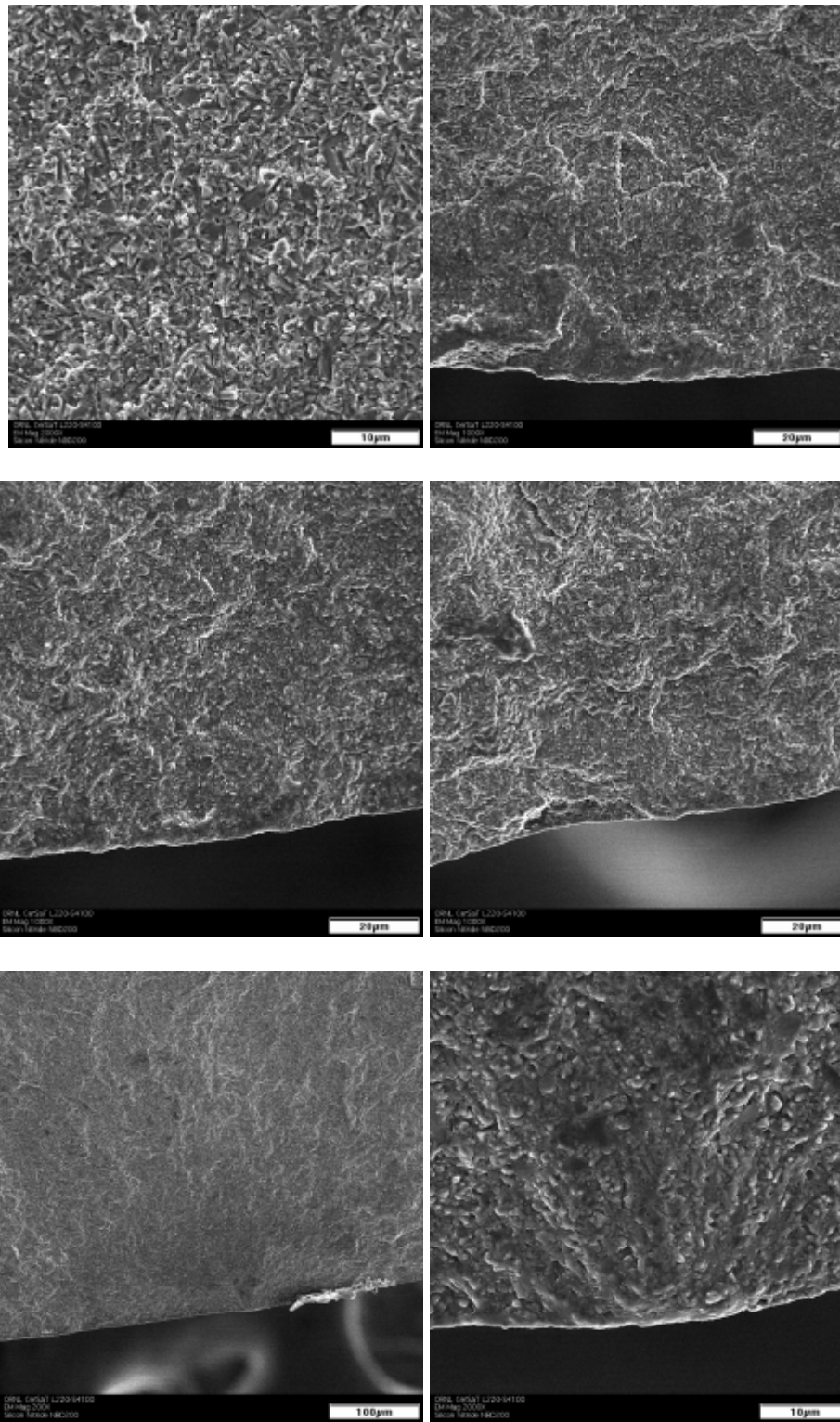


Figure 7-31: Figure 7-32: HIPed NBD200 specimen 05

## 7.4 Modified Four-Ball Machine – Hertzian Stress

Table 7.1 shows the relationship between four ball machine loading and the contact stress for a typical Silicon Nitride and steel ball contact.

Plint Machine Load (KN)	Contact Load (N)	Max. Compressive Stress (GPa)	Radius of contact circle (m)	Max. shear stress (Gpa)	Max. tensile stress (Gpa)
0.195873022	80	3.041370168	0.000112068	0.942824752	0.466343426
0.391746043	160	3.831886296	0.000141197	1.187884752	0.587555899
0.587619065	240	4.386414819	0.00016163	1.359788594	0.672583606
0.783492086	320	4.827874205	0.000177897	1.496641004	0.740274045
0.979365108	400	5.200669833	0.000191633	1.612207648	0.797436041
1.17523813	480	5.526536364	0.000203641	1.713226273	0.847402242
1.224206385	500	5.60225175	0.000206431	1.736698042	0.859011935
1.371111151	560	5.817931834	0.000214378	1.803558868	0.892082881
1.566984173	640	6.082740337	0.000224136	1.885649504	0.932686852
1.762857195	720	6.326304887	0.000233111	1.961154515	0.970033416
1.958730216	800	6.552433396	0.000241443	2.031254353	1.004706454
2.154603238	880	6.763946703	0.000249237	2.096823478	1.037138494
2.350476259	960	6.962999497	0.000256571	2.158529844	1.067659923
2.546349281	1040	7.151279175	0.000263509	2.216896544	1.096529474
2.742222303	1120	7.330134784	0.000270099	2.272341783	1.123954
2.938095324	1200	7.500663832	0.000276383	2.325205788	1.150101788
3.133968346	1280	7.663772592	0.000282393	2.375769503	1.175111797
3.329841368	1360	7.820219125	0.000288158	2.424267929	1.199100266
3.525714389	1440	7.970644696	0.000293701	2.470899856	1.22216552
3.721587411	1520	8.115597172	0.000299042	2.515835123	1.244391566
3.917460432	1600	8.255548764	0.000304199	2.559220117	1.26585081
4.113333454	1680	8.390909687	0.000309187	2.601182003	1.286606152

**Table 7-1: Relationship between machine loading and contact stress on four-ball machine**

## 7.5 Ball-on-Rod Tester Configuration

The ball-on-rod tester consists of a rotating cylindrical test specimen alternately stressed by rolling contact fatigue with three radially loaded balls. The balls are radially loaded against the test specimen by two tapered bearing cups which are thrust-loaded by three compressing springs. Figure 7-33 shows a breaking down of the load assembly.

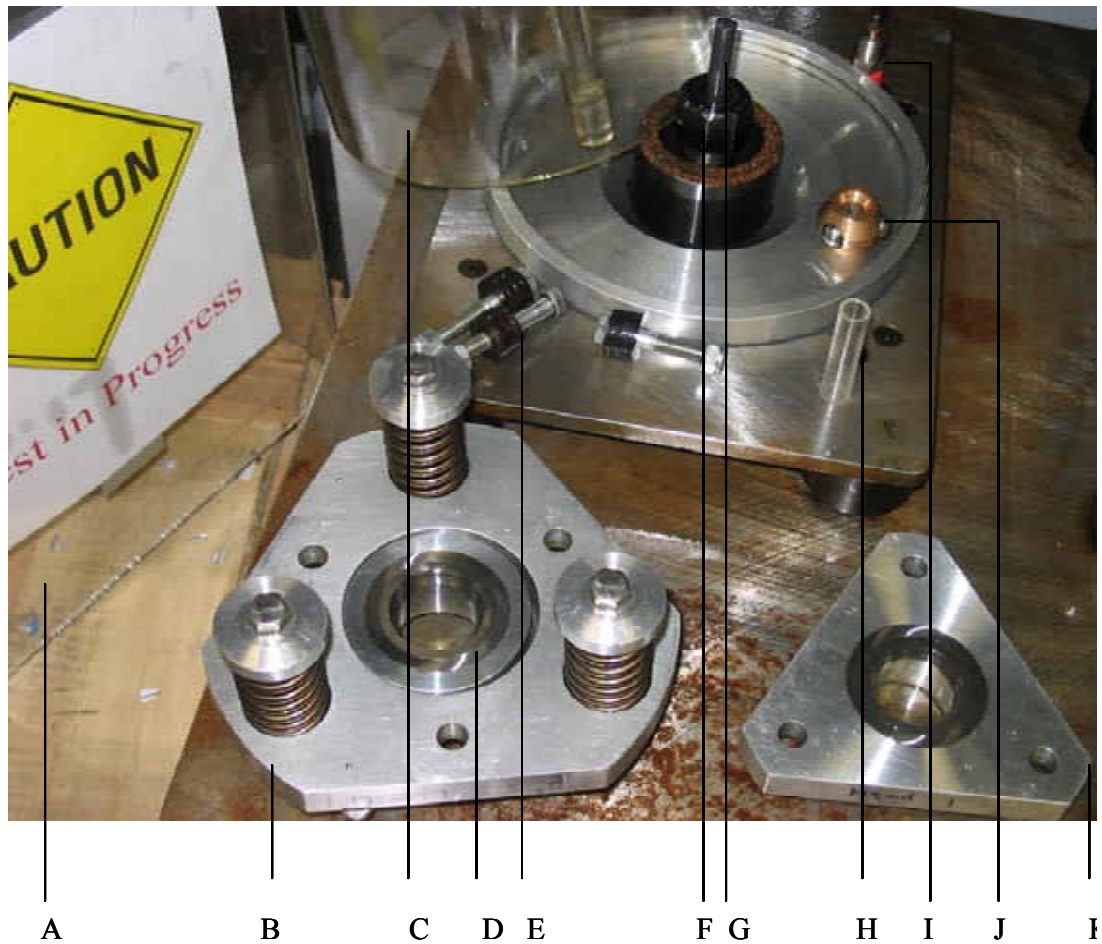


**Figure 7-33: A. plastic guard; B. middle plate, lower plate and spring assembly; C. small plastic guard; D. bearing cups; E. bolts and nuts assembly; F. nut; G. testing specimen; H. plastic guide; I. pick-up accelerator; J. copper container and steel balls; K. upper plate with bearing cup**

There are two steps to calibrate the tester. The first step is to measure the gap, and the second is to apply a known force to the lower cup. For step one, first install 3 balls, a retainer and a 0.3750 inch diameter bar in the head, which is shown in Figure 7-34, then

bolt the head firmly together ( the amount of spring pressure is not important at this point).



**Figure 7-34: Ball on rod tester test head**

The gap between the middle and lower aluminium plates needs to be accurately measured, as shown in Figure 7-35. Then calculate the average of the three gaps. The average is the one to use for calibration of the spring load.

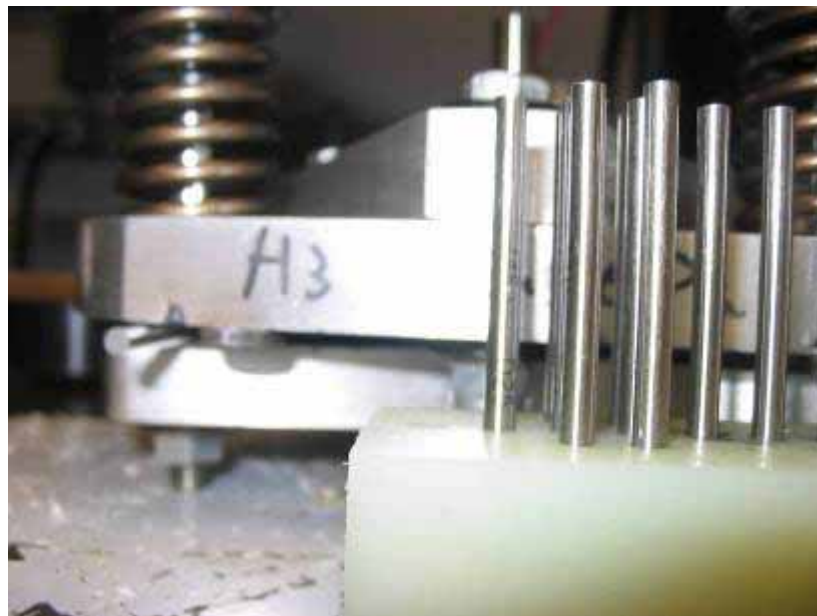


**Figure 7-35: Calibration: measurement of the gap between middle plate and lower plate.**

In step two, match the bolt holes on the middle plate with the posts on the bench. Place the calibration rod on top of the middle plate, and align the centre of the middle plate and the calibration rod, as shown in Figure 7-36.



**Figure 7-36: Calibration: apply a known load to the spring.**

Load the assembly until the gap between middle plate and lower plate is identical with the one measured in step one. Tighten or loosen the spring to get a load corresponding to the Hertzian pressure associated with the test. Make sure the gaps in three different directions are the same. Unload the assembly to complete the calibration.

## 7.6 Ball on Rod – Contact Analysis

The configuration of the ball-on-rod tester is to a 3/8” Silicon Nitride rod in contact with three AISI 52100 steel balls, which is shown in Figure 7-37. The rod is driven by a motor which rotates at 3600 rpm fixed speed.

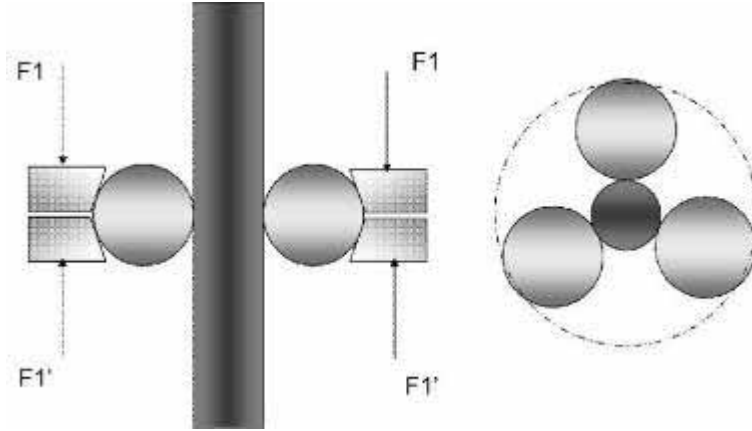


**Figure 7-37: Contact geometry of ball-on-rod tester**

The angle of  $\alpha$  and  $\alpha'$  can be read across the ball-on-rod tribotester manual where  $\alpha = \alpha' = 25.083$  degrees. Given  $F_1 = F_1'$ , so  $F_2 = 2F_1 / \tan \alpha = 4.27F_1$ . The ball on rod contact is an elliptical contact area ( $a, b, a < b$ ), and the effective modulus and equivalent relative curvature can be deduced using the equation below where  $R'$ ,  $R''$  are the principal relative radii of curvature in x and y direction.

$$E^* \text{ - Effective Modulus: } 1/E^* = (1 - \nu_1^2)/E_1 + (1 - \nu_2^2)/E_2 \quad (\text{Eq. 7-1})$$

$$R_e \text{ - Equivalent Relative Curvature: } R_e = (R'R'')^{1/2} \quad (\text{Eq. 7-2})$$

$$\text{Relative Curvature } (R'/R''): b/a = (R'/R'')^{1/2} \quad (\text{Eq. 7-3})$$

$$\text{Maximum Hertzian Pressure: } p_0 = \frac{3P}{2\pi ab} = \left( \frac{6PE^{*2}}{\pi^3 R_e^2} \right)^{1/3} \{F_1(e)\}^{-2} \quad (\text{Eq. 7-4})$$

$$\text{Compression: } \delta = \left( \frac{9P^2}{16E^{*2} R_e} \right)^{1/3} F_2(e) \quad (\text{Eq. 7-5})$$

$$\text{Equivalent Contact Radius: } c = (ab)^{1/2} = \left( \frac{3PR_e}{4E^*} \right)^{1/3} F_1(e) \quad (\text{Eq. 7-6})$$

Correction Factors  $F_1(e)$ ,  $\{F_1(e)\}^{-2}$ ,  $F_2(e)$  are shown in Figure 7-38.

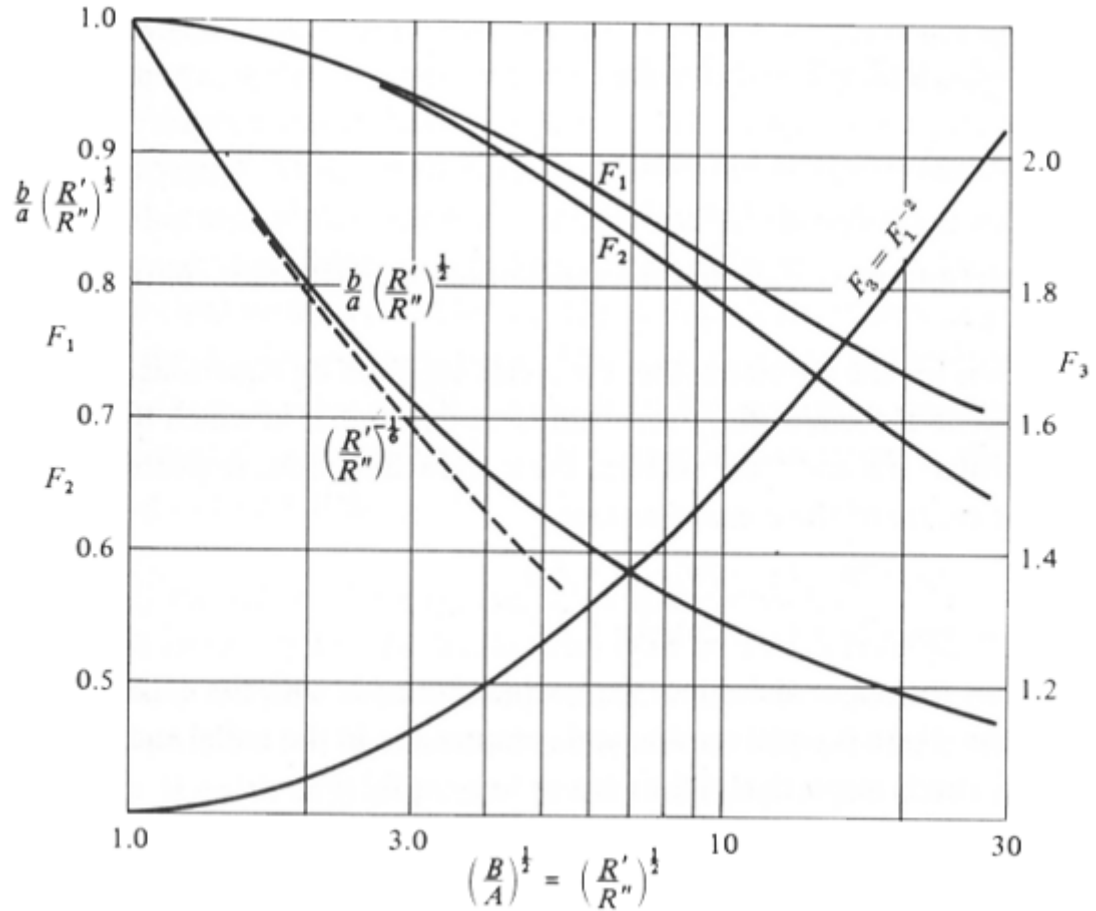


Figure 7-38: Correction factors plotted against  $(R'/R'')^{1/2}$  (Johnson 1987)

In the case of ball-on-rod contact of Silicon Nitride rod(A) and steel ball (B), where

$R_{AX} = 9999$  mm (Radius of body A in the crown direction)

$R_{BX} = 0.635$  mm (Radius of body B in the crown direction)

$R_{AY} = 0.47625$  mm (Radius of body A in the rolling direction)

$R_{BY} = 0.635$  mm (Radius of body B in the rolling direction)

$R' = R_{AX} * R_{BX} / (R_{AX} + R_{BX}) = 6.35$  mm

$R'' = R_{AY} * R_{BY} / (R_{AY} + R_{BY}) = 2.72$  mm

$R'/R'' = 2.333$

$(R'/R'')^{1/2} = 1.528$

$R_e = (R'R'')^{1/2} = 4.16 = 4.16 * 10^{-3}$  m

$F_1(e) = F_2(e) = 0.98, F_1(e)^{-2} = 1.04$

$E^* = 134.14$  GPa ( $E_A = 320$  GPa,  $E_B = 200$  GPa,  $\nu_A = 0.28, \nu_B = 0.29$ )

$$P_0 = 3P/2\pi ab = (6PE^{*2}/\pi^3 R_e^2)^{1/3} \{F_1(e)\}^{-2} \quad (\text{Eq. 7-7})$$

For 5.6 GPa Maximum Contact Stress, the corresponding contact load is,

$$P = \frac{\left(\frac{P_0}{\{F_1(e)\}^{-2}}\right)^3 \times \pi^3 R_e^2}{6E^{*2}} = \frac{\left(\frac{5.6 \times 10^9}{1.04}\right)^3 \times \pi^3 \times (4.16 \times 10^{-3})^2}{6 \times (134.14 \times 10^9)^2} = 775.94(N) \quad (\text{Eq. 7-8})$$

$$c = (ab)^{1/2} = \left(\frac{3PR_e}{4E^*}\right)^{1/3} F_1(e) = \left(\frac{3 \times 775.94 \times 4.16 \times 10^{-3}}{4 \times 134.14 \times 10^9}\right)^{1/3} \times 0.98 = 2.57 \times 10^{-4} (m) \quad (\text{Eq. 7-9})$$

$b/a = (R'/R'')^{1/2} = 1.528$ ,  $a = 0.2079$  mm,  $b = 0.3177$  mm, width of contact path = 0.62.

Table 7.2 shows the relationship between the ball-on-rod machine spring loading and contact stress for a typical Silicon Nitride rod and steel ball contact.

Radial Load (N)	Load Single Spring (N)	Calibration load (N)	Contact Stress (GPa)
0.00	0.00	0.00	0.0000
1.45	0.34	1.02	0.6895
11.60	2.71	8.14	1.3790
12.97	3.04	9.11	1.4312
38.91	9.11	27.32	2.0642
39.15	9.16	27.49	2.0684
62.17	14.55	43.65	2.4132
90.79	21.25	63.75	2.7379
92.80	21.72	65.16	2.7579
132.13	30.92	92.77	3.1026
181.25	42.42	127.26	3.4474
181.59	42.50	127.50	3.4495
241.25	56.46	169.38	3.7921
311.30	72.86	218.57	4.1284
313.21	73.30	219.91	4.1369
398.21	93.20	279.59	4.4816
445.95	104.37	313.11	4.6540
492.88	115.35	346.06	4.8118
497.36	116.40	349.20	4.8263
611.73	143.17	429.51	5.1711
739.33	173.03	519.09	5.5081
742.42	173.75	521.26	5.5158
890.50	208.41	625.23	5.8605
1,057.07	247.40	742.19	6.2053
1,243.22	290.96	872.88	6.5500
1,450.03	339.36	1018.09	6.8948

**Table 7-2: Relationship between spring loading and contact stress on ball-on-rod machine**

## 7.7 Absolute Viscosity

The absolute viscosity of three lubricants used in the lubricant study can be derived by calculating the constants  $S_0$  and  $G_0$  in the equation. For lubricant one, at 40 degrees,

$$\eta_1 = \eta_{k1} * \rho_1 = 53.8 \text{ cSt}/10^6 * 847 = 4.6 * 10^{-2} \text{ N}\cdot\text{s}/\text{m}^2 = 46 \text{ cP} \quad (\text{Eq. 7-10})$$

and at 100 degree,

$$\eta_1 = \eta_{k1} * \rho_1 = 8.98 \text{ cSt}/10^6 * 847 = 7.6 * 10^{-3} \text{ N}\cdot\text{s}/\text{m}^2 = 7.6 \text{ cP} \quad (\text{Eq. 7-11})$$

$$\log(\log 46 + 1.200) = -S_0 \log\left(1 + \frac{40}{135}\right) + \log G_0 \quad (\text{Eq. 7-12})$$

$$\log(\log 7.6 + 1.200) = -S_0 \log\left(1 + \frac{100}{135}\right) + \log G_0 \quad (\text{Eq. 7-13})$$

$$S_0 = 1.08, G_0 = 3.79$$

$$\eta = 10^{\left(1 + \frac{t_m}{135}\right)^{-1.08} \times 3.79} \times 0.063 \quad (\text{Eq. 7-14})$$

Similarly for lubricant two, at 40 degree,

$$\eta_2 = \eta_{k2} * \rho_2 = 64 \text{ cSt}/10^6 * 837 = 0.0536 \text{ N}\cdot\text{s}/\text{m}^2 = 53.6 \text{ cP} \quad (\text{Eq. 7-15})$$

and at 100 degree,

$$\eta_2 = \eta_{k2} * \rho_2 = 11.8 \text{ cSt}/10^6 * 837 = 0.0099 \text{ N}\cdot\text{s}/\text{m}^2 = 9.9 \text{ cP} \quad (\text{Eq. 7-16})$$

$$\log(\log 53.6 + 1.200) = -S_0 \log\left(1 + \frac{40}{135}\right) + \log G_0 \quad (\text{Eq. 7-17})$$

$$\log(\log 9.9 + 1.200) = -S_0 \log\left(1 + \frac{100}{135}\right) + \log G_0 \quad (\text{Eq. 7-18})$$

$$S_0 = 0.978, G_0 = 3.775$$

$$\eta = 10^{\left(1 + \frac{t_m}{135}\right)^{-0.978} \times 3.775} \times 0.063 \quad (\text{Eq. 7-19})$$

For lubricant three, at 40 degrees

$$\eta_3 = \eta_{k3} * \rho_3 = 79 \text{ cSt}/10^6 * 867 = 0.0685 \text{ N}\cdot\text{s}/\text{m}^2 = 68.5 \text{ cP} \quad (\text{Eq. 7-20})$$

and at 100 degrees,

$$\eta_3 = \eta_{k3} * \rho_3 = 12.3 \text{ cSt}/10^6 * 867 = 0.0107 \text{ N}\cdot\text{s}/\text{m}^2 = 10.7 \text{ cP} \quad (\text{Eq. 7-21})$$

$$\log(\log 79 + 1.200) = -S_0 \log\left(1 + \frac{40}{135}\right) + \log G_0 \quad (\text{Eq. 7-22})$$

$$\log(\log 10.7 + 1.200) = -S_0 \log\left(1 + \frac{100}{135}\right) + \log G_0 \quad (\text{Eq. 7-23})$$

$$S_0 = 1.116, G_0 = 4.138$$

$$\eta = 10^{\left(1 + \frac{t_m}{135}\right)^{-1.116} \times 4.138} \times 0.063 \quad (\text{Eq. 7-24})$$

## REFERENCES

- Abe, T., S. Niizeki, et al. (1988). "Rolling Contact Fatigue Life of Si<sub>3</sub>N<sub>4</sub> Ceramics Ball and Analysis of Flaking Origin." Proceedings JAST Tribology Conference, Okayama: 53-56.
- Ahmed, R. and M. Hadfield (1996). "Rolling contact fatigue behaviour of thermally sprayed rolling elements." Surface & Coatings Technology **82**(1-2): 176-186.
- Akazawa, M. (1986). "Wear Properties of Silicon Nitride in Rolling Contact." Wear **110**: 285-293.
- Akazawa, M. and K. Kato (1988). "Wear properties of silicon nitride in rolling-sliding contact." Wear **124**: 123-132.
- Akazawa, M., K. Kato, et al. (1989). "Wear properties of silicon nitride in rolling contact." Wear **110**: 285-293.
- Allen, D. L. (1994). "Effect of Composition and Physical-Properties of Silicon- Nitride on Rolling Wear and Fatigue Performance." Tribology Transactions **37**(2): 410-414.
- Asada, S., K. Hashimoto, et al. (1992). Rolling-Contact Fatigue of Engineering Ceramics. Sintering 91. Zurich, TRANS TECH PUBLICATIONS LTD. **25**: 627-634.
- Barwell, F. T. and D. Scott (1956). "Effect of lubriant on pitting failure of ball bearings." Engineering(July 6): 9-12.
- Baumgartner, H. R., Ed. (1974). Evaluation of roller bearings containing hot-presses silicon nitride rolling elements. Ceramics for high performance application. Chestnut Hill, MA, Brook Hill Publishing.
- Bhandhubanyong, P. and T. Akhadejdamrong (1997). "Forming of silicon nitride by the HIP process." Journal Of Materials Processing Technology **63**(1-3): 277-280.
- Bocanegra-Bernal, M. H. (2004). "Hot Isostatic Pressing (HIP) technology and its applications to metals and ceramics." Journal Of Materials Science **39**(21): 6399-6420.
- Braza, J. F., H. S. Cheng, et al. (1989). "Mechanical Failure Mechanisms in Ceramic Sliding and Rolling Contacts." Tribology Transactions **32**(1): 1-8.

- Burrier, H. I. (1996). "Optimizing the structure and properties of silicon nitride for rolling contact bearing performance." Tribology Transactions **39**(2): 276-285.
- C1323 (2001). "Standard Testing Method for Ultimate Strength of Advanced Ceramics with Diametrically Compressed C-Ring Specimens at Ambient Temperature." Annual Book of ASTM Standards **15.01**: 1-6.
- Chao, L. Y., R. Lakshminarayanan, et al. (1998). "Transient wear of silicon nitride in lubricated rolling contact." Wear **223**(1-2): 58-65.
- Chao, L. Y., R. Lakshminarayanan, et al. (1995). "Rolling-Contact Fatigue and Wear of Cvd-Sic with Residual Surface Compression." Journal of the American Ceramic Society **78**(9): 2307-2313.
- Chao, L. Y. and D. K. Shetty (1995). "Development of Silicon Nitride for Rolling Contact Bearing Applications: A Review." Journal of Materials Education **17**: 245-303.
- Cowley, P. E. and J. W. Lueck (1979). Investigation of the use of silicon nitride in aircraft engine bearings., Final report to Naval Air Systems Command, Contract N00019-76-C-0251.
- Fujiwara, T., T. Yoshioka, et al. (1989). "Study on load rating property of silicon nitride for rolling bearing material." Journal of JSLE International Edition: 81-86.
- Glover, D. (1982). A Ball-Rod Rolling Contact Fatigue Tester. ASTM STP 771. Philadelphia, PA, ASTM.
- Guo, G. F., J. B. Li, et al. (2007). "Direct measurement of residual stresses and their effects on the microstructure and mechanical properties of heat-treated Si<sub>3</sub>N<sub>4</sub> ceramics II: With CeO<sub>2</sub> as a single additive." Acta Materialia **55**(9): 3245-3251.
- Hadfield, M. (1993). Rolling contact fatigue of ceramics. London, Brunel University.
- Hadfield, M. (1998). "Failure of silicon nitride rolling elements with ring crack defects." Ceramics International **24**(5): 379-386.
- Hadfield, M. and T. A. Stolarski (1995). "Observations of Delamination Fatigue on Pre-cracked Ceramic Elements in Rolling-Contact." Ceramics International **21**(2): 125-130.

- Hadfield, M., T. A. Stolarski, et al. (1993). "Failure Modes of Ceramics in Rolling-Contact." Proceedings of the Royal Society of London Series a- Mathematical Physical and Engineering Sciences **443**(1919): 607-621.
- Hadfield, M., T. A. Stolarski, et al. (1993). "Failure Modes of Ceramic Elements with Ring-Crack Defects." Tribology International **26**(3): 157-164.
- Hadfield, M. and S. Tobe (1998). "Residual stress measurements of hot isostatically pressed silicon nitride rolling elements." Ceramics International **24**(5): 387-392.
- Hadfield, M., S. Tobe, et al. (1994). "Subsurface Crack Investigation on Delaminated Ceramic Elements." Tribology International **27**(5): 359-367.
- Hsieh, C. P. and B. T. Khuriyakub (1992). "Surface Defect Inspection of Spherical Objects by the Resonant Sphere Technique." Applied Physics Letters **60**(15): 1815-1817.
- Hsieh, C. P. and B. Y. Khuriyakub (1993). "One-Point Contact Measurement of Spherical Resonances." Applied Physics Letters **62**(24): 3091-3093.
- Jahanmir, S. (1993). Effect of Grinding on Strength and Surface Integrity of Silicon Nitride. Machining of Advanced Materials, Gaithersburg, Maryland.
- Johnson, K. L. (1987). Contact mechanics. Cambridge, Cambridge University Press.
- Jones, W. R. (1975). "Pressure Viscosity Measurements for Several Lubricants to  $5.5 \times 10^8$  Pa and 149 degree celcius." ASLE Transactions **18**(4): 249-262.
- Kang, J. and M. Hadfield (1999). A study on the lapping of ceramic balls. Surface Treatment Iv - Computer Methods and Experimental Measurements. Southampton, WIT PRESS. **3**: 389-399.
- Kang, J. and M. Hadfield (2001). "A novel eccentric lapping machine for finishing advanced ceramic balls." Proceedings of the Institution of Mechanical Engineers Part B- Journal of Engineering Manufacture **215**(6): 781-795.
- Kang, J. and M. Hadfield (2001). "Parameter optimization by Taguchi methods for finishing advanced ceramic balls using a novel eccentric lapping machine." Proceedings of the Institution of Mechanical Engineers, Part B: Journal of Engineering Manufacture **215**(1): 69-78.

- Kang, J. and M. Hadfield (2002). "The influences of natural surface defects on rolling contact fatigue failure modes of HIPed Si<sub>3</sub>N<sub>4</sub>." Industrial Ceramics **22**(3): 185-192.
- Kang, J., M. Hadfield, et al. (2000). The consequences of aggressive lapping processes on the surface integrity of HIPed silicon nitride bearing balls. 1st International Conference on Tribology in Environmental Design 2000 - the Characteristics of Interacting Surfaces - a Key Factor in Sustainable and Economic Products. Bury St Edmunds, PROFESSIONAL ENGINEERING PUBLISHING LTD: 227-234.
- Kang, J., M. Hadfield, et al. (2002). "Residual stress field of HIPed silicon nitride rolling elements." Ceramics International **28**(6): 645-650.
- Karaszewski, W. (2008). "The influence of oil additives on spread cracks in silicon nitride." Tribology International **41**(9-10): 889-895.
- Katz, R. N. (1985). "Ceramics for High Performance Rolling Element Bearings: A Review and Assessment." International Journal of High Technology Ceramics **1**: 69-79.
- Kelina, I. Y., Tkacheva, II, et al. (2005). "Tribological properties and testing of bearings fabricated from hot-pressed silicon nitride-based ceramics." Refractories And Industrial Ceramics **46**(1): 15-20.
- Khan, Z. A., M. Hadfield, et al. (2005). "Ceramic rolling elements with ring crack defects - A residual stress approach." Materials Science And Engineering A-Structural Materials Properties Microstructure And Processing **404**(1-2): 221-226.
- Khan, Z. A., M. Hadfield, et al. (2006). "Residual stress variations during rolling contact fatigue of refrigerant lubricated silicon nitride bearing elements." Ceramics International **32**(7): 751-754.
- Kida, K., K. Kitamura, et al. (2005). "Static and fatigue strengths of pre-cracked silicon nitride balls under pressure load." International Journal Of Fatigue **27**(2): 165-175.
- Kikuchi, K., T. Yoshioka, et al. (1984). "Rolling contact fatigue life of ceramics for rolling element bearing materials." J. JSLE Int. Ed.: 137-142.
- Komanduri, R., Z. B. Hou, et al. (1999). "A "gentle" method for finishing Si<sub>3</sub>N<sub>4</sub> balls for hybrid bearing applications." Tribology Letters **7**(1): 39-49.

- Krivoshein, G. S. (1960). "On evaluating the effect of lubricants on the fatigue pitting of steel." Industr. Lub. **26**: 405-407.
- Lakshminarayanan, R., L. Y. Chao, et al. (1997). "Wear of steel in rolling contact with silicon nitride." Wear **210**(1-2): 278-286.
- Lee, J. S., J. H. Mun, et al. (2003). "Effect of beta-Si<sub>3</sub>N<sub>4</sub> seed particles on the property of sintered reaction-bonded silicon nitride." Ceramics International **29**(8): 897-905.
- Lee, J. S., J. H. Mun, et al. (2004). "Effect of raw-Si particle size on the properties of sintered reaction-bonded silicon nitride." Ceramics International **30**(6): 965-976.
- Levesque, G. and N. K. Arakere (2008). "An investigation of partial cone cracks in silicon nitride balls." International Journal Of Solids And Structures **45**(25-26): 6301-6315.
- Levesque, G. A. and N. K. Arakere "Critical Flaw Size in Silicon Nitride Ball Bearings." Tribology Transactions **53**(4): 511-519.
- Li, W. B., B. Q. Lei, et al. (1999). "Stresses developed in reaction-bonded ceramics." Journal Of The European Ceramic Society **19**(3): 277-283.
- Lu, B. H., J. L. Yuan, et al. (2002). Ultra-precision manufacturing of silicon nitride balls. Proceedings Of The Second International Symposium On Instrumentation Science And Technology, Vol 2. Harbin, Harbin Institute Technology Publishers: 182-187.
- Lueck, J. W. (1990). Rolling wear of silicon nitride bearing materials. Gas turbine and aero-engine congress and exposition, Brussels, Belgium.
- Muller, M., W. Bauer, et al. (2009). "Processing of micro-components made of sintered reaction-bonded silicon nitride (SRBSN). Part 1: Factors influencing the reaction-bonding process." Ceramics International **35**(7): 2577-2585.
- Muller, M., J. Rogner, et al. (2009). "Processing of micro-components made of sintered reaction-bonded silicon nitride (SRBSN). Part 2: Sintering behaviour and micro-mechanical properties." Ceramics International **36**(2): 707-717.
- Nishihara, Y. (1988). "Rolling Contact Fatigue Life of Si<sub>3</sub>N<sub>4</sub> Ceramics and Various Kinds of Factors Affecting Rolling Contact Fatigue Life of Ceramic Balls." NTN Technical Review **54**: 31-39.

- Otsuka, A., H. Sugawara, et al. (1994). "Mechanism of Rolling Fatigue and Mode II Fatigue Crack Growth - A Proposal on a Mode II Fatigue Crack Growth Test Method." J. Soc. Mat. Sci. Japan **43**: 55-56.
- Parker, R. and E. V. Zaretsky (1975). "Fatigue life of high-speed ball bearings with silicon nitride balls." Trans. of the ASME, J. of Lub. Tech.: 350-357.
- Quinn, G. D., L. K. Ives, et al. (2003). On the Fractographic Analysis of Machining Cracks in Ground Ceramics: A Case Study on Silicon Nitride, NIST.
- Ren, C. Z., T. Y. Wang, et al. (2002). "Experimental research on the residual stress in the surface of silicon nitride ceramic balls." Journal Of Materials Processing Technology **129**(1-3): 446-450.
- Riley, F. L. (2000). "Silicon nitride and related materials." Journal of the American Ceramic Society **83**(2): 245-265.
- Roosen, A. R. and W. C. Carter (1998). "Simulations of microstructural evolution: anisotropic growth and coarsening." Physica a-Statistical Mechanics and Its Applications **261**(1-2): 232-247.
- Scott, D. "Study of the effect of lubricant on pitting failure of balls."
- Terwilliger, G. F. (1974). "Properties of Sintered Silicon Nitride." Journal of American Ceramic Society **57**(1): 48-49.
- Terwilliger, G. F. and F. F. Lange (1975). "Pressureless Sintering of Silcion Nitride." Journal of Materials Science **10**: 1169-1174.
- Thoma, K., L. Rohr, et al. (2004). "Materials failure mechanisms of hybrid ball bearings with silicon nitride balls." Tribology International **37**(6): 463-471.
- Touret, R. and E. P. Wright, Eds. (1976). Rolling contact fatigue performance testing of lubricants: papers presented at the international symposium organized by the insitute of petroleum. London, Heydon.
- Trivedi, H. K., M. M. Massey, et al. (2001). "Next generation lubrication system for weapons." Tribology Letters **10**(4): 229-235.
- Trivedi, H. K. and C. S. Saba (2001). "Effect of temperature on tribological performance of a silicon nitride ball material with a linear perfluoropolyalkylether." Tribology Letters **10**(3): 171-177.

- Tuyen, D. V., Y. J. Park, et al. (2009). "Formation of rod-like Si<sub>3</sub>N<sub>4</sub> grains in porous SRBSN bodies using 6Y(2)O(3)-2MgO sintering additives." Ceramics International **35**(6): 2305-2310.
- Wang, L., R. W. Snidle, et al. (2000). "Rolling contact silicon nitride bearing technology: a review of recent research." Wear **246**(1-2): 159-173.
- Wang, Y. and M. Hadfield (1999). "Rolling contact fatigue failure modes of lubricated silicon nitride in relation to ring crack defects." Wear **229**: 1284-1292.
- Wang, Y. and M. Hadfield (1999). "Rolling contact fatigue failure modes of lubricated silicon nitride in relation to ring crack defects." Wear **229**(2): 1284-1292.
- Wang, Y. and M. Hadfield (2000). Boundary element analysis of surface ring crack in silicon nitride bearing elements. 1st International Conference on Tribology in Environmental Design 2000 - the Characteristics of Interacting Surfaces - a Key Factor in Sustainable and Economic Products. Bury St Edmunds, PROFESSIONAL ENGINEERING PUBLISHING LTD: 297-304.
- Wang, Y. and M. Hadfield (2000). "Influence of ring crack location on the rolling contact fatigue failure of lubricated silicon nitride: Experimental studies." Wear **243**(1): 157-166.
- Wang, Y. and M. Hadfield (2000). "Influence of ring crack location on the rolling contact fatigue failure of lubricated silicon nitride: Fracture mechanics analysis." Wear **243**(1): 167-174.
- Wang, Y. and M. Hadfield (2001). "Ring crack propagation in silicon nitride under rolling contact." Wear **250-251**(PART 1): 282-292.
- Wang, Y. and M. Hadfield (2002). "Rolling-Contact Fatigue of Ceramics." ASM Handbook **11**: 957-964.
- Wang, Y. and M. Hadfield (2002). "A study of line defect fatigue failure of ceramic rolling elements in rolling contact." Wear **253**(9-10): 975-985.
- Wang, Y. and M. Hadfield (2003). Life prediction for surface crack initiated contact fatigue of silicon nitride bearing balls. Tribological Research and Design for Engineering Systems. Amsterdam, ELSEVIER SCIENCE BV: 349-358.
- Wang, Y. and M. Hadfield (2003). "A mechanism for nucleating secondary fractures near a pre-existing flaw subjected to contact loading." Wear **254**(7-8): 597-605.

- Wereszczak, A. A., R. J. Caspe, et al. (2003). C-ring strength of advanced monolithic ceramics. 27th International Cocoa Beach Conference on Advanced Ceramics and Composites: B. **24**: 483-490.
- Xu, J., F. Luo, et al. (2008). "Effect of presintering on the dielectric and mechanical properties of porous reaction-bonded silicon nitride." Materials Science And Engineering A-Structural Materials Properties Microstructure And Processing **488**(1-2): 167-171.
- Yoshioka, T. and M. Takeda (1994). "Clarification of rolling contact fatigue initiation using acoustic emission technique." Lubrication Eng. **51**(41-44).
- Zhao, P., M. Hadfield, et al. (2003). Experimental investigation of lubricated surface ring crack fatigue in rolling contact. Tribology in Environmental Design 2003. Bury St Edmunds, PROFESSIONAL ENGINEERING PUBLISHING LTD: 301-310.
- Zhou, J. and G. Wu (2009). "Experimental study of cyclic rolling-contact fatigue of silicon nitride balls." Tribology Transactions **52**(5): 663.
- Zhou, J., G. Wu, et al. (2007). "Volume defect fatigue failure of ceramic balls under rolling condition." Chinese Journal of Mechanical Engineering (English Edition) **20**(2): 47.
- Zhou, J., G. Wu, et al. (2007). "Critical stress of silicon nitride ceramic balls under pure rolling condition." Jixie Qiangdu/Journal of Mechanical Strength **29**(4): 661.
- Zhou, J. L., G. Q. Wu, et al. (2009). "Tensile stress fatigue life model of silicon nitride ceramic balls." Tribology International **42**(11-12): 1838-1845.